

Fabrication, Analysis, Simulation, and Application of the Nanohole Array Sensor

by
Guang Yang

A Dissertation submitted to the Materials Science & Engineering,
Cullen College of Engineering
in partial fulfillment of the requirements for the degree of

Doctor of Philosophy

in Materials Science & Engineering

Chair of Committee: Jiming Bao

Committee Member: Richard C. Willson

Committee Member: Paul Ruchhoeft

Committee Member: Xiaonan Shan

Committee Member: Tianfu Wu

University of Houston
December 2020

Copyright 2020, Guang Yang

Dedication

This dissertation is dedicated to my grandfather, Guochang Yang, who passed away four months before my Ph.D. graduation due to an unexpected disease. May he rest in peace in heaven and bless my future.

Acknowledgments

First, I want to express my sincere gratitude to my advisor, Dr. Jiming Bao, for his generous support and excellent mentorship during the past four years at the University of Houston. He has provided me this great opportunity to study and work in his lab with various outstanding scholars. His diligent work, critical thinking, creative ideas, and enthusiasm for the truth have inspired and guided me to achieve my goals.

I would also like to thank my parents, Shengyu Yang and Xia Wang, for their unconditional and everlasting love throughout the 30 years of my life. They are always believing in me and supporting me selflessly. They respect and trust every decision I have made. They empower me to be persistent in going beyond myself and moving forward without stopping. I love them forever.

Next, I want to thank my current and previous colleagues, Tian Tong, Xinxin Xing, Mohammadjavad Mohebinia, Cristal Solares, Zhoulyu Rao, Ye Zhang, Bo Yu, Sicong Sun, Chunzheng Wu, Shuai Yue, Shenyu Dai, Zhaojun Qin, Shengyang Xue, Fan Qin, Zhenghuan Zhao, Zhuan Zhu, Yanan Wang, and Kamrul Alam, for their help during my Ph.D. study, work and life.

Special appreciations are given to Feng Lin and his wife, Jiao Guo. I have learned a lot from them during my working and living.

Then, I would like to thank my landlord, Mrs. Shirin Rasheed, who is a very nice lady and provides me with a comfortable living environment.

Additionally, I want to give thanks to my good friends, Rui Ma, Yu Zheng, Miao Wang, Linghao Liu, and Yaxi Li, who have given me great encouragement and emotional support during my worst tribulations.

Finally, I would like to show my gratitude to all the other people who have helped and supported me during my life.

Abstract

Nanohole arrays in metal films have many amazing optical properties based on the surface plasmon resonance, which makes it popular in the sensing field. Usually, the change of the refractive index on the metal surface of nanohole arrays, caused by the binding of an analyte, can be reflected on the peak shift or intensity change of the transmission or reflection spectra. As sensing components, nanohole arrays provide many important advantages, including high reproducibility, miniaturization, the ability to integrate with other techniques, the capability of high-throughput analysis, and so on. Nanohole array sensing is quite compatible with the lab-on-chip technology and meets the tendency of point-of-care diagnostics that have been dramatically developed in recent years. Point-of-care diagnostics require low cost and portable devices with reliable and robust sensitivity for special analytes such as viruses. With the help of the nanohole arrays, the individual molecule of nanoscale size can be directly and precisely located. In this work, we have fabricated nanohole arrays with 150 nm diameter and 2 μm period, which have a larger period than those reported by other papers. Silica-shelled gold nanospheres with 70 nm core diameter and 20 nm shell thickness are used to block the nanoholes; and darkfield imaging system is used to obtain the images by the CCD and spectra by the spectrometer. The images and spectra of the nanoholes blocked by the individual nanospheres are analyzed and compared with those of the nanoholes before blocking. Results show a significant reduction of the light intensity in the blue and green light regions but an unusual

enhancement in the red light region. FDTD simulations are also conducted to not only confirm the experimental results but also provide the information about the position and the size of the nanospheres inside the nanoholes, and the wavelength of the exciting light. Furthermore, we demonstrate that our nanohole array samples can be integrated into a home-made inexpensive darkfield microscope and analyzed by a smartphone with an application developed by ourselves, which make it viable for future POC diagnostics.

Table of Contents

Dedication	iii
Acknowledgments	iv
Abstract	vi
Table of Contents.....	viii
List of Table	xii
List of Figure.....	xiii
Chapter 1 Introduction and Background.....	1
1.1 Introduction.....	1
1.2 Surface Plasmon of Nanohole in Metal Films	2
1.3 Configuration of Nanohole Array Sensors	7
1.4 EOT of Nanohole Arrays.....	8
1.5 Working Mechanism of Nanohole Array Sensors.....	13
1.6 Nanohole Array Biosensor Applications	15
1.7 Challenge, Motivation, and Scope of this Dissertation	17
Chapter 2 Nanohole Array Fabrication.....	19
2.1 Introduction.....	19
2.2 Electron Beam Lithography.....	21
2.2.1 Fabrication process	21
2.2.2 Dose control of e-beam lithography	22

2.2.3	Comparison of circular and square nanoholes.....	24
2.2.4	Comparison of wet etching and dry etching.....	25
2.3	Nanoimprint Lithography.....	28
2.3.1	Fabrication process	28
2.3.2	Etching rate of SiO ₂ by C ₄ F ₈ and O ₂	30
2.3.3	Etching rate of SiO ₂ by CHF ₃ and O ₂	31
2.3.4	Performance of the anti-stick layer.....	33
2.3.5	Etching rate of the mr-I 7030R resist by O ₂ plasma	34
2.3.6	Etching rate of the 495 PMMA by O ₂ plasma	37
2.3.7	Comparison of 30 s mold and 50 s mold after nanoimprint.....	40
2.4	Optimized Performance of Electron Beam Lithography and Nanoimprint Lithography.....	42
2.5	Conclusions.....	43
Chapter 3 Imaging Analysis of the Nanohole Array by Darkfield Setup		45
3.1	Introduction.....	45
3.2	Results and Discussion	46
3.2.1	The home-made darkfield imaging setup.....	46
3.2.2	Nanohole blocking experiment.....	48
3.2.3	Color analysis	52
3.2.4	Spectra analysis	53
3.2.5	Analysis of monochromatic light obtained by filters.....	55

3.2.6	Inexpensive darkfield device coupled with a smartphone	58
3.2.7	Filter test with inexpensive microscope darkfield setup	65
3.2.8	Optimized field of view and designed structure of the device	67
3.3	Conclusions.....	70
Chapter 4	Simulations.....	71
4.1	Introduction.....	71
4.1.1	FDTD Theory	74
4.1.2	The condition of the numerical stability	80
4.1.3	Numerical dispersion	81
4.1.4	Summary	82
4.2	Results and Discussion	82
4.2.1	Simulation configuration.....	82
4.2.2	Different sizes of the nanosphere.....	85
4.2.3	Different positions of the nanosphere	89
4.2.4	Different wavelengths of the exciting light	93
4.2.5	Positions of the nanosphere above the nanohole	94
4.3	Conclusions.....	96
Chapter 5	Smartphone Application of Nanohole Array Sensing	97
5.1	Introduction.....	97
5.2	Results and Discussion	98
5.2.1	Home page of the smartphone application	98

5.2.2	Global threshold and local threshold	99
5.2.3	Erosion and dilation operations	102
5.2.4	Calculation of the number of blocked nanoholes by the histogram and direct counting.....	104
5.3	Conclusions.....	109
Chapter 6 Conclusions and Perspectives		111
References.....		114
Appendices.....		131
A.	The analysis script of the simulation.....	131
B.	The smartphone application codes.....	133
i.	MainActivity.java.....	133
ii.	Label.java	148
iii.	FindThreshold.java	150
iv.	Threshold.java	152
v.	FindTforAnyRange.java.....	158
vi.	Morphology.java.....	160
vii.	SaveImage.java.....	162
viii.	activity_main.xml	164
ix.	AndroidManifest.xml.....	175
x.	strings.xml	176

List of Table

Table 2-1	Quality of nanohole arrays with different sizes under different doses.....	23
Table 2-2	Difference between the pre-set size and measured size of nanoholes under the dose of $700 \mu\text{C}/\text{cm}^2$	23
Table 2-3	Sizes of circular and square nanoholes measured from SEM images.....	28
Table 2-4	Recipe of etching SiO_2 with chromium as a mask.....	31
Table 2-5	Etching depth of SiO_2 measured by the profilometer and average etching rate of SiO_2 by C_4F_8 and O_2	31
Table 2-6	Recipe of etching SiO_2 with PMMA as a mask.....	32
Table 2-7	Etching depth of SiO_2 measured by the profilometer and average etching rate of SiO_2 by CHF_3 and O_2	32
Table 2-8	Recipe of the anti-stick layer coating.....	34
Table 2-9	Recipe of etching mr-I 7030R resist by O_2 plasma.....	35
Table 2-10	Vertical etching rate of the mr-I 7030R resist by different recipes.....	35
Table 2-11	Horizontal etching rate of the mr-I 7030R resist.....	37
Table 2-12	Vertical etching rate of the 495 PMMA by O_2 plasma.....	37
Table 2-13	Horizontal etching rate of the 495 PMMA by O_2 plasma.....	39
Table 3-1	Smartphone microscopes compared with the professional microscope.....	61
Table 3-2	Practical performance of the inexpensive microscope with different combinations of eyepieces and objectives.....	63

List of Figure

Figure 1-1	(a) SEM image and transmission spectra of isolated cylindrical nanohole in the silver film with different thickness h . (b) SEM image and transmission spectra of isolated rectangular nanohole. ^[4]	3
Figure 1-2	Scattering spectra normalized by the hole area of isolated circular nanohole with diameter D in 20 nm thin gold film. ^[5]	4
Figure 1-3	Scattering spectra of isolated circular nanohole with (a) 220 nm and (b) 150 nm diameter in the gold film with different thickness T . ^[6]	4
Figure 1-4	(a) SEM image and near field images of isolated circular nanohole in thin gold film. (b) Transmission spectra of gold film, isolated nanohole, and nanohole arrays. All diameters are 250 nm and the period is 2 μm . ^[7]	5
Figure 1-5	(a) Transmission spectra of chromium film and isolated chromium nanohole with and without a gold nanoparticle. (b) Transmission spectra normalized by chromium background. ^[8]	6
Figure 1-6	(a) Scattering spectra with incident light of different polarizations. (b) Transmission spectra of aluminum nanoholes with and without a gold nanoparticle. ^[9]	6
Figure 1-7	Nanohole array sensors with different configurations. ^[10-15]	8
Figure 1-8	Simulated transmission spectra of hexagonal nanohole arrays in the air with varying hole diameters. ^[17]	9

Figure 1-9	(a) Schematic of the cylindrical nanohole array, (b) side view of a single nanohole, and simulated transmission spectra of the nanohole arrays with different film thickness h when $R = 300$ nm and $P = 1500$ nm. ^[18]	10
Figure 1-10	(a) Simulation results and (b) experimental results of the transmission spectra for different adhesion layers between the gold film and Pyrex substrate. ^[19]	10
Figure 1-11	Optical microscope images of nanohole arrays in aluminum films. ^[20]	12
Figure 1-12	Optical transmission spectra of the square-lattice nanohole arrays with different periods in the gold metal film on a Pyrex substrate. ^[23]	12
Figure 1-13	Examples of the (a) reflection-based and (b) transmission-based nanohole array sensors. ^[26,32]	14
Figure 1-14	(a) Spectra of the sensor when exposed to different concentrations of acetone vapor balanced with dry air. (b) Peak wavelength vs. concentration of acetone vapors. ^[24]	14
Figure 1-15	(a) Unit cell of 3×3 nanohole array used for simulation. Simulation results of the gold nanoparticle (b) position-dependent and (c) size-dependent EOT transmission spectra of gold nanohole arrays. ^[48]	15
Figure 2-1	A typical fabrication process of gold nanohole array with e-beam writer and ion mill.....	21
Figure 2-2	SEM images of nanohole arrays of different size under different doses.	23
Figure 2-3	Circular and square nanoholes of different size under the same dose.....	24

Figure 2-4	SEM images of wet etching of the gold with PMMA mask under the same etching time by using KI/I ₂ solution of different concentrations.....	25
Figure 2-5	SEM images of gold films by dry etching with PMMA mask.....	26
Figure 2-6	SEM close-up images of the circular nanoholes with different sizes.....	27
Figure 2-7	SEM close-up images of the square nanoholes with different sizes.	27
Figure 2-8	A typical fabrication process of the mold for nanoimprint.....	29
Figure 2-9	A typical fabrication process of the gold nanohole array thin film by nanoimprint lithography.	30
Figure 2-10	Surface energy difference of the Si/SiO ₂ mold (a) with and (b) without the anti-stick layer.	34
Figure 2-11	SEM images of nanohole arrays imprinted on the mr-I 7030R resist after etching of (a) (b) (c) 3 min, (d) (e) (f) 4 min, and (g) (h) (i) 5 min.	36
Figure 2-12	SEM images of nanohole arrays imprinted on PMMA (a) (b) before etching and after etching of (c) (d) 3 min, (e) (f) 5 min, and (g) (h) 6 min.	39
Figure 2-13	(a), (b), (c), and (d) are the SEM images of 30 s mold. (e), (f), (g), and (h) are the SEM images of 50 s mold.	40
Figure 2-14	Performance of the 50 s mold imprinting on the PMMA.....	41
Figure 2-15	Schematic of the (a) 30 s mold and (b) 50 s mold.	41
Figure 2-16	SEM images of nanohole arrays fabricated by (a) e-beam lithography and (b) nanoimprint lithography.	42
Figure 3-1	Diagram of the light path through a darkfield microscope.....	46

Figure 3-2	Schematic of home-made darkfield setup for nanohole array imaging.....	47
Figure 3-3	Darkfield images of the nanohole array (a) before blocking and (b) after blocking experiment. The scale bars are both 10 μm	49
Figure 3-4	The corresponding areas of the SEM images and darkfield images. The circles in the SEM images show the nanoholes that are blocked by a single nanosphere. The scale bars are both 10 μm	51
Figure 3-5	RGB channels of the selected areas in the darkfield images. (a) and (b) shows 12 and 11 nanoholes respectively, and their corresponding intensity on the yellow line. The scale bars are both 10 μm	53
Figure 3-6	Spectra analysis of blocked and unblocked nanoholes. (a) Selected nanoholes. (b) Average spectra of blocked and unblocked nanoholes. (c) Intensity ratio according to (b). (d) Transmission spectra of gold film.	55
Figure 3-7	Transmission spectra of the (a) 450, (b) 550 and (c) 650 filters.	56
Figure 3-8	Professional microscope with darkfield condenser.	57
Figure 3-9	The darkfield images of the blocked nanohole array at the same area captured by the professional microscope (a) without filter, with (b) blue filter, (c) green filter, and (d) red filter. The scale bars are all 20 μm	58
Figure 3-10	Three types of smartphone microscopes.	59
Figure 3-11	The simple darkfield setup for smartphone microscope testing.	59

Figure 3-12 Images taken by the smartphone camera with different microscopes, (a) #1 microscope, (b) #3 microscope, and (c) professional microscope. The scale bars are 100 μm in (a) and (b), and 10 μm in (c).	61
Figure 3-13 The home-made darkfield setup by using an inexpensive learner’s microscope bundled with a smartphone holder. The eyepiece and the objective are 10X and 40X respectively.	64
Figure 3-14 Darkfield images of the nanohole array captured by smartphone with (a) professional and (b) inexpensive microscope. The nanohole array has 150 nm diameter and 2 μm period. The scale bars are both 10 μm	64
Figure 3-15 Darkfield images of the empty nanohole array, taken by a smartphone with RGB filters. The nanohole array has 150 nm diameter and 2 μm period. The scale bars are all 10 μm	66
Figure 3-16 The Bayer filter in the CMOS of the smartphone camera.	66
Figure 3-17 Darkfield images of the blocked nanohole array at the same area, taken by a smartphone. The nanohole array has 150 nm diameter and 2 μm period. The scale bars are both 10 μm	67
Figure 3-18 The optimized field of view of the monochromatic darkfield image taken by the inexpensive microscope coupled with the smartphone, which shows a 80 \times 80 blocked nanohole array. The scale bar is 20 μm	68
Figure 3-19 The designed structure of the device for point-of-care diagnostic.	69

Figure 4-1	Positions of the electric and magnetic field vector components in a cubic unit cell of the space lattice. The E-components are at the middle of the edges and the H-components are at the center of the faces.	78
Figure 4-2	The simulation configuration of the nanoholes structure. (a) Side view of the simulated area and (b) top view of the simulated area.	83
Figure 4-3	Polarizations of the incident light. Red arrows are propagating direction of the incident light. Blue arrows are polarization of the electric field. P polarization is in XZ plane and S polarization is in YZ plane.	84
Figure 4-4	The schematic of a simplified imaging system.	85
Figure 4-5	Near field intensity distributions of 488, 550, and 641 nm exciting light with P and S polarization. The right nanohole is blocked by a silica-shelled gold nanosphere with 70 nm core diameter and 20 nm thick shell.	86
Figure 4-6	Intensity ratios between the blocked and unblocked nanoholes at 488 nm wavelength of (a) P and (b) S polarizations for near field (red dots) and far field (black squares). The nanosphere is at the center of the nanohole.	88
Figure 4-7	Intensity ratios between the blocked and unblocked nanoholes at 550 nm wavelength of (a) P and (b) S polarizations for near field (red dots) and far field (black squares). The nanosphere is at the center of the nanohole.	88
Figure 4-8	Intensity ratios between the blocked and unblocked nanoholes at 641 nm wavelength of (a) P and (b) S polarizations for near field (red dots) and far field (black squares). The nanosphere is at the center of the nanohole.	88

Figure 4-9 Top view of the simulated structure with a nanosphere at the edge of the nanohole.....90

Figure 4-10 Intensity ratios between the blocked and unblocked nanoholes at 488 nm wavelength of (a) P and (b) S polarizations for near field (red dots) and far field (black squares). The nanosphere is at the edge of the nanohole.90

Figure 4-11 Intensity ratios between the blocked and unblocked nanoholes at 550 nm wavelength of (a) P and (b) S polarizations for near field (red dots) and far field (black squares). The nanosphere is at the edge of the nanohole.90

Figure 4-12 Intensity ratios between the blocked and unblocked nanoholes at 641 nm wavelength of (a) P and (b) S polarizations for near field (red dots) and far field (black squares). The nanosphere is at the edge of the nanohole.....91

Figure 4-13 Top view of the simulated structure with a nanosphere at the corner of the nanohole.....92

Figure 4-14 Intensity ratios between the blocked and unblocked nanoholes at 488 nm wavelength of (a) P and (b) S polarizations for near field (red dots) and far field (black squares). The nanosphere is at the corner of the nanohole.92

Figure 4-15 Intensity ratios between the blocked and unblocked nanoholes at 550 nm wavelength of (a) P and (b) S polarizations for near field (red dots) and far field (black squares). The nanosphere is at the corner of the nanohole.92

Figure 4-16	Intensity ratios between the blocked and unblocked nanoholes at 641 nm wavelength of (a) P and (b) S polarizations for near field (red dots) and far field (black squares). The nanosphere is at the corner of the nanohole.	93
Figure 4-17	Intensity ratios between the blocked and unblocked nanoholes at different wavelengths of the exciting light with the P and S polarizations.	94
Figure 4-18	Side views of the positions when the nanosphere is above the nanohole at the center position or edge position.	95
Figure 4-19	Intensity ratios between the blocked and unblocked nanoholes at 488, 550, and 641 nm wavelength of P and S polarizations. The nanosphere is above the nanohole at the center position or edge position.	95
Figure 5-1	The home page of the Nanohole_Array_Sensor application.	99
Figure 5-2	Original darkfield image processed by the global threshold and local threshold methods. The scale bars are all 10 μm	102
Figure 5-3	Separation of the connected nanoholes of the original darkfield image, which is processed first by the global threshold and then by the erosion and dilation operations. The scale bars are all 10 μm	104
Figure 5-4	Elimination of the noisy point of the original darkfield image, which is processed first by the global threshold and then by the erosion and dilation operations. The scale bars are all 10 μm	104
Figure 5-5	Darkfield images and histograms of empty nanohole arrays (a) without green filter and (b) with green filter. The scale bars are both 10 μm	106

Figure 5-6 (a) Example of the darkfield image analyzed by the smartphone application, (b) the darkfield image by microscope, (c) its threshold image, and (d) intensity histogram of the nanoholes. The scale bars are both 6 μm 107

Figure 5-7 (a) Example of the darkfield image analyzed by the smartphone application, (b) the darkfield image by smartphone, (c) and (d) threshold images, and (e) the darkfield image by CCD. The scale bars are all 10 μm 109

Chapter 1 Introduction and Background

1.1 Introduction

Nanohole arrays are a kind of nanostructure consisting of many nanoscale voids fabricated on a metallic surface, such as Au, Ag, Al, and so on. In 1998, Ebbesen's group discovered the unusual phenomenon on metallic substrates with sub-wavelength holes, called extraordinary optical transmission (EOT), where the transmission of the light at certain wavelengths can have a large enhancement.^[1] This finding disagrees with the understanding founded by Bethe that the light transmission through a sub-wavelength aperture should be very weak.^[2] Since then, the single nanohole and nanohole array in metal films have been a major research field. Years of studies indicate that the fascinating optical properties including EOT of the nanohole arrays are closely related to the surface plasmon resonances (SPR), which can have a variety of promising applications for optical detections in chemical and biomedical fields.

The point-of-care (POC) applications have been developed dramatically in recent years and continue to expand rapidly to deliver inexpensive, portable, and reliable devices to meet the demands of on-site diagnostics and real-time healthcare. The tunability and flexibility of nanohole arrays provide an opportunity to design smaller, faster, and more efficient devices. Nanohole arrays are utilized for the POC diagnostic as SPR sensors, which offer many advantages such as real-time monitoring, label-free recognition of ligands or analytes, low sample volumes, reusability, repeatability, allowing testing on

crude samples without purification, ability for multiplex sensing of several analytes, possibility of optical integrations, and high-density packing.^[3]

1.2 Surface Plasmon of Nanohole in Metal Films

In previous work, investigators have studied how local surface plasmons influence the transmission properties of the isolated nanohole on optically thick suspended silver films.^[4] For a single cylindrical nanohole, the transmission spectra show a resonance peak whose intensity decreases rapidly with increasing thickness of the silver film, shown in Figure 1-1 (a). For a single rectangular nanohole, the transmission spectra can have a strong polarization effect, and the peak height of the transmission resonance increases with its peak shifting to larger wavelengths as the aspect ratio is enlarged, shown in Figure 1-1 (b). In a different work, researchers have shown that the darkfield scattering spectra of optically thin gold films perforated by a single circular nanohole exhibit an optical resonance in the visible range, which is assigned to a dipolar localized surface plasmon at the hole circumference, shown in Figure 1-2.^[5] Another work has also observed resonance in the darkfield scattering spectra of a single nanohole in the thin gold film.^[6] It has been claimed that film plasmons can induce a large dipole moment across the nanohole which thus mediates coupling between these specific film plasmons and an incident electromagnetic wave. The wavelength of the dipole-active film plasmons increases with increasing hole diameter, which results in red-shifted wavelength of the hole resonance, and a redshift of the wavelength of the hole resonance is expected as film thickness decreases, shown in

Figure 1-3. Another work has studied how the surface plasmon polariton (SPP) can influence the transmission properties of nanoholes in the thin gold film by using near field scanning optical microscopy and far field spectroscopic measurements.^[7] Noticeably, even though the SPPs have been observed in the near field images shown in Figure 1-4 (a), the SPP band is not present in the spectrum of the isolated hole shown in Figure 1-4 (b). For nanohole arrays, SPPs launched from one hole can be coupled back to free space light by scattering from adjacent holes, and hence the optical transmission can be enhanced by SPPs. For thicker films, a greater enhancement is expected because the decay of light through the gold film is greater than that of the SPPs through the nanoholes, shown in Figure 1-4 (b).

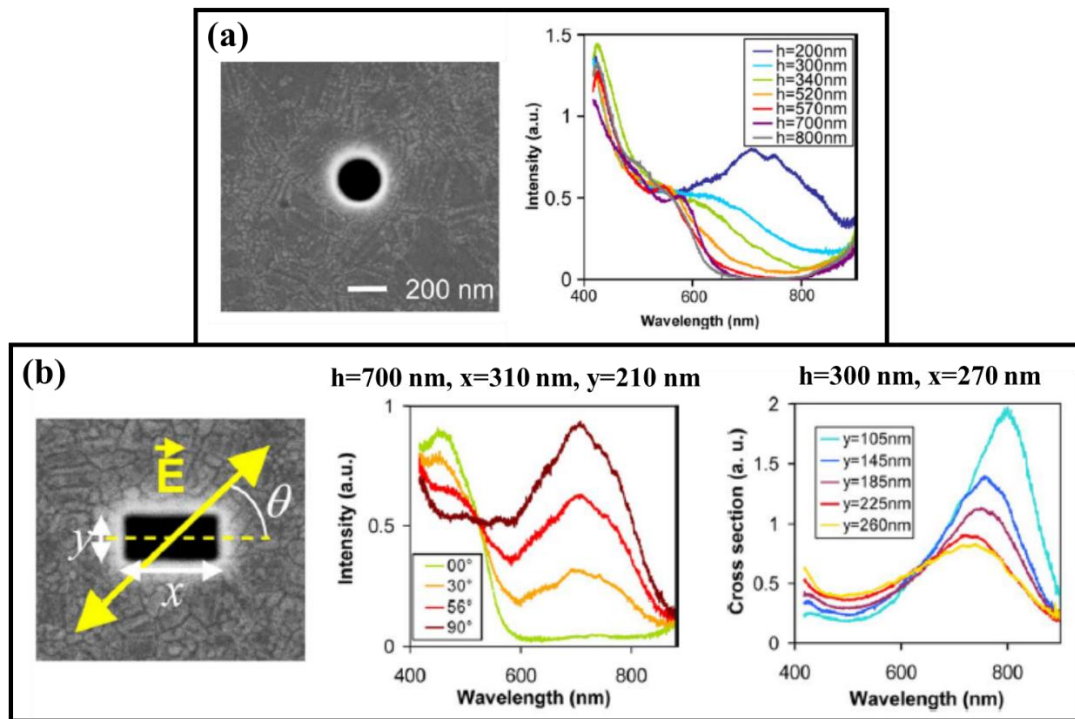


Figure 1-1 (a) SEM image and transmission spectra of isolated cylindrical nanohole in the silver film with different thickness h . (b) SEM image and transmission spectra of isolated rectangular nanohole.^[4]

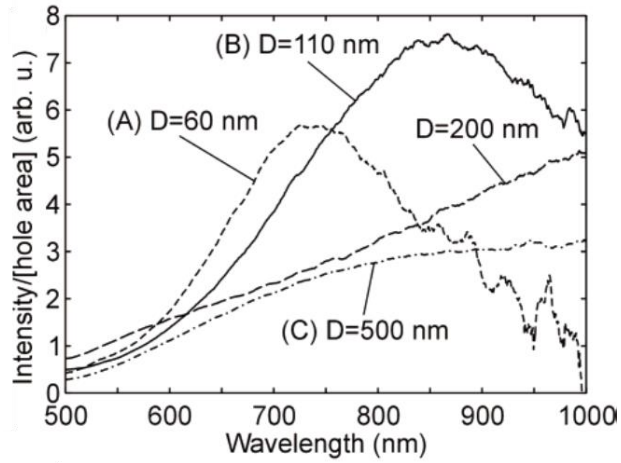


Figure 1-2 Scattering spectra normalized by the hole area of isolated circular nanohole with diameter D in 20 nm thin gold film.^[5]

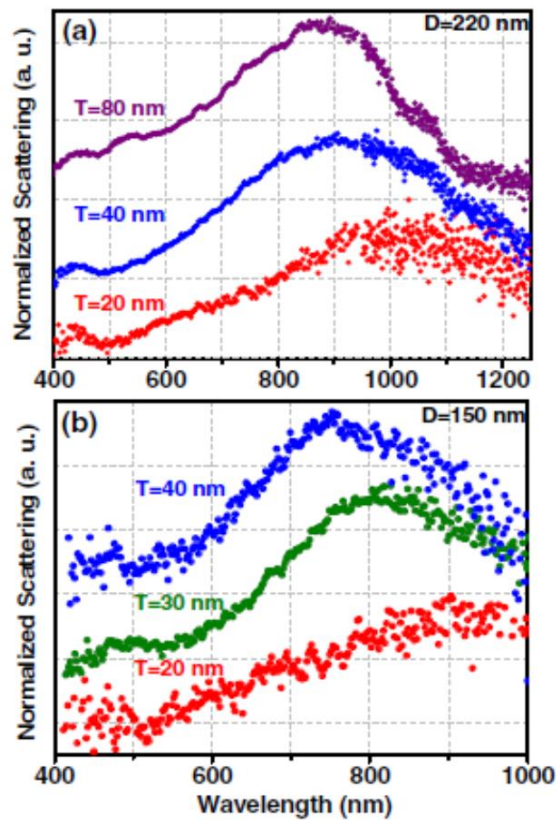


Figure 1-3 Scattering spectra of isolated circular nanohole with (a) 220 nm and (b) 150 nm diameter in the gold film with different thickness T .^[6]

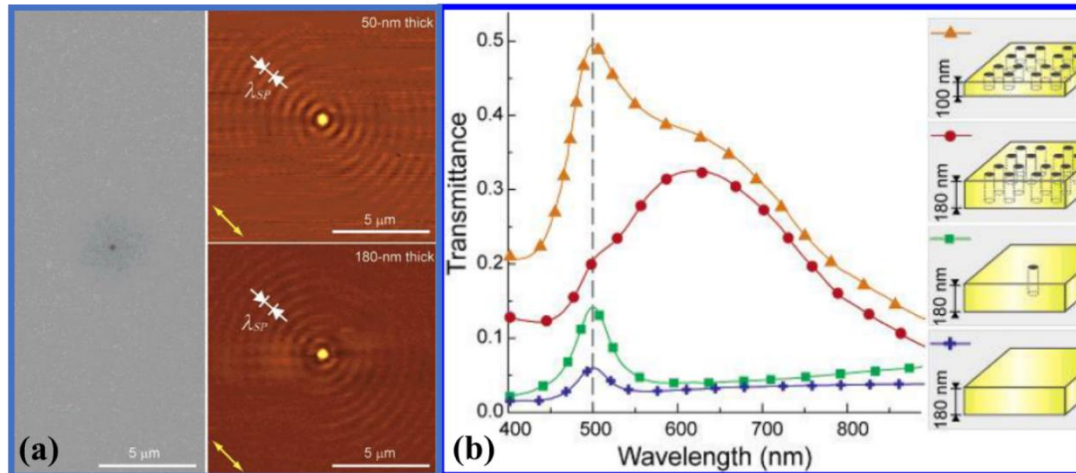


Figure 1-4 (a) SEM image and near field images of isolated circular nanohole in thin gold film. (b) Transmission spectra of gold film, isolated nanohole, and nanohole arrays. All diameters are 250 nm and the period is 2 μm .^[7]

On the other hand, some people have also studied the spectroscopic behavior of isolated nanohole containing one nanoparticle. For example, Jahr's group studied the transmission spectra of the isolated chromium nanohole with and without a gold nanoparticle by normalizing the spectra to light source and chromium background, shown in Figure 1-5.^[8] It indicates that the nanoparticle causes a decrease in the light transmission for wavelengths shorter than 550 nm and an increase in the light transmission for longer wavelengths. In another work, Lumdee's group has investigated the gap-plasmon resonance of a gold nanoparticle inside a circular nanopore in an aluminum film by measuring transmission spectra and darkfield scattering spectra.^[9] Figure 1-6 (a) shows the darkfield scattering spectra of an isolated aluminum nanohole containing one gold nanoparticle when the incident light has different polarizations. The resonance peaks for both polarizations are nearly at the same location and have a little difference in intensity

and width. For the transmission spectra shown in Figure 1-6 (b), the isolated aluminum nanohole doesn't show any resonance peak while the one with a gold nanoparticle has a large resonance peak at about 670 nm. This transmission peak matches the scattering peak suggesting that the sidewall gap plasmon mode can be efficiently excited over a broad angular range.

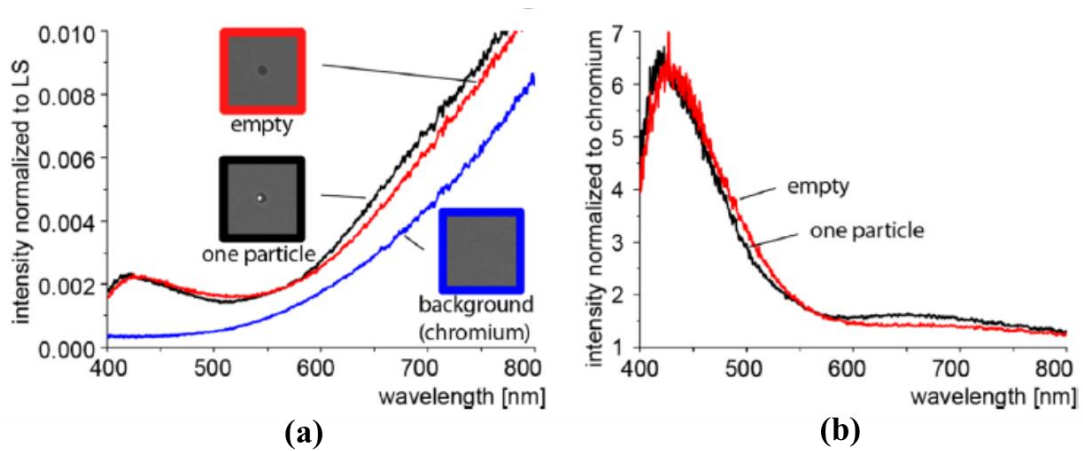


Figure 1-5 (a) Transmission spectra of chromium film and isolated chromium nanohole with and without a gold nanoparticle. (b) Transmission spectra normalized by chromium background.^[8]

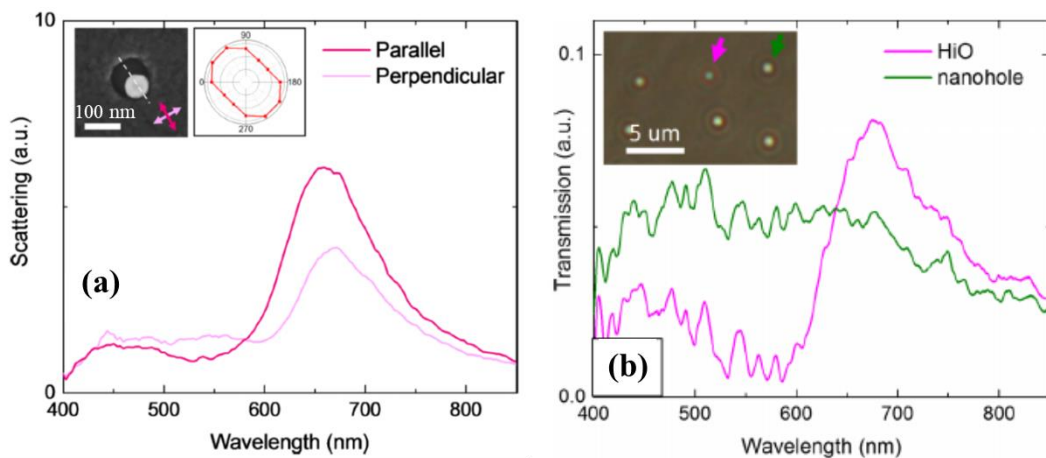


Figure 1-6 (a) Scattering spectra with incident light of different polarizations. (b) Transmission spectra of aluminum nanoholes with and without a gold nanoparticle.^[9]

1.3 Configuration of Nanohole Array Sensors

Since nanohole arrays exhibit many useful optical properties, they have been used for sensing applications. According to the physical structures of the nanohole array sensors that have been reported, there are some typical types of structures that are mostly studied, shown in Figure 1-7. Figure 1-7 (a) shows the nanoholes in a metal film on the glass or quartz substrate^[10], and Figure 1-7 (b) shows the nanoholes in the top metallic layer of a metal-dielectric-metal sandwich film on the glass or quartz substrate^[11]. Figure 1-7 (c) shows the nanoholes in a metal film with metallic nanodiscs at the bottom of the nanoholes^[12], and Figure 1-7 (d) shows the suspended nanoholes in a metal film and SiN thin film^[13]. Figure 1-7 (e) shows the convex nanoholes in a metal film fabricated by the nanosphere lithography^[14], and Figure 1-7 (f) shows the nanoholes in a metal film and the substrate with the sidewall and bottom covered by a metallic layer^[15]. Additionally, some other nanohole array structures similar to these or modified from these also exist.

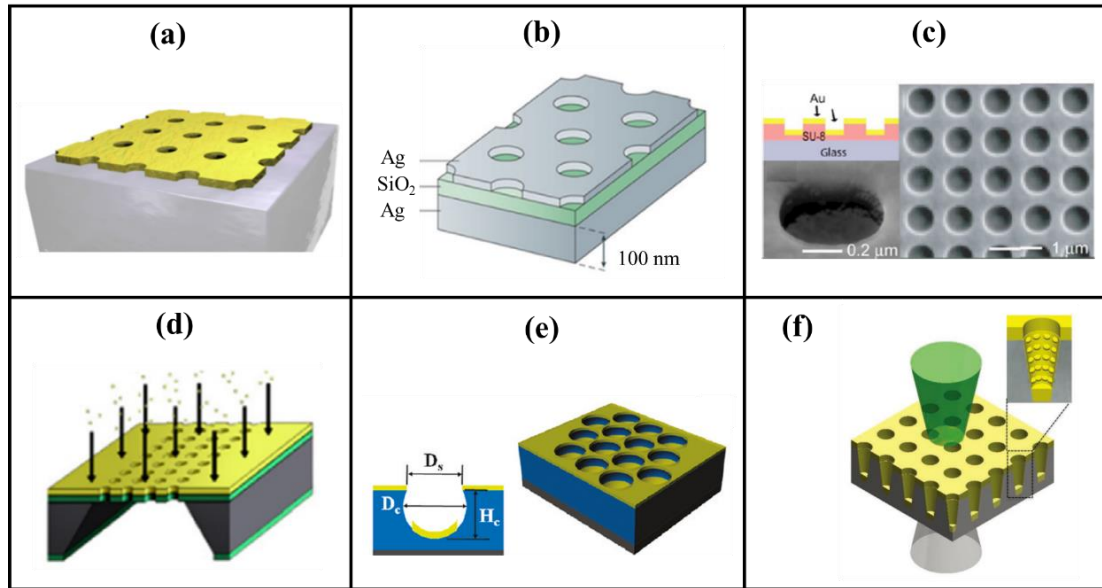


Figure 1-7 Nanohole array sensors with different configurations.^[10-15]

1.4 EOT of Nanohole Arrays

Light transmission through a hole is theoretically proportional to $(r/\lambda)^4$ given by Bethe, where r is the hole radius and λ is the light wavelength.^[2] Thus, for sub-wavelength holes, when $r \ll \lambda$, the transmission of light should be close to zero. However, later studies show that the transmission of light can be three or four orders of magnitude higher than the previous theoretical results when the sub-wavelength nanoholes are fabricated on some of the metal films such as Au, Ag, and Al.^[1,16] This extraordinary optical transmission of light results from the SPR and diffraction of light waves generated on the metal-dielectric interface of the plasmonic nanoholes. The performance of EOT in the nanohole arrays is dependent on various factors, such as the periodicity of the nanohole array, the diameter of the nanoholes, the thickness of the metal film, the order of the nanohole, the shape of the nanoholes, the adhesion layer of the metal film, and so on.

For example, Ohno's group has measured and simulated transmission spectra of the triangular-lattice nanohole array with different nanohole sizes.^[17] Their simulation results show that the resonance wavelengths of the transmission peaks and dips vary within a small range when the diameter of the nanoholes increases, shown in Figure 1-8. The intensities of the peaks and dips have obvious changes as well. Chen's group has simulated the transmission spectra of cylindrical nanohole arrays in the gold film of different thickness on SiO₂ substrate.^[18] Usually the thickness of the metal film only influence the peak intensity, shown in Figure 1-9. For the factor of the adhesion layer between the metal and the dielectric substrate, the simulated and experimental results have also been obtained by Najiminaini's group, shown in Figure 1-10.^[19] The transmission spectra can have a large difference due to the thickness and the material of the adhesion layer.

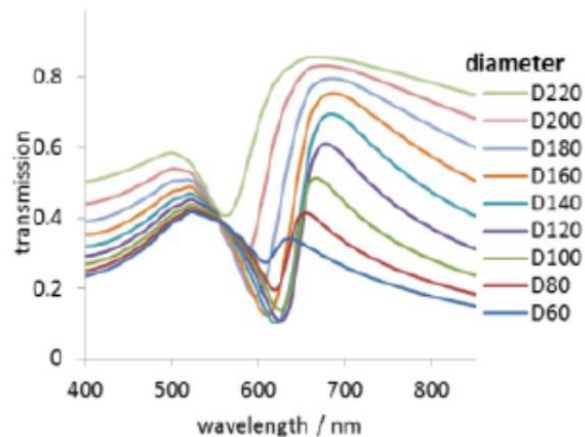


Figure 1-8 Simulated transmission spectra of hexagonal nanohole arrays in the air with varying hole diameters.^[17]

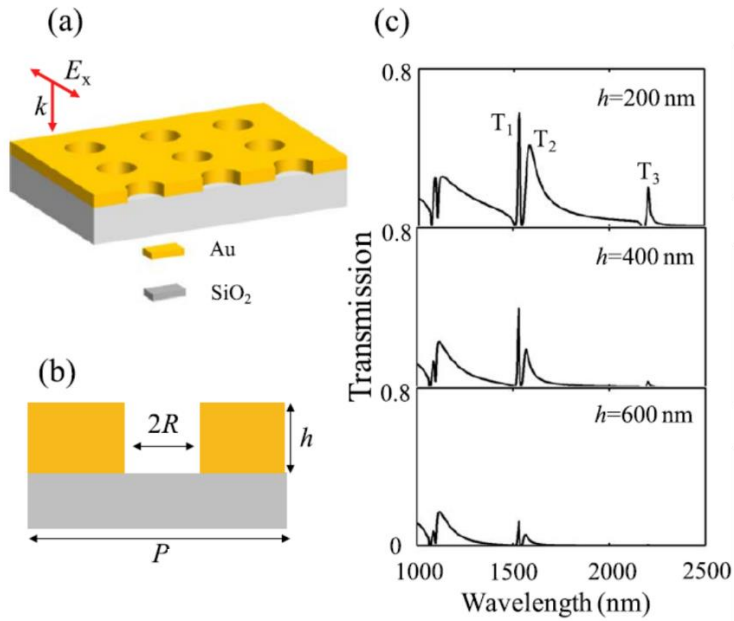


Figure 1-9 (a) Schematic of the cylindrical nanohole array, (b) side view of a single nanohole, and simulated transmission spectra of the nanohole arrays with different film thickness h when $R = 300$ nm and $P = 1500$ nm.^[18]

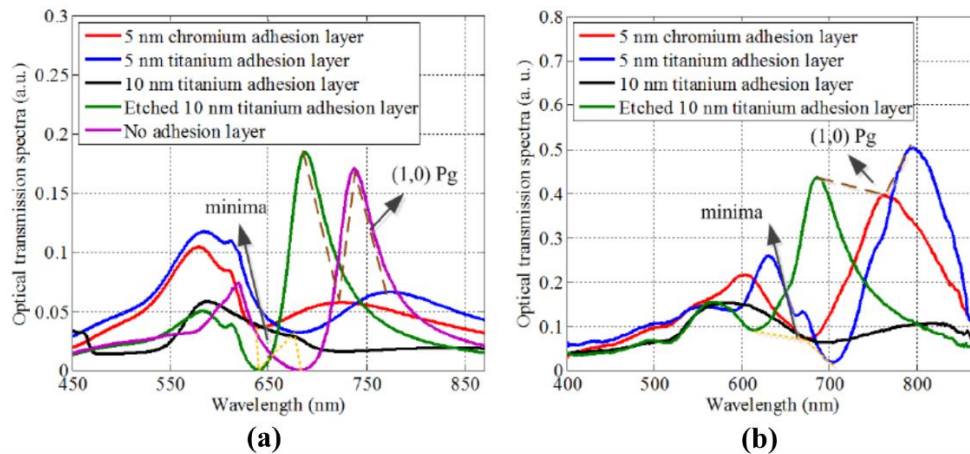


Figure 1-10 (a) Simulation results and (b) experimental results of the transmission spectra for different adhesion layers between the gold film and Pyrex substrate.^[19]

However, one of the most important factors, which affect the performance of the EOT in nanohole arrays, is the periodicity of the nanohole arrays. Figure 1-11 shows colorful microscope images of different kinds of nanohole arrays in the aluminum film with various

periods, obtained by Inoue's group.^[20] The periods of the nanohole arrays are changing from 200 nm to 700 nm with a 20 nm increment, which can result in plenty of colors of the transmission light. Their experiments also show that the transmission spectra have an obvious response to the shape and order of the nanohole arrays. Generally, for the square-lattice nanohole arrays in the metal film, the peak position of the transmission spectrum at normal incidence is given by

$$\lambda_{peak}(i, j) = \frac{p}{\sqrt{i^2 + j^2}} \sqrt{\frac{\epsilon_m \epsilon_d}{\epsilon_m + \epsilon_d}}, \quad (1 - 1)$$

where p is the period of the array, i and j are integer numbers representing scattering orders from the 2D array, and ϵ_m and ϵ_d are the dielectric constants of the metal and the dielectric material, respectively.^[21] While for the triangular-lattice nanohole arrays in the metal film, the peak position of the transmission spectrum at normal incidence is given by

$$\lambda_{peak}(i, j) = \frac{p}{\sqrt{\frac{4}{3}(i^2 + ij + j^2)}} \sqrt{\frac{\epsilon_m \epsilon_d}{\epsilon_m + \epsilon_d}}. \quad (1 - 2)$$

But these two equations are derived neglecting the interference that will give rise to a resonance shift because they don't take into account the presence of the nanoholes and the associated scattering losses. Thus, the wavelengths of the peak positions they predict are slightly shorter than those observed experimentally.^[22] Figure 1-12 shows the optical transmission spectra of the square-lattice nanohole arrays with different periods in the gold metal film on a Pyrex substrate.^[23] The (1, 0) and (1, 1) resonance peaks are indicated by

the black arrows. The shift of the resonance peaks is very sensitive to the change of the nanohole array period.

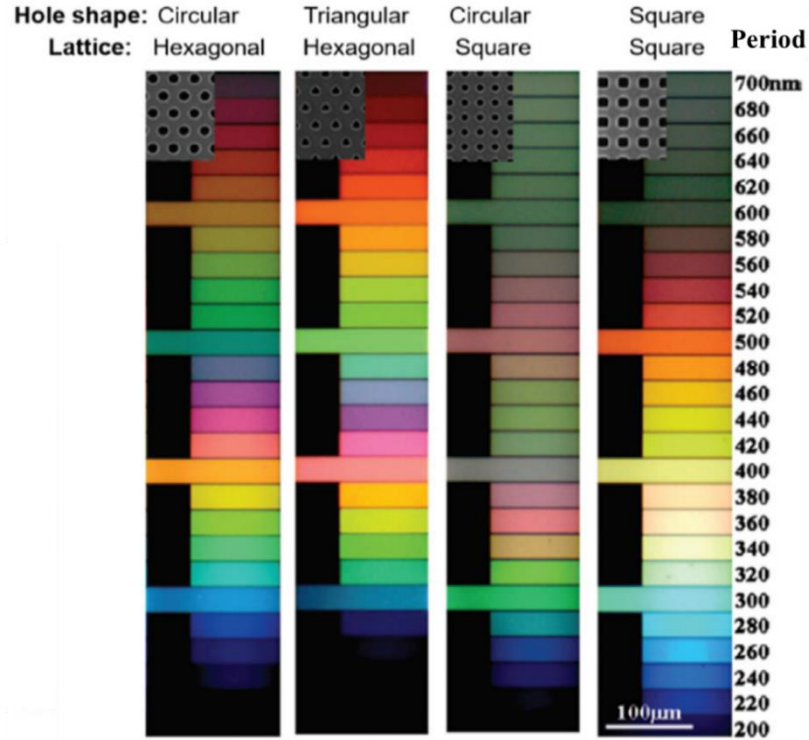


Figure 1-11 Optical microscope images of nanohole arrays in aluminum films.^[20]

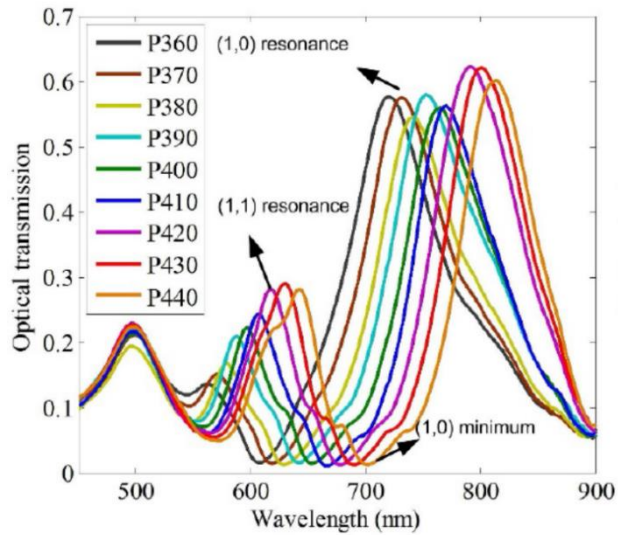


Figure 1-12 Optical transmission spectra of the square-lattice nanohole arrays with different periods in the gold metal film on a Pyrex substrate.^[23]

1.5 Working Mechanism of Nanohole Array Sensors

For the nanohole array sensors, there are usually two modes of SPR detection according to the configuration of the measurement setup, namely reflection mode^[24-26] and transmission mode^[10,27-43]. Figure 1-13 (a) and (b) shows two typical setups of the reflection-based and transmission-based nanohole array sensors, respectively.^[26,32] Simply, the illuminating light and detector are on the same side of the sensor in the reflection mode while the illuminating light and detector are at the opposite sides of the sensor in the transmission mode. If considering the parameters analyzed during the measurement, the nanohole array based biosensors can be generally classified into two categories, which are the wavelength shift mode^[10,24-37,44-47] and the light intensity mode^[24,37-43,48,49]. According to Equation 1-1 and 1-2, the SPR peak wavelength is sensitive with the dielectric constant change of the material contacting the metal surface. The molecules binding on the metal surface can change the refraction index of the sample side, which can result in the change of its dielectric constant. As a consequence, the transmission or reflection spectra measured can be different from the one without the molecule binding. Usually, an obvious shift of the SPR peak can be observed in the transmission or reflection spectra. Figure 1-14 shows an example of the SPR peak shift.^[24] The peak wavelength has a redshift with the increasing concentration of the acetone vapor, shown in Figure 1-14 (a). Thus, the concentration of the acetone vapor can be measured by calibrating the curves shown in Figure 1-14 (b). On the other hand, the transmission or reflection intensity of the spectra can change as well

when the molecule is binding on the surface of the metal film or inside the nanohole. Usually, an obvious intensity reduction of the SPR peak or certain wavelength can be observed in the spectra. Figure 1-15 (a) shows the simulated model of a unit cell with a 3×3 nanohole array. When the gold nanoparticle is close to the nanohole or inside the nanohole, the peak intensity of the transmission spectra can have a pronounced reduction, shown in Figure 1-15 (b). Additionally, the peak intensity of the transmission spectra decreases with the increase of the gold nanoparticle size, shown in Figure 1-15 (c).^[48]

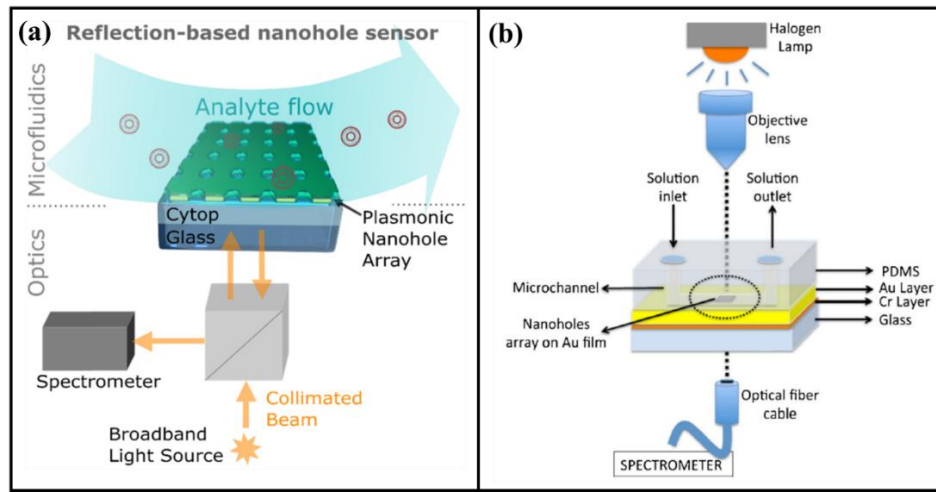


Figure 1-13 Examples of the (a) reflection-based and (b) transmission-based nanohole array sensors.^[26,32]

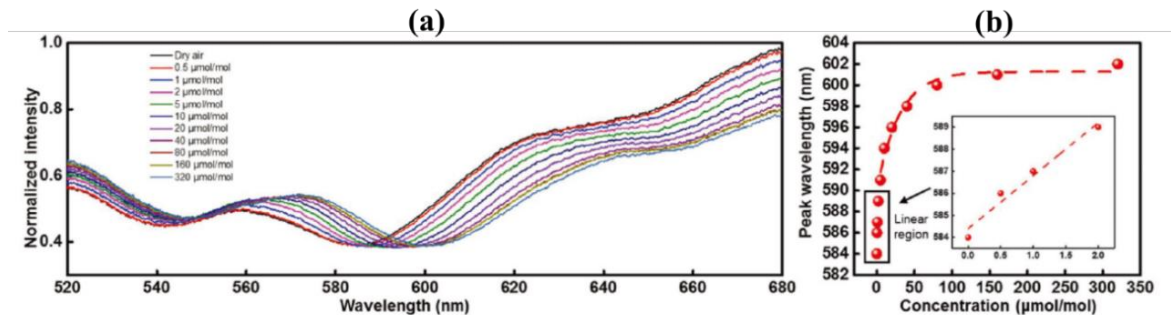


Figure 1-14 (a) Spectra of the sensor when exposed to different concentrations of acetone vapor balanced with dry air. (b) Peak wavelength vs. concentration of acetone vapors.^[24]

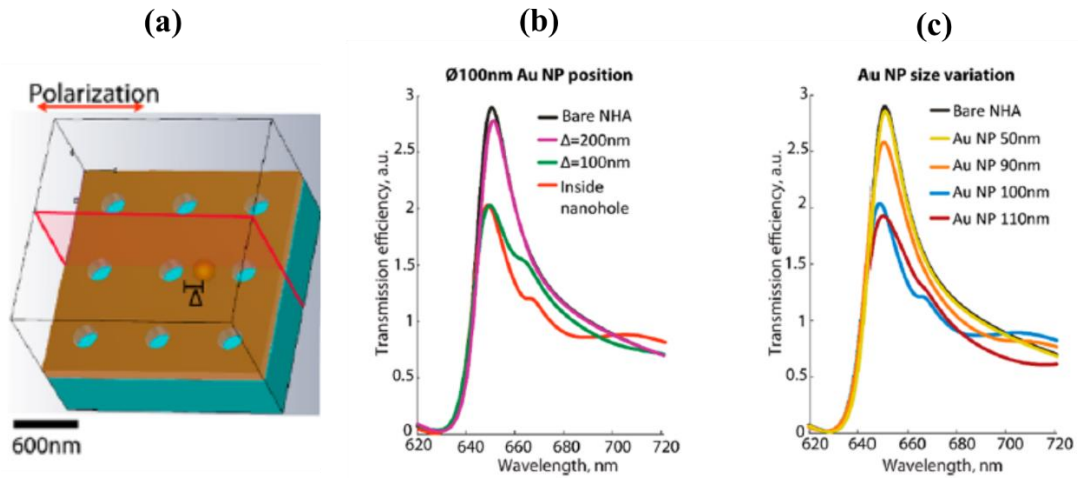


Figure 1-15 (a) Unit cell of 3×3 nanohole array used for simulation. Simulation results of the gold nanoparticle (b) position-dependent and (c) size-dependent EOT transmission spectra of gold nanohole arrays.^[48]

1.6 Nanohole Array Biosensor Applications

One of the popular applications of the nanohole array sensors is biomolecular assays. Traditional diagnostic equipment for infectious diseases such as enzyme-linked immunosorbent assays, polymerase chain reaction, and cell culture usually cannot meet the criteria of the POC diagnostics. With the increasing development of POC diagnostics and demand for fast and inexpensive healthcare in resource-limited regions in recent years, the nanohole array based biosensors are being developed to integrate into the compact, inexpensive and portable devices to perform on-site measurements and analysis. Investigators have made substantial efforts to improve the reliability of these POC devices, such as the sensitivity, specificity, selectivity, repeatability, and limit of detection. Although there are still many optimizations that need to be done before final large-scale commercialization, many prototypes of the miniaturized devices have been proposed to

detect cells, proteins and pathogens. Usually, the concentration of the analyte can be derived according to the peak wavelength shift or the intensity change of the spectra as explained in the previous part.

By using the bio-recognition molecules such as avidin, streptavidin, biotin, cell-derived vesicles for efficient ligand-receptor binding to attain high sensitivity and specificity, protein detection can be achieved. In a previous study, it has demonstrated the detection of exosomes, a cell-derived vesicle involved in the transport of molecular contents of cancer like cells, on the nanohole array sensors.^[29] Antibodies are immobilized on the nanohole array to detect proteins on the exosomes or in the exosome lysates. In another work, the gold nanohole arrays have been integrated with microfluidic devices to detect a cell-signaling protein TNF- α by performing immunoassay on the array.^[50] The TNF- α proteins with streptavidin-Au conjugate are trapped on the nanohole array by biotin-avidin coupling, which shows an SPR response that is proportional to the density of the protein layer.

For the pathogen detection, one group has used the 8G5, M-DA01-A5, and A33L antibodies immobilized on the surfaces of the nanohole array to achieve the specificity of the sensor to recognize vesicular stomatitis virus, Smallpox, and Ebola viruses.^[51] In a similar work, the lipid membranes over SiO₂-Au nanohole array surface have been used to detect pathogenic bacteria *Staphylococcus aureus* by measuring α -hemolysin, a hydrophilic peptide monomer secreted by the bacteria.^[52] Additionally, another group has

demonstrated real-time detection of uropathogenic *E. coli* for diagnosis of urinary tract infections using human urine samples by using a flow-through nanohole array sensor.^[53]

1.7 Challenge, Motivation, and Scope of this Dissertation

Almost all previous applications have implemented densely arranged nanohole arrays, whose periods usually are several hundred nanometers. These sensors utilize the whole effect of a large area nanohole array, while the effect of the individual nanoholes are usually not concerned about in their configurations. Even though one group has showed that an individual nanoparticle inside the nanohole of a close-packed nanohole array can be detected by the transmission intensity change, it is influenced a lot by the background noise.^[48] Also, it cannot distinguish two adjacent nanoholes when they both capture an individual nanoparticle. However, with the help of the nanohole array sensors with an enlarged period, more precise single virus detection with inexpensive and compact devices has a great chance to be achieved. The goal of this dissertation is to demonstrate that the single nanoparticle, captured in the gold nanohole array with an enlarged period, can be easily recognized and precisely located with an inexpensive home-made microscope setup by darkfield imaging, which makes the single virus detection by the optical device for POC diagnostics possible in the coming future.

This dissertation contains four sections. The first section introduces the fabrication methods that have been utilized to manufacture uniform and robust gold nanohole arrays. We have exploited e-beam lithography to achieve small scale and reliable fabrication, and

nanoimprint lithography to perform inexpensive and high-throughput fabrication of the gold nanohole array with the optimized configuration. The second section shows the optical imaging analysis of the nanohole arrays blocked by the nanoparticles. The darkfield setup is used and a home-made darkfield microscope setup with an inexpensive microscope has been established. The spectra analysis and digital image analysis of the individual nanoholes have been conducted by the spectrometer and computer software, respectively. The third section gives the simulation results of the near field and far field by modeling two nanoholes with one of them blocked by a single nanoparticle. The position of the nanoparticle inside the nanohole and the size of the nanoparticle have been changed to obtain a series of results under different conditions. These results have been compared with those observed in the second section. The fourth section develops a prototype of a smartphone application that can be used to analyze the darkfield images obtained by the inexpensive home-made darkfield imaging system. This provides the possibility to miniaturize the proposed imaging system for POC diagnostics under further optimization in the future.

Chapter 2 Nanohole Array Fabrication

2.1 Introduction

Microscale and nanoscale patterns can be fabricated by various of methods. As the scale decreases, the difficulty of fabrication increases. After decades of research, subwavelength nanohole array with high quality of uniformity can be easily fabricated by several methods, such as focused ion beam (FIB)^[32,39-42,54-59], electron beam (e-beam) lithography^[19,27,42,60-62], nanoimprint lithography^[62-65], nanosphere lithography^[66-70], interference lithography^[30,31,71-77] and so on. All these methods have their advantages and disadvantages.

FIB and e-beam lithography are expensive methods since they require high-level vacuum and high power electric field. They are time-consuming for large area pattern fabrication. However, they both have a high resolution of about 10 nm and can directly write patterns on the sample or photoresist without masks.

Nanoimprint lithography is a low cost, high throughput, and high-resolution nanolithography method. A mold with desired patterns is used to print on the resist by pressure and the resist is typically cured by heat or UV light during the imprinting, thus called thermoplastic nanoimprint lithography or photo nanoimprint lithography, respectively.

Nanosphere lithography is an economical technique for generating hexagonally close-packed or similar patterns of nanoscale features. It usually uses a self-assembled monolayer

of latex or silica spheres as lithography masks to fabricate nanodot arrays or nanohole arrays with controlled spacings. It also needs some specific methods to deposit a single-layer of spheres, such as Langmuir-Blodgett, dip coating, spin coating, and solvent evaporation, etc.

Interference lithography is a simple technique for creating periodic arrays of line features without the use of complex optical systems or photomasks. For 2-beam interference, arrays with rectangular symmetry can be generated. While for 3-beam interference, arrays with hexagonal symmetry can be generated. In the previous work of our group, nanohole arrays with approximately 2 μm periodicity and 1 μm diameter have been produced by the interference lithography with a 363.8 nm laser.^[77] Usually, the interference fringes have a bright to dark ratio of 1 : 1. This means the diameter of nanoholes and the space between nanoholes are almost the same. Although one paper^[74] has reported that the diameter to periodicity ratio can be varied between 0.25 and 0.55 by changing the exposure time or the development time, a ratio smaller than 0.1, like 150 nm diameter and 2 μm periodicity, is beyond what can be achieved by interference lithography.

In this work, squared nanohole arrays with rectangular symmetry are fabricated. The diameter of nanoholes is reduced to 150 nm to make the nanohole size similar to the virus size, and the periodicity of nanohole arrays is still maintained at 2 μm for the convenience that individual nanoholes can be distinguished by the optical microscope. Considering the available equipment, time, cost, and throughput, these nanohole arrays are fabricated by two methods, e-beam lithography, and thermoplastic nanoimprint lithography.

2.2 Electron Beam Lithography

2.2.1 Fabrication process

A typical process to fabricate the nanohole array in the gold film with the e-beam writer and ion mill is shown in Figure 2-1. First, a 5 nm chromium thin film followed by a 95 nm gold thin film is deposited on the glass by the e-beam evaporator. Second, a PMMA layer with a thickness of about 350 nm is spin-coated on the top of the gold layer at 4000 rpm. After baking the substrate for 2 min at 180 °C, the nanohole array pattern with the desired diameter and period is written on the PMMA by the e-beam writer. Next, the sample is developed by the mixture of the IPA and water solution with a ratio of 2 : 1 for 90 s and dried by nitrogen. Then, the sample is etched by the ion mill for 3 min. Finally, the PMMA is removed by sonication in the hot acetone.

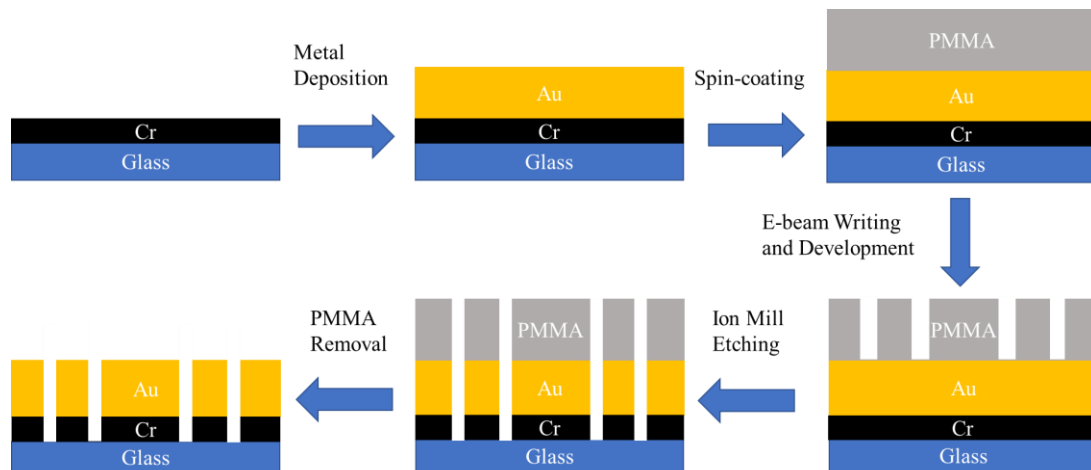


Figure 2-1 A typical fabrication process of gold nanohole array with e-beam writer and ion mill.

2.2.2 Dose control of e-beam lithography

To optimize the electron beam dose injected into the PMMA, a series of doses, from $400 \mu\text{C}/\text{cm}^2$ to $800 \mu\text{C}/\text{cm}^2$, have been applied. The silicon is used as the substrate spin-coated with the PMMA layer. A series of nanoholes with different sizes from 150 nm to 300 nm are designed in this experiment.

In Figure 2-2, the SEM images show the nanohole arrays with different sizes obtained in the PMMA film under different doses. For the dose of $400 \mu\text{C}/\text{cm}^2$, only the “T” type marker can be seen and none of the nanohole arrays can be detected. Also, some pictures with lower doses and smaller sizes show that the nanoholes have a vague outline, while the pictures with higher doses and larger sizes show that the nanoholes have a clear outline. These results show that the smaller the size is, the higher dose is needed. Table 2-1 has concluded the quality of the nanoholes under different conditions. The suitable dose is over $700 \mu\text{C}/\text{cm}^2$ for the size of 150 nm and over $600 \mu\text{C}/\text{cm}^2$ for the size from 200 nm to 300 nm. The sizes of nanoholes obtained under the dose of $700 \mu\text{C}/\text{cm}^2$ are also measured by SEM, which are shown in Table 2-2. The average size deviation of the four kinds of nanoholes is 4.6 %, which is acceptable. It indicates that the e-beam lithography is a precise method under optimized conditions.

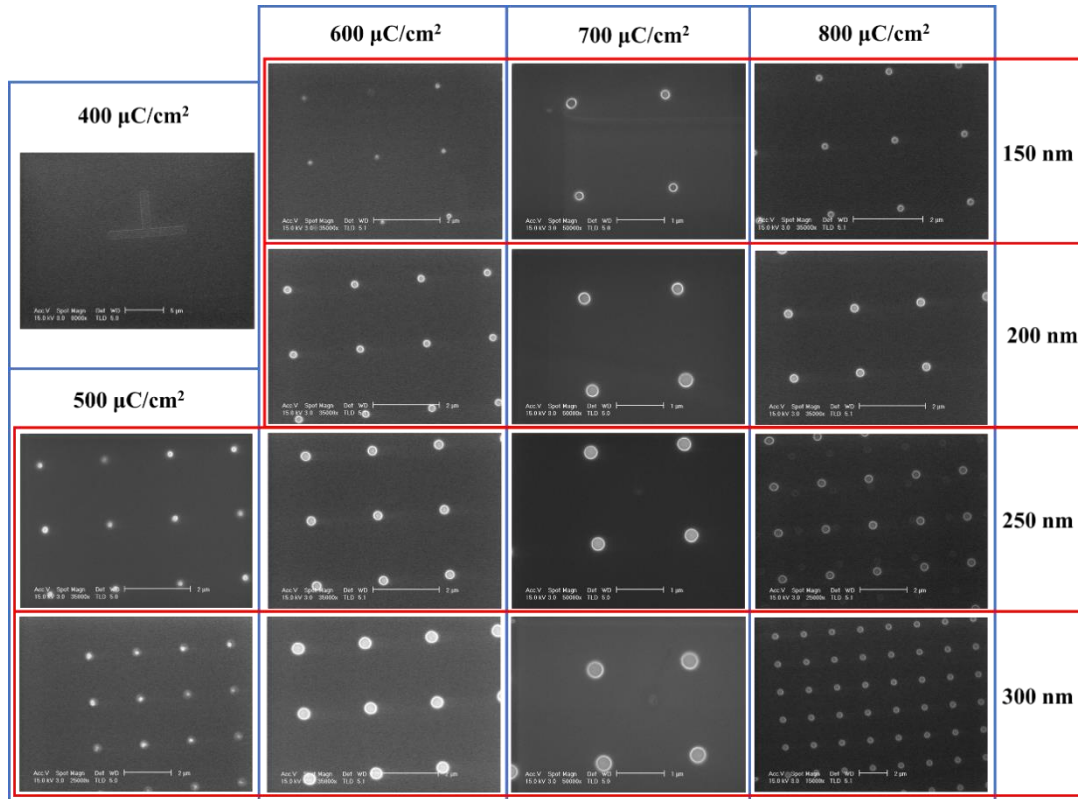


Figure 2-2 SEM images of nanohole arrays of different size under different doses.

Table 2-1 Quality of nanohole arrays with different sizes under different doses.

	400 $\mu\text{C}/\text{cm}^2$	500 $\mu\text{C}/\text{cm}^2$	600 $\mu\text{C}/\text{cm}^2$	700 $\mu\text{C}/\text{cm}^2$	800 $\mu\text{C}/\text{cm}^2$
150 nm	Nothing	Nothing	Bad	Good	Good
200 nm	Nothing	Nothing	Good	Good	Good
250 nm	Nothing	Bad	Good	Good	Good
300 nm	Nothing	Bad	Good	Good	Good

Table 2-2 Difference between the pre-set size and measured size of nanoholes under the dose of 700 $\mu\text{C}/\text{cm}^2$.

Dose = 700 $\mu\text{C}/\text{cm}^2$			
Pre-set hole size (nm)	Measured hole size by SEM (nm)	Deviation	Average
150	~154	2.7%	4.6%
200	~215	7.5%	
250	~264	5.6%	
300	~308	2.7%	

2.2.3 Comparison of circular and square nanoholes

Figure 2-3 shows circular and square nanoholes in PMMA films from 150 nm to 800 nm under the same dose of $700 \mu\text{C}/\text{cm}^2$. The nanoholes over 300 nm maintain a clear shape, while the square nanoholes under 200 nm gradually turn into circular nanoholes. Due to the writing mechanism of the e-beam writer, the circular nanoholes consume about twice of the time as the square nanoholes. Thus, if there is no requirement of the nanohole shape or the nanohole size is under 200 nm, making square nanoholes can save much more time than making circular nanoholes, which means saving much more money since the e-beam lithography is an expensive method.

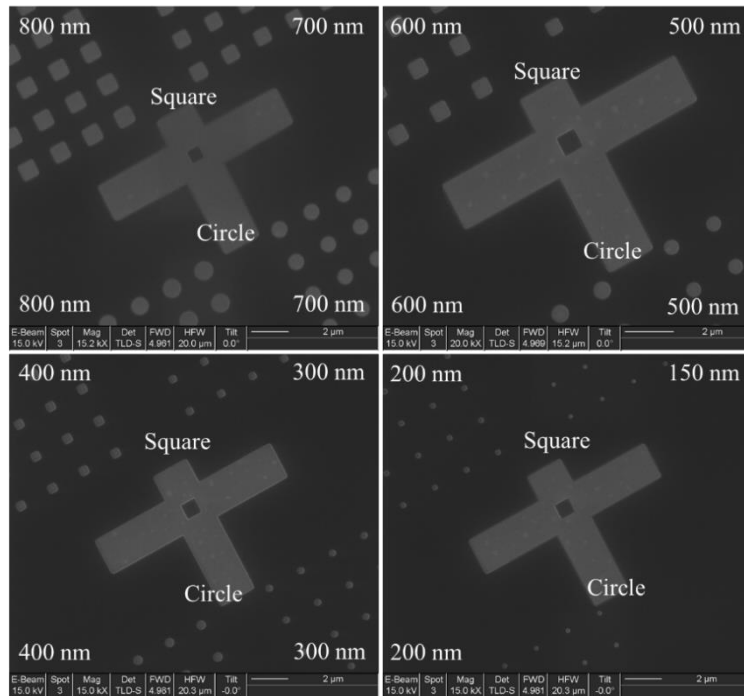


Figure 2-3 Circular and square nanoholes of different size under the same dose.

2.2.4 Comparison of wet etching and dry etching

Two different etching methods, wet etching and dry etching, are tried to etch the gold film with the PMMA mask. For the wet etching, the mixed KI/I₂ solution is used to etch gold. Figure 2-4 (a) shows the SEM images of the gold film after the wet etching and the PMMA removal by using KI/I₂ solution of high concentration (KI : I₂ : H₂O = 4 g : 1 g : 40 ml), while Figure 2-4 (b) by using KI/I₂ solution of low concentration (KI : I₂ : H₂O = 4 g : 1 g : 800 ml). The etching time of both conditions is 20 s. Figure 2-4 (a) shows an average size of about 1.7 μm and Figure 2-4 (b) shows a smaller size from 100 to 400 nm. Although the PMMA mask has circular nanoholes, both the etching shapes of the holes are irregular at the edge. Especially for the small size, the shapes of the nanoholes differ from one another and cannot be controlled due to the nonuniform chemical reaction rate in different directions. Thus, the wet etching method is not suitable for the fabrication of the nanopatterns.

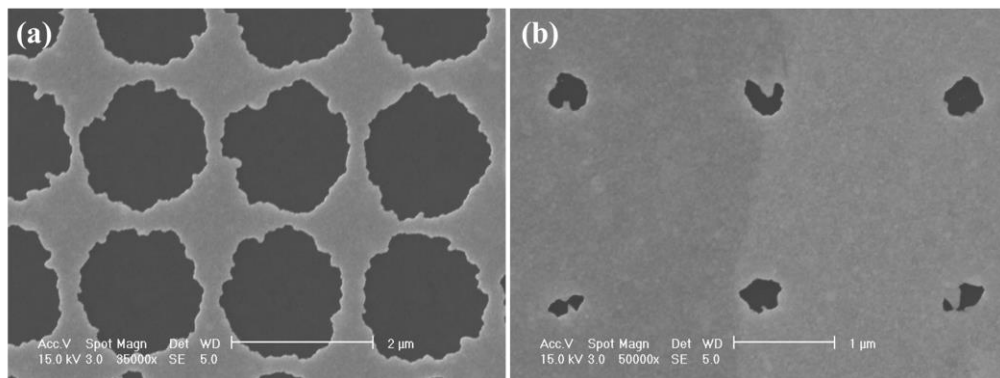


Figure 2-4 SEM images of wet etching of the gold with PMMA mask under the same etching time by using KI/I₂ solution of different concentrations.

For the dry etching, the ion mill equipment is used to etch the gold film under the PMMA mask. Ion milling is a physical etching technique whereby the ions of an inert gas (typically Ar) are accelerated from a wide beam ion source onto the surface of a substrate (or coated substrate) in the vacuum to remove material to some desired depth or underlayer. Figure 2-5 shows the SEM images of the nanohole arrays in the gold film after the ion milling and PMMA removal. Different sizes of circular and square nanoholes from 150 nm to 800 nm are obtained in the gold film. The uniformity and homogeneity of the size and the shape of the nanoholes have been perfectly inherited from the PMMA masks that are shown in Figure 2-3. To etch a 100 nm thick gold film, a typical etching time of 3 min is conducted.

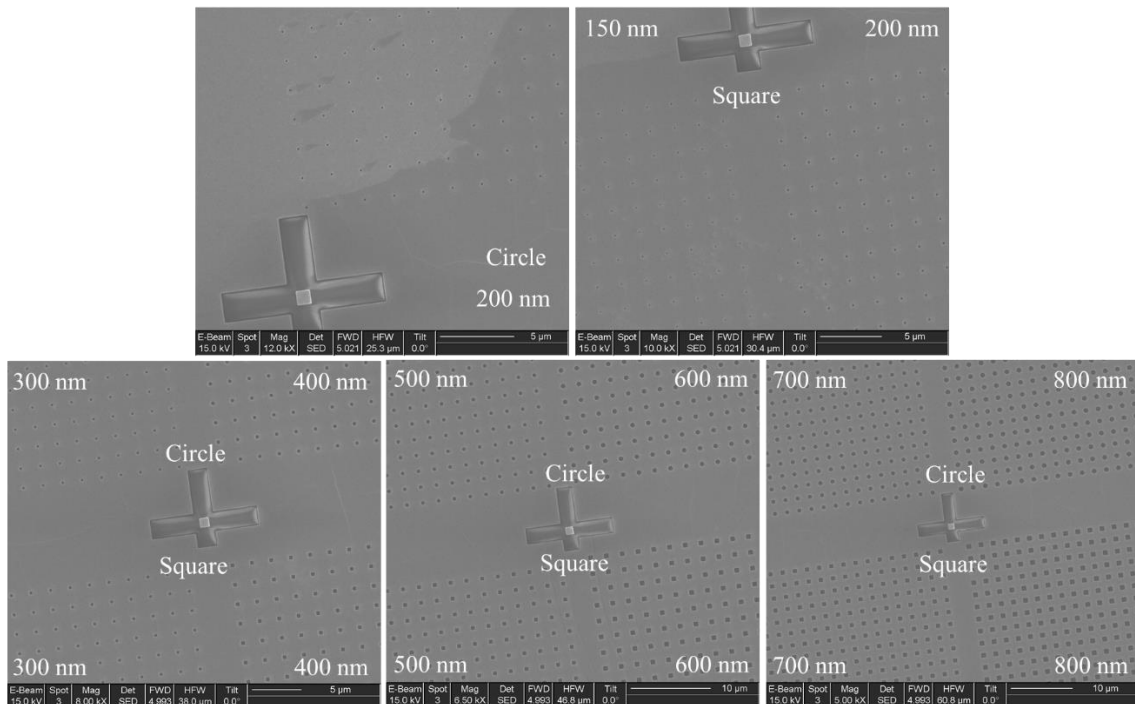


Figure 2-5 SEM images of gold films by dry etching with PMMA mask.

Table 2-3 Sizes of circular and square nanoholes measured from SEM images.

Preset size	Circle size	Square size
150	/	132
200	186	192
300	284	285
400	376	383
500	490	478
600	597	577
700	693	688
800	794	790

2.3 Nanoimprint Lithography

2.3.1 Fabrication process

Nanoimprint lithography has a few more steps since it includes a fabrication process of the mold. However, the mold can be used for many times to do the nanoimprint lithography. A typical fabrication process of the mold for nanoimprint is shown in Figure 2-8. A silicon substrate with a 300 nm thick SiO₂ layer is chosen to make the mold. First, a 350 nm thick PMMA layer is spin-coated on the Si/SiO₂ substrate. After baking the substrate for 2 min at 180 °C, the nanohole array pattern with the desired diameter and period is written on the PMMA by the e-beam writer. Second, the sample is developed by the mixture of the IPA and water solution with a ratio of 2 : 1 for 90 s and dried by nitrogen. Third, a chromium layer of 30 nm thickness is deposited on the sample by the e-beam evaporator. Next, the PMMA is removed by the hot acetone and the chromium nanodot array with the desired diameter and period will remain on the Si/SiO₂ substrate. Then, the substrate is etched by the reactive-ion etching with the C₄F₈ and O₂. Finally, after removing

the remaining chromium by a chromium etchant, an anti-stick layer is coated on the sample by the reactive-ion etching with the C_4F_8 .

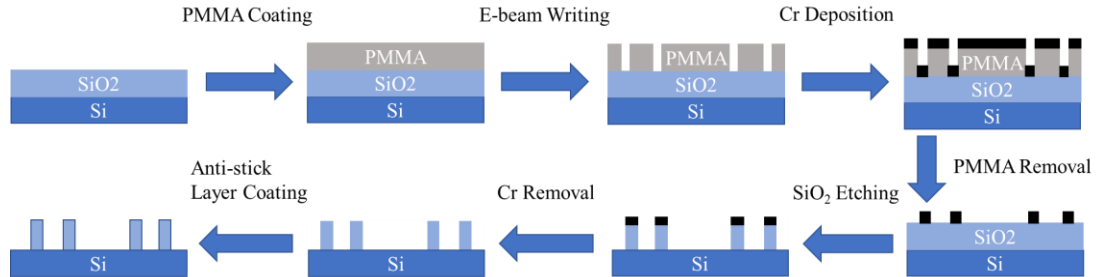


Figure 2-8 A typical fabrication process of the mold for nanoimprint.

After successfully making the mold, it can be used to do nanoimprint lithography. Figure 2-9 shows a typical fabrication process of the nanohole array in the gold thin film by nanoimprint lithography. First, a chromium layer of 5 nm thickness followed by a gold layer of 95 nm thickness is deposited on the glass substrate by the e-beam evaporator. Second, an mr-I 7030R thermoplastic resist of 300 nm thickness is spin-coated on the top of the gold layer at 3000 rpm. After baking the sample for 2 min at 140 °C, the sample is imprinted by the mold fabricated above at 135 °C under the pressure of 500 psi. Next, the sample is etched for 2 min by the reactive-ion etching with O_2 to remove the residual layer of the thermoplastic resist. Then, the sample is etched for 3 min by the ion mill to remove the gold and chromium. Finally, the 7030R resist layer is removed by the hot acetone under sonication.

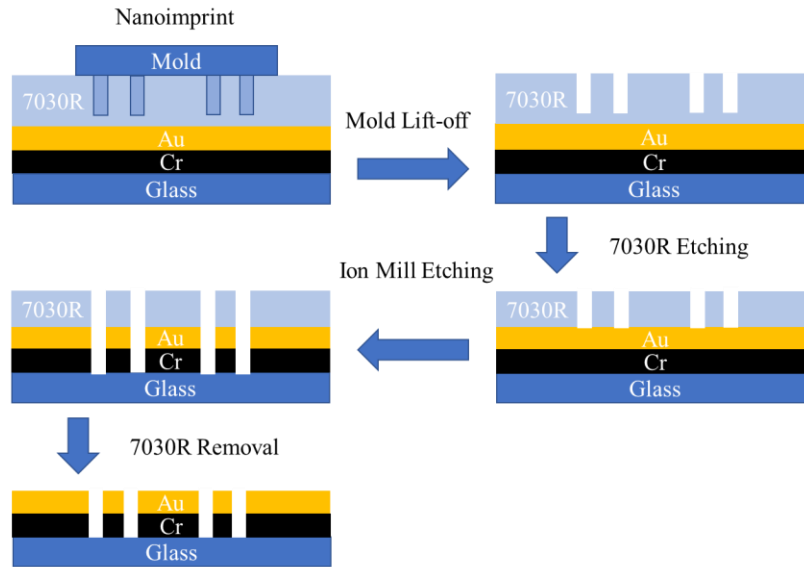


Figure 2-9 A typical fabrication process of the gold nanohole array thin film by nanoimprint lithography.

2.3.2 Etching rate of SiO₂ by C₄F₈ and O₂

For the process of mold fabrication, the SiO₂ can be etched by reactive-ion etching with C₄F₈ and O₂. Table 2-4 shows the experimental parameters used for the reactive-ion etching. The RF power is 70 W and the ICP power is 1500 W. The flow rate of the C₄F₈ to O₂ is 45 sccm to 5 sccm. The pressure and temperature is kept at 6 mTorr and 20 °C, respectively. And the pressure of the helium is kept at 10 Torr, which is used for cooling. This recipe is used to etch SiO₂ which has a chromium mask. It gives a reference etching rate of 377 : 6.9 nm/min for SiO₂ to chromium. To acquire the practical etching rate of our system, some tests are conducted. Several Si substrates with a 300 nm thick SiO₂ layer are etched by the reactive-ion etching using this recipe for different times. Table 2-5 concludes the data obtained from these samples. The samples have been etched for 35, 40, 45, 60 s

respectively. For each sample, half of the surface area is covered by the tape which prevented the SiO₂ from etching. Each sample has been measured three times at different positions by the profilometer. And then the average etching depth and the average etching rate of SiO₂ have been calculated and shown in Table 2-5. Sample 4 is excluded from calculating the average etching rate of SiO₂ because it is over-etched. The average etching rate of SiO₂ calculated is 382.2 nm/min, which is very close to the reference etching rate. According to this, about 47.1 s is needed to etch 300 nm thick SiO₂.

Table 2-4 Recipe of etching SiO₂ with chromium as a mask.

RF Power	[W]	70
ICP Power	[W]	1500
Pressure	[mTorr]	6
C ₄ F ₈	[sccm]	45
O ₂	[sccm]	5
Temperature	[°C]	20
Helium	[Torr]	10

Table 2-5 Etching depth of SiO₂ measured by the profilometer and average etching rate of SiO₂ by C₄F₈ and O₂.

Sample	Etch time (s)	Measured depth by Profilograph (nm)			Average (nm)	Rate (nm/min)	Average (nm/min)
1	35	240	220	235	232	398	382.2
2	40	255	260	260	257	385.5	
3	45	270	260	285	272	363	
4	60	330	325	340	332	332	/

2.3.3 Etching rate of SiO₂ by CHF₃ and O₂

The SiO₂ can also be etched by the reactive-ion etching with the CHF₃ and O₂. Table 2-6 shows the experimental parameters used for the reactive-ion etching. The RF power is 200 W and the ICP power is 0 W. The flow rate of the CHF₃ to O₂ is 50 sccm to 2 sccm.

The pressure and temperature is kept at 50 mTorr and 20 °C, respectively. And the pressure of the helium is kept at 10 Torr, which is used for cooling. This recipe is used to etch SiO₂ with PMMA as a mask, which gives a reference etching rate of 29 : 29 nm/min for SiO₂ to PMMA. To obtain the practical etching rate of our system, two Si substrates with a 300 nm thick SiO₂ layer are etched by the reactive-ion etching using this recipe for different times. The method to measure the etching depth is the same as the previous experiment. Table 2-7 shows the results of the two samples that are etched for 5 min and 10 min, respectively. The average etching rate calculated is about 31 nm/min, which is very close to the reference etching rate. Additionally, the PMMA mask can be etched at almost the same rate as the SiO₂ by this recipe. Thus, the thickness of the PMMA should be well controlled to avoid over-etching.

Table 2-6 Recipe of etching SiO₂ with PMMA as a mask.

RF Power	[W]	200
ICP Power	[W]	0
Pressure	[mTorr]	50
CHF ₃	[sccm]	50
O ₂	[sccm]	2
Temperature	[°C]	20
Helium	[Torr]	10

Table 2-7 Etching depth of SiO₂ measured by the profilometer and average etching rate of SiO₂ by CHF₃ and O₂.

Sample	Etch time (min)	SEM measured depth (nm)	Rate (nm/min)	Average (nm/min)
1	5	~156	31	31
2	10	~311	31	

2.3.4 Performance of the anti-stick layer

Table 2-8 shows the experimental parameters for the anti-stick layer coated on the Si/SiO₂ mold. The RF power is 50 W while the ICP power is not necessary. The flow rate of the C₄F₈ is kept at 100 sccm. And the system pressure and temperature are kept at 80 mTorr and 20 °C, respectively. The pressure of the helium is kept at 10 Torr and the processing time is set to 30 s.

After coating the anti-stick layer, the surface energy of the molds with and without the anti-stick layer has been compared qualitatively by water contact angle examination. Figure 2-10 (a) shows that the Si/SiO₂ surface with the anti-stick layer can have a contact angle of more than 90° between the surface and the water, which indicates a high hydrophobicity of the anti-stick layer. While Figure 2-10 (b) shows that the Si/SiO₂ surface without the anti-stick layer can only have a small contact angle between the surface and the water, which reflects a high hydrophilia of the Si/SiO₂ surface. Although no difference in the mold surface can be seen before and after the treatment by eyes, the contact angle test indicates that the anti-stick layer is successfully applied to the mold. With the existence of the anti-stick layer, the repeatability of the mold can be dramatically improved.

Table 2-8 Recipe of the anti-stick layer coating.

RF Power	[W]	50
ICP Power	[W]	0
Pressure	[mTorr]	80
C ₄ F ₈	[sccm]	100
Temperature	[°C]	20
Helium	[Torr]	10
Time	[s]	30

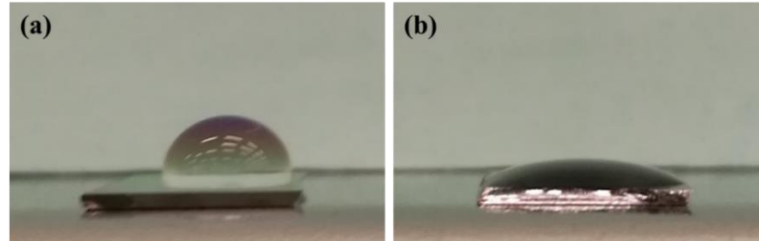


Figure 2-10 Surface energy difference of the Si/SiO₂ mold (a) with and (b) without the anti-stick layer.

2.3.5 Etching rate of the mr-I 7030R resist by O₂ plasma

To etch the mr-I 7030R resist by the reactive-ion etching, the O₂ plasma is used. Table 2-9 shows the experimental parameters in detail. Here, two different system pressures have been tested, 10 mTorr and 3.3 mTorr, while the other conditions are kept constant. The RF power is set to 70 W without the ICP power. The flow rate of O₂ is kept at 50 sccm. The system temperature is kept at 20 °C and the helium pressure is kept at 10 Torr. For each recipe, several samples are etched for 1, 2, 3, and 4 min, respectively. These samples are the Si/SiO₂ substrates coated with the mr-I 7030R resist of enough thickness. For each sample, half of the surface area is covered by the tape which prevents the resist from etching. The etching depth of the mr-I 7030R resist is measured by the profilometer and then the etching rate is calculated. Table 2-10 shows the calculated etching rate of each

sample for the two recipes and the average etching rates are also inferred. The final results give the average vertical etching rate of 52.6 nm/min for 10 mTorr and 33.8 nm/min for 3.3 mTorr. This indicates that a higher pressure leads to a higher etching efficiency.

Table 2-9 Recipe of etching mr-I 7030R resist by O₂ plasma.

RF Power	[W]	70
ICP Power	[W]	0
Pressure	[mTorr]	10 or 3.3
O ₂	[sccm]	50
Temperature	[°C]	20
Helium	[Torr]	10

Table 2-10 Vertical etching rate of the mr-I 7030R resist by different recipes.

Sample	Etching time (min)	Etching rate of different recipes (nm/min)	
		Pressure 10 mTorr	Pressure 3.3 mTorr
# 1	1	52	/
# 2	2	53.5	32
# 3	3	51.7	34.2
# 4	4	53.1	35.3
Average		52.6	33.8

To estimate the horizontal etching rate of the mr-I 7030R resist, three Si/SiO₂ substrates with the mr-I 7030R resist of 300 nm thickness are imprinted by the mold with nanohole arrays of 100 nm, 150 nm, and 200 nm in diameter that all have 500 nm period. Then the samples are etched for 3, 4, and 5 min respectively by the high-pressure O₂ plasma recipe shown above. Next, the samples are all etched by the CHF₃ and O₂ for 8 min. The practical diameters of the nanoholes are measured by the SEM images and compared with the preset values. Figure 2-11 shows the SEM images of nanoholes with different etching time and different sizes. Figure 2-11 (a), (b), and (c) show the nanohole arrays etched for 3 min. Figure 2-11 (d), (e), and (f) show the nanohole arrays etched for 4 min. And Figure

2-11 (g), (h), and (i) show the nanohole arrays etched for 5 min. The average etching rates of the nanoholes for different sizes and different etching times are calculated and displayed in Table 2-11. The final average value for the horizontal etching rate of the mr-I 7030R resist is about 15.3 nm/min at the high-pressure O₂ plasma. Considering that the samples have been treated by two etching steps, the practical horizontal etching rate of the mr-I 7030R resist only by the O₂ plasma should be much smaller than this value.

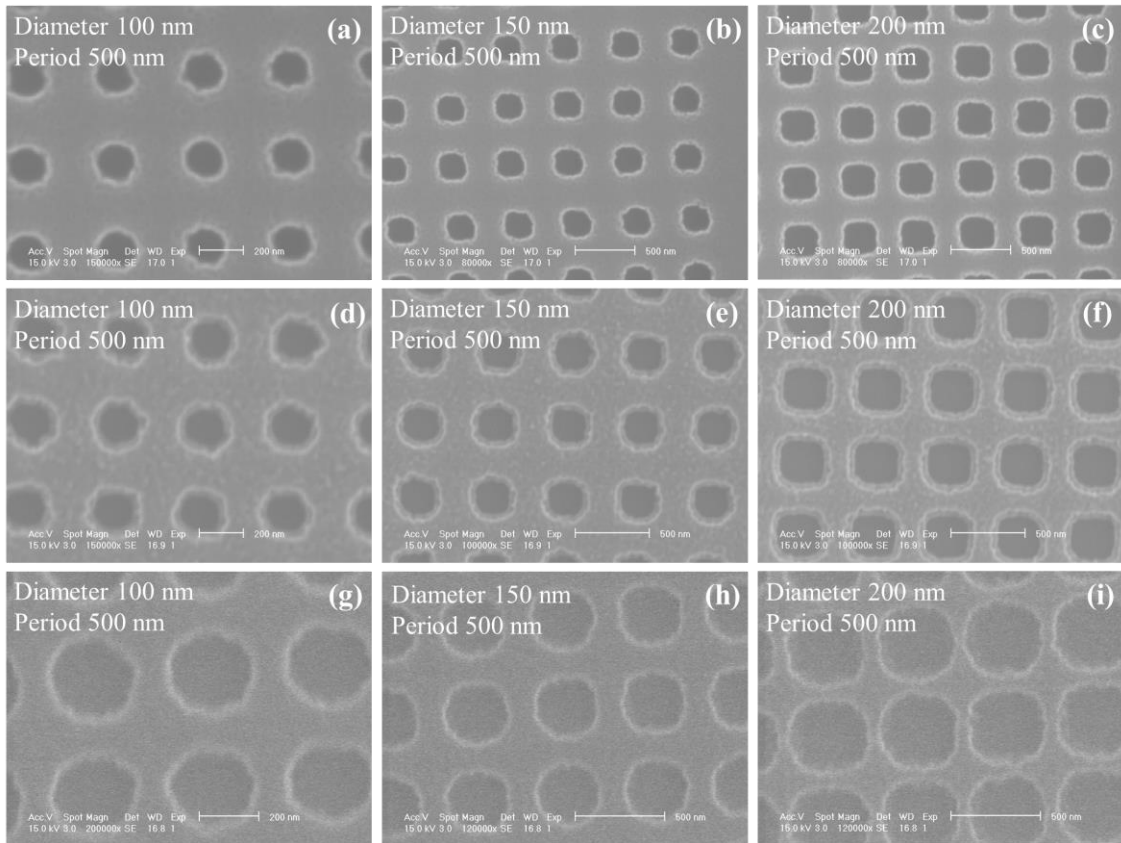


Figure 2-11 SEM images of nanohole arrays imprinted on the mr-I 7030R resist after etching of (a) (b) (c) 3 min, (d) (e) (f) 4 min, and (g) (h) (i) 5 min.

Table 2-11 Horizontal etching rate of the mr-I 7030R resist.

Substrate	Sample	Etching time by O ₂ at 10 mTorr (min)	Etching time by CHF ₃ and O ₂ (min)	100 nm nanohole etching rate (nm/min)	150 nm nanohole etching rate (nm/min)	200 nm nanohole etching rate (nm/min)	Average rate (nm/min)
SiO ₂ /Si	#1	3	8	12.5	11.6	13.3	15.3
	#2	4	8	14.7	15.4	16.7	
	#3	5	8	17.1	18.2	17.9	

2.3.6 Etching rate of the 495 PMMA by O₂ plasma

The etching rate of the 495 PMMA by the O₂ plasma is also studied. The experimental parameters are the same as those in Table 2-9 except that the system pressure is set to 3.3 mTorr. Several Si/SiO₂ substrates coated with the 495 PMMA of about 480 nm thickness have been etched with half of their surface area covered by the tape which prevents the PMMA from etching. These samples are etched for 3, 5, 6, and 7 min respectively and the etching depth is measured by the profilometer. Table 2-12 shows the calculated etching rate for each sample and the average etching rate by using the low-pressure recipe. Sample 4 may be over-etched and was not considered when calculating the average etching rate. Thus, the final vertical etching rate is about 69 nm/min.

Table 2-12 Vertical etching rate of the 495 PMMA by O₂ plasma.

Sample	Etch time (min)	Measured depth by Profilograph (nm)	Rate (nm/min)	Average rate (nm/min)
1	3	200	67	69
2	5	360	72	
3	6	415	69	
4	7 (PMMA all gone)	480 (thickness of PMMA at 1000 rpm)	69	

To measure the horizontal etching rate, several Si/SiO₂ substrates with the 495 PMMA of enough thickness are imprinted by the mold with nanohole arrays of 150 nm diameter and 200 nm diameter that both have 500 nm period. Then the samples are etched for 3, 5,

6, and 7 min respectively by the low-pressure O₂ plasma recipe shown above. The actual diameters of the nanoholes are measured by SEM before and after the etching. Figure 2-12 shows the top view SEM images of the nanohole arrays on the PMMA before and after etching. To achieve high quality SEM images, the samples are coated with a very thin gold layer to enhance the conductivity. Figure 2-12 (a) and (b) show the nanohole arrays before etching, (c) and (d) show the nanohole arrays etched for 3 min, (e) and (f) for 5 min, and (g) and (h) for 6 min. The samples etched for 7 min have no PMMA remaining at all. With the increasing etching time, the diameter of the nanoholes increases considerably. Figure 2-12 (a), (c), (e), and (g) show the diameter increasing trend of 150 nm nanohole arrays with 500 nm period, and Figure 2-12 (b), (d), (f), and (h) show the diameter increasing trend of 200 nm nanohole arrays with 500 nm period. The diameters of these nanoholes before and after etching are measured from the SEM images and shown in Table 2-13. The horizontal etching rate is then calculated by these data. The final average value for the horizontal etching rate is 14.9 nm/min at the low-pressure O₂ plasma. It is acceptable for microscale imprinting, while it is above average for the nanoimprint process, especially for the nanoholes of 150 nm diameter.

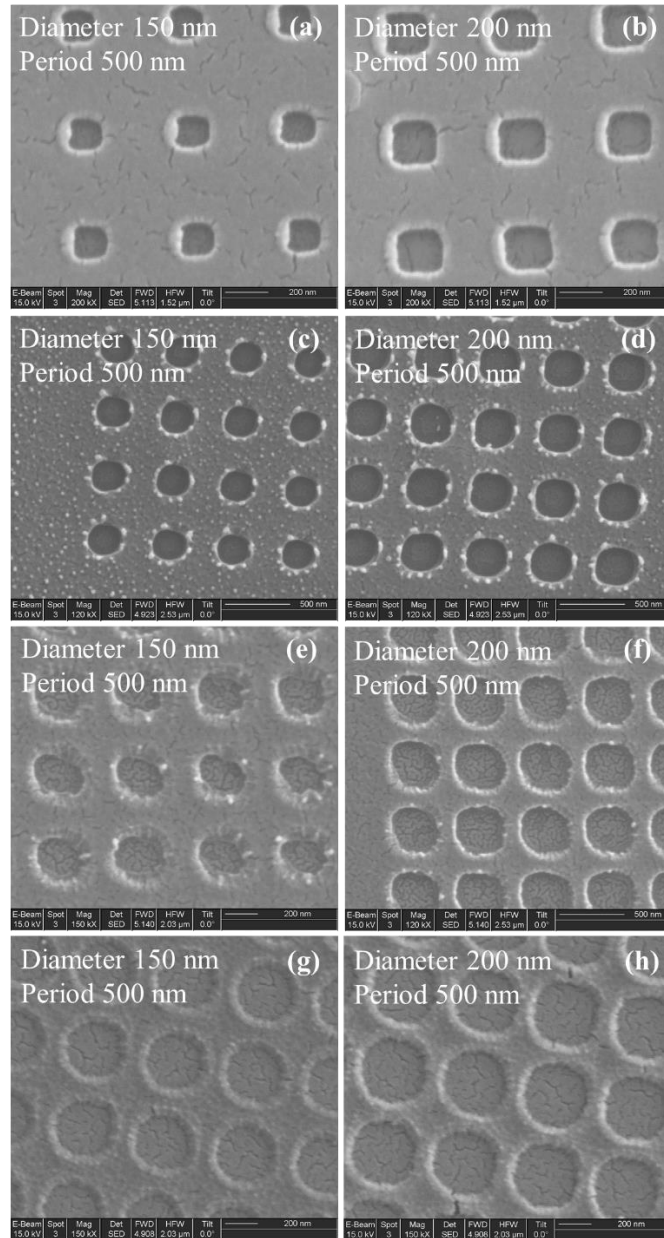


Figure 2-12 SEM images of nanohole arrays imprinted on PMMA (a) (b) before etching and after etching of (c) (d) 3 min, (e) (f) 5 min, and (g) (h) 6 min.

Table 2-13 Horizontal etching rate of the 495 PMMA by O₂ plasma.

Etching time (min)	3		5		6		7
Preset diameter of nanohole (nm)	150	200	150	200	150	200	PMMA is all etched away
Measured diameter before etching (nm)	~156	~210	~156	~210	~156	~210	
Measured diameter after etching (nm)	~253	~311	~280	~371	~324	~376	
Horizontal etching rate (nm/min)	16.2	16.8	12.4	16.1	14	13.8	
Average rate (nm/min)	14.9						

2.3.7 Comparison of 30 s mold and 50 s mold after nanoimprint

Here, the performance of the two Si/SiO₂ molds is compared, which are etched for 30 s and 50 s respectively by using the recipe shown in Table 2-4. Figure 2-13 (a), (b), (c), and (d) show the SEM images of the 30 s and Figure 2-13 (e), (f), (g), and (h) show the SEM images of the 50 s. Among them, (a), (b), (e), and (f) are top views of the molds, while (b), (c), (g), and (h) are 45° squint views of the molds. According to the etching rate of SiO₂, the height of the nanocylinders should be about 191 nm for 30 s. However, it is over-etched for the 50 s mold and the height of the nanocylinders for 50 s should be about 300 nm.

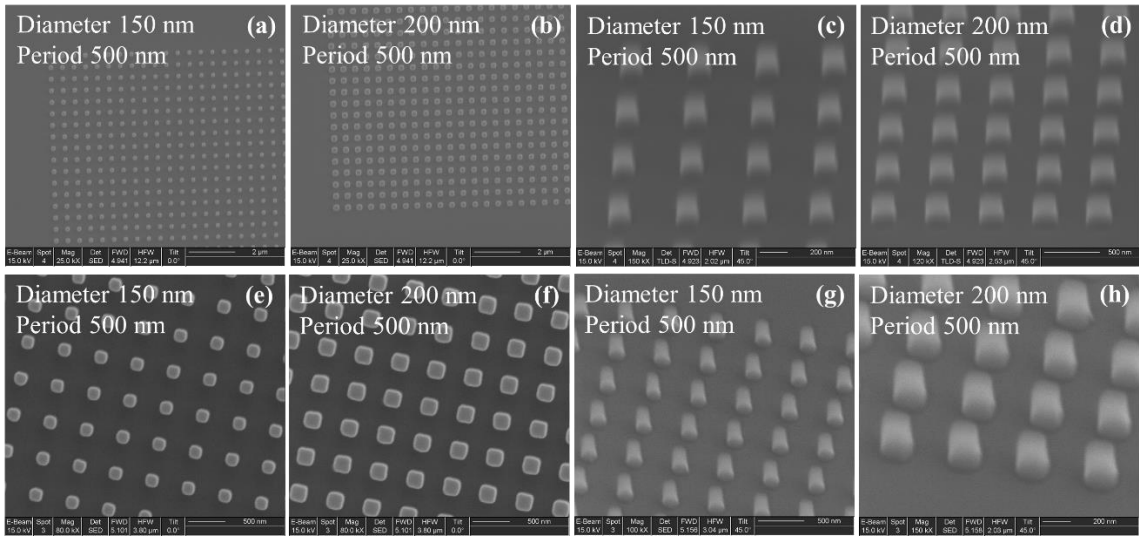


Figure 2-13 (a), (b), (c), and (d) are the SEM images of 30 s mold. (e), (f), (g), and (h) are the SEM images of 50 s mold.

After nanoimprint, the performance of the molds has a big difference. The nanocylinders of the 50 s mold are easily broken during the imprint process. Figure 2-14 shows a large area of the broken nanocylinders sticking into the PMMA after the lift-off of the mold. While the nanocylinders of the 30 s mold remain well after the nanoimprint. This

may be due to the weak connection between the Si and SiO₂. Figure 2-15 shows the schematic of the two molds. The SiO₂ nanocylinders of the 30 s mold still adjoin a 1/3 thick layer of SiO₂, which has a much larger area connected to the Si substrate than that of the 50 s mold. Because of the over-etching, the Si substrate has been exposed and the SiO₂ nanocylinders of the 50 s mold connect to the Si substrate directly and individually. Thus, the small connecting area between the Si substrate and the SiO₂ nanocylinders as well as the weaker connection between the Si substrate and the SiO₂ nanocylinders than that between the SiO₂ layer and the SiO₂ nanocylinders, leads to the broken nanocylinders after the nanoimprint. Thus, leaving a layer of SiO₂ and avoiding over-etching of SiO₂ can make the mold more durable and solid.

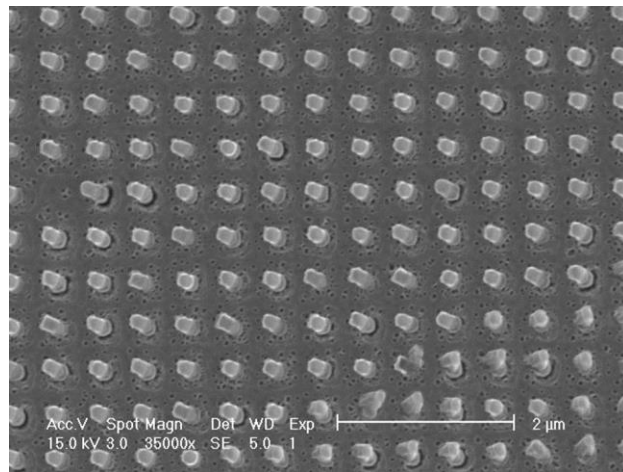


Figure 2-14 Performance of the 50 s mold imprinting on the PMMA.

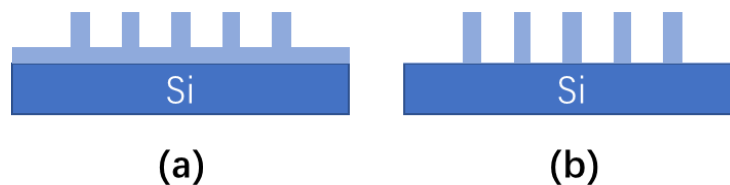


Figure 2-15 Schematic of the (a) 30 s mold and (b) 50 s mold.

2.4 Optimized Performance of Electron Beam Lithography and Nanoimprint Lithography

From the previous investigations on the e-beam lithography and nanoimprint lithography, the conditions of the nanohole array fabrication process are optimized. The nanohole arrays with 150 nm diameter and 2 μm period are fabricated by these two methods under the optimized conditions. Figure 2-16 shows the SEM images of the nanohole arrays with the desired configuration. Figure 2-16 (a) shows the nanohole arrays fabricated by e-beam lithography and Figure 2-16 (b) shows the nanohole arrays fabricated by nanoimprint lithography. Both the samples show extremely uniform nanohole arrays without any defects. The nanohole arrays fabricated by these two methods can have a high quality. These favorable results confirm the success of the previous studies and establish a solid base for the following experiments.

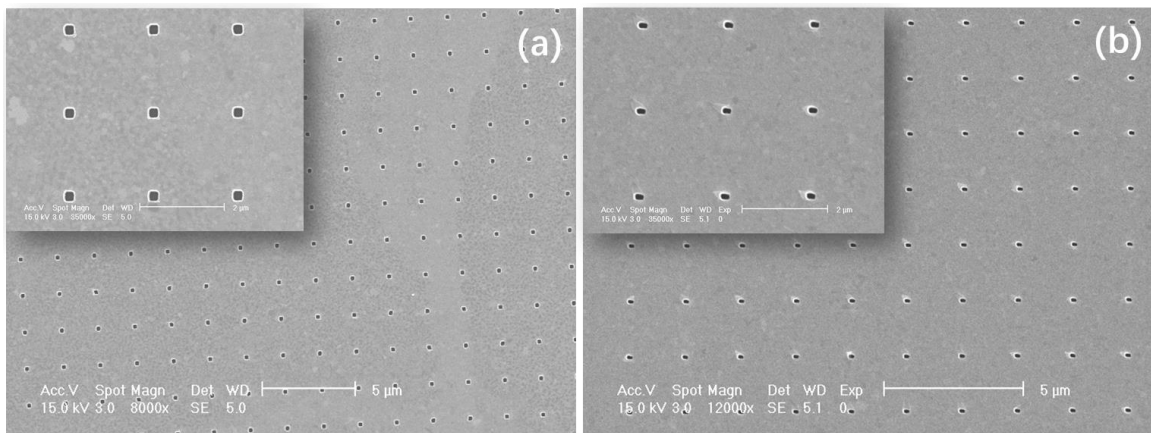


Figure 2-16 SEM images of nanohole arrays fabricated by (a) e-beam lithography and (b) nanoimprint lithography.

2.5 Conclusions

In this chapter, we have studied the fabrication conditions and ascertained the factors that will influence the quality and uniformity of the nanohole arrays. Two fabrication methods, e-beam lithography and nanoimprint lithography, are investigated and optimized to achieve the nanohole arrays with high quality and high uniformity in the gold thin film. For the e-beam lithography, the electron beam dose control for a given thickness of the resist is the most important. Since the e-beam writer is powerful and highly automatic equipment, the e-beam lithography has fewer steps than nanoimprint lithography. However, this is also why it is an expensive method. For nanoimprint lithography, it has many more factors to be concerned about than e-beam lithography. Due to many steps of etching including the etching of the molds and the samples, the process of the nanoimprint lithography for the nanoscale fabrication is much more complex than that of the e-beam lithography. The etching rates of the vertical direction and the horizontal direction of different materials are the most important things that need to be known in the nanoimprint process since the errors can be enlarged step by step if one of the steps is wrong. By comparing the performance of the mr-I 7030R resist and 495 PMMA, we finally decide to use the mr-I 7030R resist as the thermoplastic resist because it has a smaller horizontal etching rate and can be etched more uniformly than the 495 PMMA. Another thing to note is that the thermal expansion mismatch between the substrate and the mold with different materials more or less exists in the thermoplastic nanoimprint lithography. In our

experiments, when the mold and the substrate are both the Si/SiO₂, the shape of the patterns on the mold can be maintained well on the resist. While when we use glass as the substrate and the Si/SiO₂ as the mold, there will be subtle change in the shape of the patterns. To completely avoid this situation, UV nanoimprint lithography can be tried to solve this problem in the future.

Chapter 3 Imaging Analysis of the Nanohole Array by Darkfield Setup

3.1 Introduction

The darkfield imaging is a kind of technique usually used to detect very small samples or samples with low contrast, which can be invisible in the bright field imaging. Figure 3-1 shows the diagram of the illuminating light path through a standard darkfield microscope. Instead of the normal condenser in the bright field microscope, the darkfield microscope uses a darkfield condenser that contains an opaque aperture at the center. This opaque aperture blocks the center area of the illuminating light and makes an annular illuminating light. A microscope objective, whose numerical aperture is smaller than that of the annular illuminating light, is used to capture the scattering light from the specimen. No direct transmitted light can go into the microscope objective and only the scattering light can be detected. Thus, the background without any structure or any specimen will be almost purely dark. The specimen that is transparent or too small to be recognized in the bright field microscope can be observed clearly in the darkfield microscope.

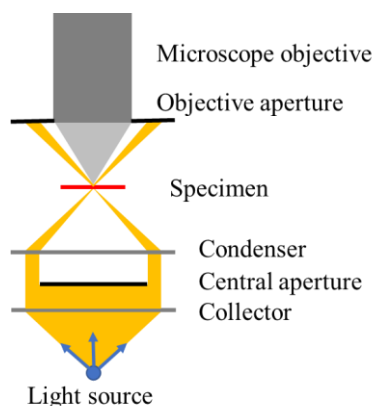


Figure 3-1 Diagram of the light path through a darkfield microscope.

In this chapter, to achieve a better contrast than the bright field setup, we have used the home-made darkfield imaging setups to investigate the gold nanohole array samples fabricated in the previous chapter. The imaging quality is optimized by choosing the appropriate configuration. The nanohole array samples have also been blocked by the silica-shelled nanospheres. The microscopic images and the spectra of the blocked and unblocked nanohole array samples have been studied by the darkfield imaging setup with the CCD and the spectrometer. The illuminating light with different wavelengths is applied to the system. And the smartphone camera is tried to be coupled with the home-made darkfield imaging setup as well. The ImageJ software has been used to analyze the darkfield images.

3.2 Results and Discussion

3.2.1 The home-made darkfield imaging setup

Figure 3-2 shows the schematic of the home-made darkfield microscopic imaging setup. The sample can be measured by the CCD or the spectrometer with or without the

moveable mirror, respectively. The exciting light illuminates from the glass side of the sample at a large angle, which is chosen to make sure that the directly transmitted light cannot go into the objective lens. The angle between the incident direction of the exciting light and the horizontal line is 28° . Thus, only the scattering light of the nanostructures can go into the objective lens and detected by the CCD and the spectrometer, which is so-called darkfield imaging. The absence or presence of the moveable mirror in the setup allows the measurement by the spectrometer or the CCD, respectively. The illuminating white light is incident from the gold film side of the sample to help the objective lens focus on the nanostructures and will be turned off when performing darkfield imaging. The CCD is a Nikon DXM1200F digital camera, the spectrometer is a HORIBA iHR 320 spectrometer, and the objective is an M Plan Apo 50X long working distance objective.

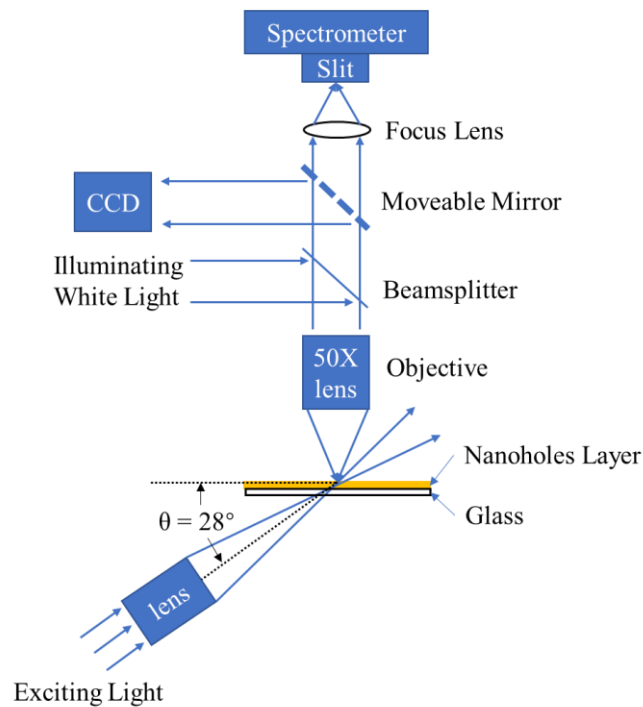


Figure 3-2 Schematic of home-made darkfield setup for nanohole array imaging.

3.2.2 Nanohole blocking experiment

The nanoparticles used to block the nanoholes were bought from the nanoComposix company. The nanoparticles are silica-shelled gold nanospheres with 70 nm core diameter and 20 nm shell thickness. The total diameter of the silica-shelled gold nanoparticles is 110 nm, which is a little smaller than the size of the nanoholes. The nanohole array on gold thin film used for the following experiment has a 150 nm diameter, 2 μm periodicity, and 100 nm thickness (5 nm Cr + 95 nm Au). The core-shell nanospheres are originally dispersed in the ethanol with a particle concentration of 2.9×10^{11} particles/mL. Before the nanohole blocking experiment, the nanosphere solution is diluted 20 times to have a particle concentration of about 10^{10} particles/mL. Photos of empty nanohole arrays are captured by the darkfield setup. When doing the nanohole blocking experiment, one drop of 10 μL diluted nanosphere solution is dropped onto the gold thin film with nanohole arrays by a pipette. After allowing the solution to air dry, the samples are again imaged by the CCD to find the nanoholes that are blocked by the nanospheres. The images taken after the blocking experiment are compared with those taken before the blocking experiment to locate the positions of the suspected blocked nanoholes. Then, the marked suspected blocked nanoholes are further confirmed by the SEM. Finally, the actual blocked nanoholes by a single nanosphere are marked and chosen to do the subsequent experiment.

Figure 3-3 shows the darkfield imaging of the gold nanohole array sample before and after the nanohole blocking experiment. Figure 3-3 (a) shows the empty nanohole array in

the gold thin film sample with a T shape marker on the right top side. The darkfield image has an extremely high contrast between the nanoholes and the background. The background, also the gold thin film, is completely dark. While the nanostructures in the gold thin film are bright and can be easily detected and distinguished by the detector. The darkfield image explicitly shows that the nanohole array has a good quality and uniform brightness, which can much benefit the subsequent experiments. Figure 3-3 (b) shows the same area of the sample after the nanohole blocking experiment. Some of the nanoholes have a more or less brown color, which means they have a high probability to be blocked by the nanospheres. The areas that contain the suspected blocked nanoholes are further confirmed by the SEM images of the same areas.

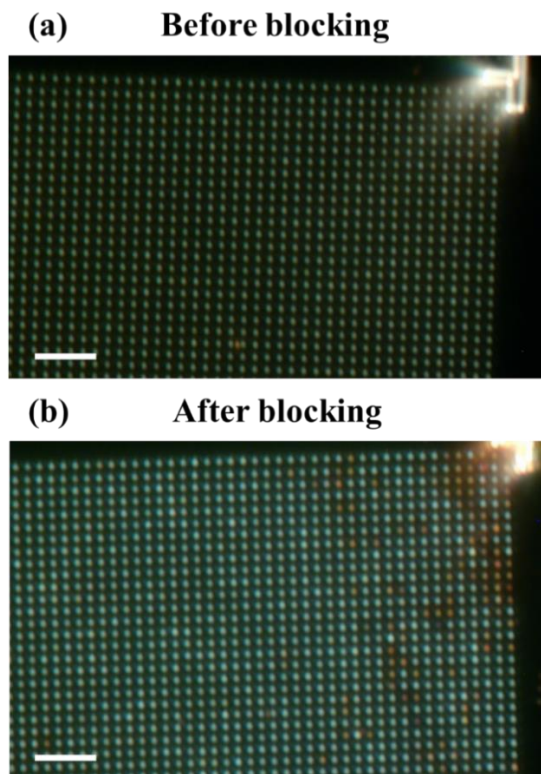


Figure 3-3 Darkfield images of the nanohole array (a) before blocking and (b) after blocking experiment. The scale bars are both 10 μm .

Figure 3-4 shows the corresponding SEM images of four typical areas circled by the red squares in the darkfield images. The suspected blocked nanoholes with color changes in the darkfield images are circled in the SEM images, which show that all the suspected nanoholes are blocked by a single nanosphere without exception. Since the core-shell gold nanospheres have a little smaller diameter than the nanoholes, there is a very high probability that the blocked nanoholes can only contain one single nanosphere. And these blocked nanoholes all have an obvious color change without exception, which can be a method to identify the blocked nanoholes in the darkfield images. While the color of empty nanoholes, with and without one or more nanospheres close around, remains unchanged. The SEM images also show that the size of the nanospheres vary in a large range, although the supplier claims an average core diameter of 70 nm and shell thickness of 20 nm. Some of the nanospheres are much smaller than the others. Furthermore, regardless of the different sizes of the nanospheres, the positions of the nanospheres inside the nanoholes are also different from one another since the total diameter of the nanospheres is always smaller than that of the nanoholes. Thus, the sizes of the nanospheres and the positions of the nanospheres inside the nanoholes should be the two main reasons that the blocked nanoholes have different degrees of color change compared with the empty nanoholes. While the nanospheres close around the nanoholes have negligible contributions to this color change.

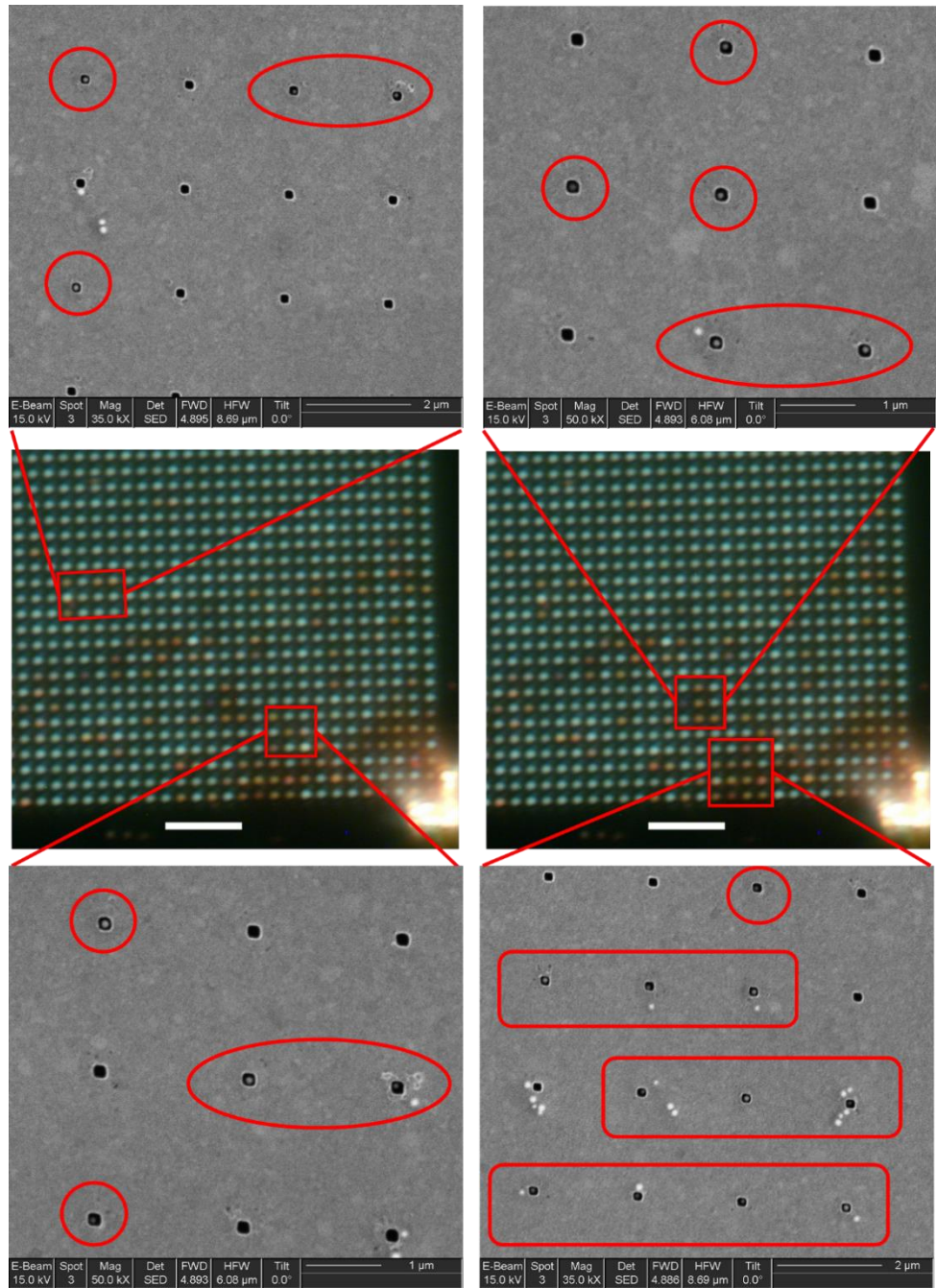


Figure 3-4 The corresponding areas of the SEM images and darkfield images. The circles in the SEM images show the nanoholes that are blocked by a single nanosphere. The scale bars are both 10 μm .

3.2.3 Color analysis

To analyze how the color of the blocked nanoholes changes, the RGB channels of two typical areas in the darkfield images are extracted by the ImageJ software, shown in Figure 3-5. In Figure 3-5 (a), the selected area contains 12 nanoholes, and the 3rd, 5th, 7th, 8th, 9th, 10th nanoholes from the left to right are blocked according to the color change. In Figure 3-5 (b), the selected area contains 11 nanoholes, and the 2nd, 5th, 7th, 8th, 10th nanoholes from the left to right are blocked according to the color change. The intensities of the red, green, and blue channels on the yellow line are separately displayed according to the pixel position of the yellow line. At the positions of the empty nanoholes, the corresponding intensities of the three channels remain at a similarly high level, respectively. However, at the positions of the blocked nanoholes, the corresponding intensities of the green and blue channels have a pronounced reduction, and the one of the red channel has no obvious reduction. The abnormality of the red channel precisely explains why the blocked nanoholes more or less tend to be brown. Another thing to be noted is that some of the blocked nanoholes seem to have a small enhancement for the red channel. On the other hand, the dramatic changes in the green and blue channels make it possible to use the monochromatic light as the exciting light source. This finding establishes a solid foundation for subsequent experiments.

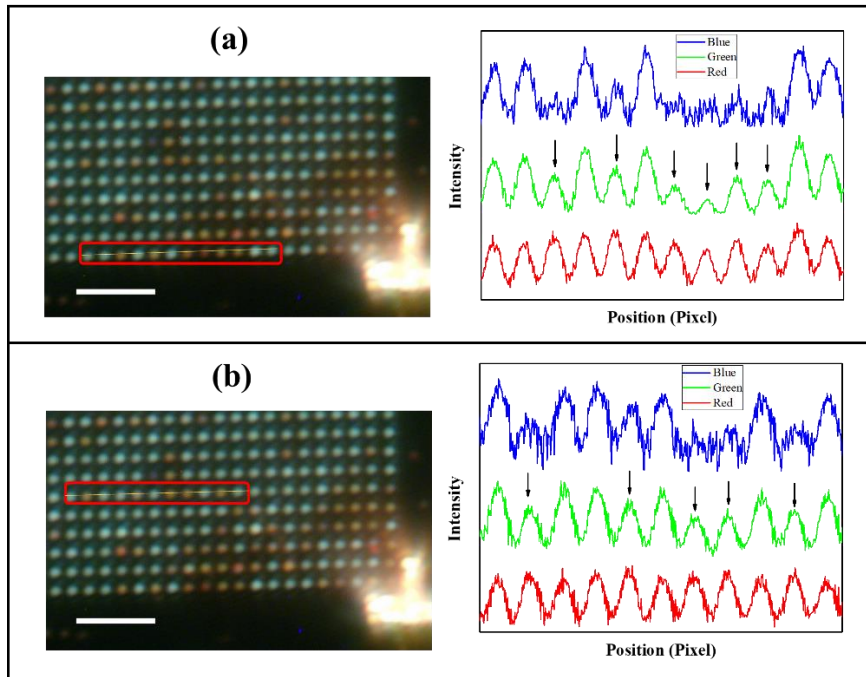


Figure 3-5 RGB channels of the selected areas in the darkfield images. (a) and (b) shows 12 and 11 nanoholes respectively, and their corresponding intensity on the yellow line. The scale bars are both 10 μm .

3.2.4 Spectra analysis

For further analysis, the darkfield scattering spectra of the blocked and unblocked nanoholes are measured by the home-made darkfield setup shown in Figure 3-2. Figure 3-6 (a) shows the positions of the several selected blocked and unblocked nanoholes circled by the red squares. There are in total 25 typical nanoholes including 16 unblocked nanoholes and 9 blocked nanoholes. The darkfield scattering spectra of these nanoholes are measured respectively. And the average darkfield scattering spectra of the blocked nanoholes and unblocked nanoholes are calculated and normalized by the exciting white light spectrum respectively, shown in Figure 3-6 (b). It indicates that there is a pronounced reduction of intensity below 600 nm wavelength when the nanoholes are blocked, while

above 600 nm wavelength there is a very small difference between the two spectra. More intuitively, the ratio between the two spectra of the blocked and unblocked nanoholes is calculated and displayed in Figure 3-6 (c). It indicates that there is a minimum at about 526 nm with a ratio of about 0.48, which means the light intensity around this wavelength can have a maximum reduction of about a half when the nanoholes are blocked by the core-shell gold nanospheres. The region with maximum reduction is corresponding to the green range. Additionally, The blue range, which is below 480 nm, has a nearly 40% reduction of intensity as well. While the red range above 620 nm shows a very small reduction. These results are in agreement with those of the color analysis. Although the color analysis seems to have a maximum reduction in the blue channel while the spectra analysis has a maximum reduction in the green range due to the different mechanisms of the two analysis method, they both show that the intensity change in the red channel is negligible.

On the other hand, the darkfield scattering spectrum of an individual unblocked nanohole has a resonance peak at about 510 nm, shown in Figure 3-6 (b). Although the darkfield scattering spectrum is very similar to the transmission spectrum of the gold film, shown in Figure 3-6 (d), which has a peak at about 500 nm, they are completely different. According to the previous studies of the individual nanohole shown in Figure 1-3 (b), a blueshift of the wavelength of the hole resonance is expected with increasing gold film thickness. Thus, the resonance peak of the darkfield scattering spectrum can be around 500 nm when the thickness of the gold film reaches 100 nm. Also, the transmission of the gold

film in darkfield setup is almost zero. As the consequence, the resonance peak of the darkfield scattering spectrum comes from the individual nanohole not the gold film.

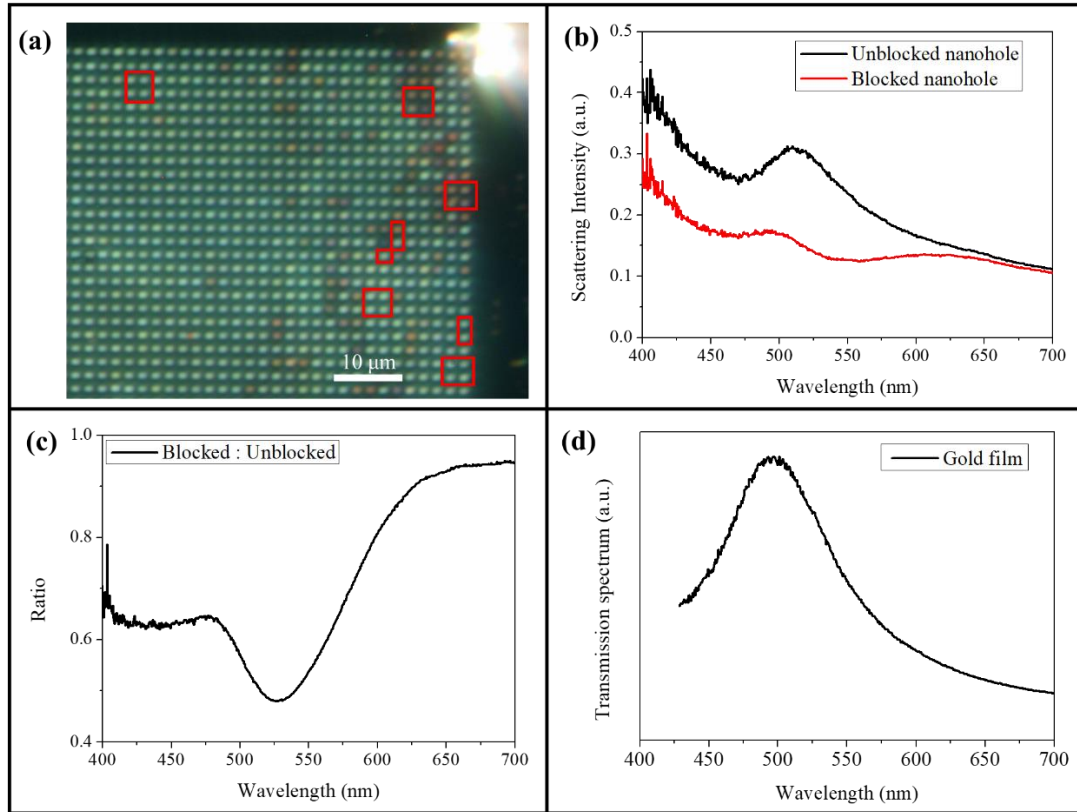


Figure 3-6 Spectra analysis of blocked and unblocked nanoholes. (a) Selected nanoholes. (b) Average spectra of blocked and unblocked nanoholes. (c) Intensity ratio according to (b). (d) Transmission spectra of gold film.

3.2.5 Analysis of monochromatic light obtained by filters

The color analysis and spectra analysis show that the monochromatic light has a great potential to have a better performance as the exciting light in the darkfield setup. Thus, the 450, 550, and 650 filters are utilized to obtain blue light, green light, and red light, respectively. Their transmission spectra are measured by the UV-vis spectrophotometer, shown in Figure 3-7. The center wavelengths for the blue filter, green filter, and red filter

are located at 455 nm, 550 nm, and 650 nm, respectively. The full width at the half maximum for all these filters is about 20 nm.

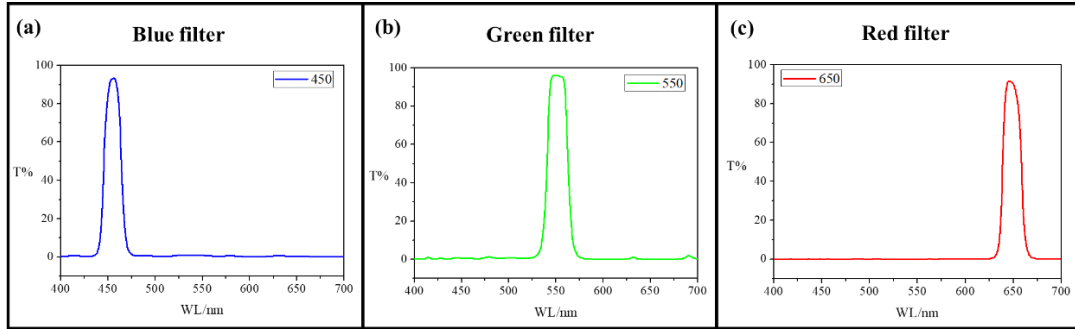


Figure 3-7 Transmission spectra of the (a) 450, (b) 550 and (c) 650 filters.

To investigate the performance of the blue, green, and red monochromatic light as the exciting light, a professional microscope with the darkfield condenser is used to analyze the nanohole array samples with blocked nanoholes. The measuring setup is shown in Figure 3-8. The CCD is the AmScope MU1000 digital camera, and the microscope is the Olympus BH-2 microscope. The darkfield condenser attached to the microscope can generate an annular light with a numerical aperture of about 0.9. To better fit the darkfield condenser, the 20X objective lens with a numerical aperture of about 0.46 is selected. The white balance of the CCD is set as default. The darkfield images of the same area of the blocked nanohole array sample, with the white light, blue light, green light, and red light as the exciting light, are shown in Figure 3-9 (a), (b), (c) and (d), respectively. These darkfield images show a high quality of definition and contrast. For the images excited by the white light, the unblocked nanoholes show a yellow color due to the halogen light source and a default white balance setting, while the blocked nanoholes clearly show a

different color which tends to be red or brown. For the images excited by the blue and green light, the blocked nanoholes show an obvious lower intensity than the unblocked nanoholes. However, for the images excited by the red light, the blocked and unblocked nanoholes can't be distinguished by the intensity. These results indicate that the blue light and green light can be good candidates of a monochromatic light source for the darkfield imaging, but the red light can't. They again agree with the results of the color analysis and spectra analysis. And since the human eyes are most sensitive to green light, Figure 3-9 (c) looks better than Figure 3-9 (b).

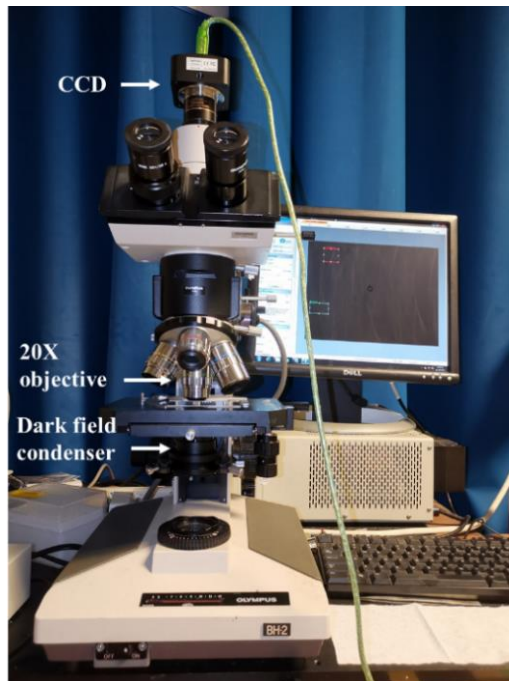


Figure 3-8 Professional microscope with darkfield condenser.

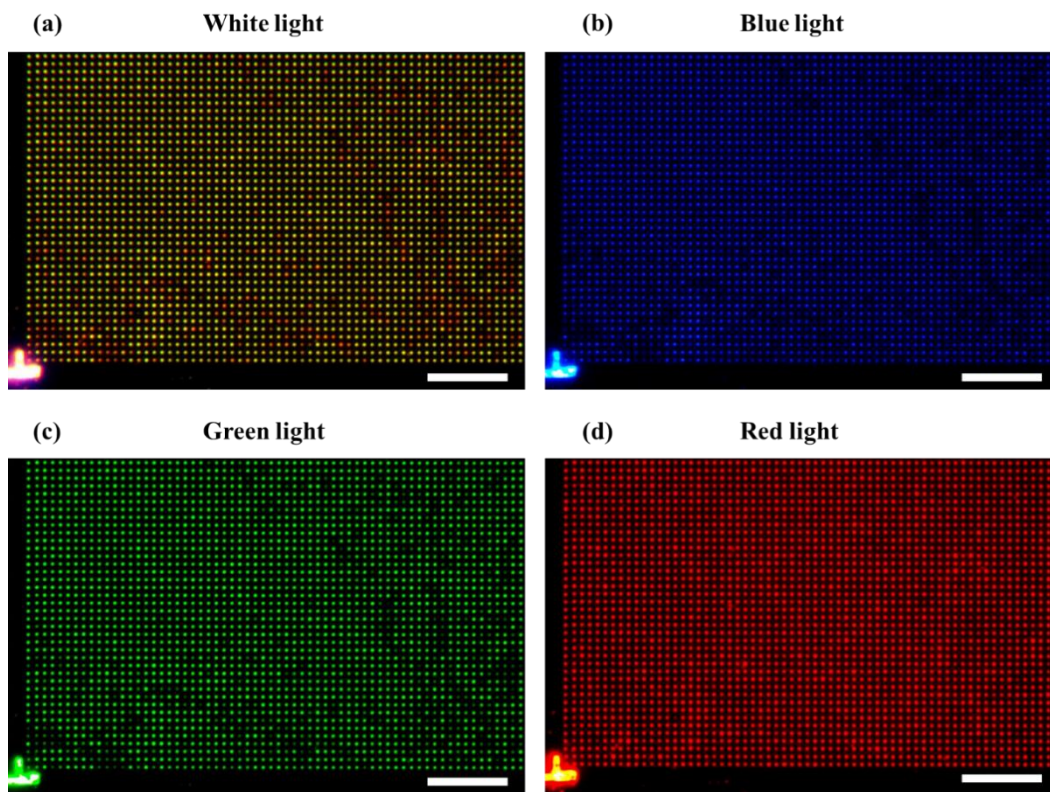


Figure 3-9 The darkfield images of the blocked nanohole array at the same area captured by the professional microscope (a) without filter, with (b) blue filter, (c) green filter, and (d) red filter. The scale bars are all 20 μm .

3.2.6 Inexpensive darkfield device coupled with a smartphone

Considering the on-site POC diagnostic, a portable and inexpensive imaging device, that can be coupled with the smartphone, is indispensable. To achieve this kind of device, finding a suitable microscope, which can be coupled with a smartphone to have enough magnification and resolution for detecting the nanoscale samples, is essential. Here, three inexpensive smartphone microscopes purchased from Amazon are tested to see if they can distinguish the nanoholes with only 2 μm periodicity. Figure 3-10 shows the three types of smartphone microscopes. The smartphone microscope shown in Figure 3-10 (a) contains a

highly compact lens group and costs about \$65. The one shown in Figure 3-10 (b) has the largest volume among the three and costs about \$10. The one shown in Figure 3-10 (c) is the smallest and has the simplest structure among the three, and also costs about \$10.

These smartphone microscopes are tested by the setup shown in Figure 3-11. The microscope to be tested is attached to the smartphone's camera. Then the smartphone is placed on the translation stage with its camera facing down. The smartphone and the microscope are adjusted by the stage while the sample is immobile on the sample holder. A simple darkfield environment is established by a LED light incident at a certain angle from the backside of the sample.



Figure 3-10 Three types of smartphone microscopes.

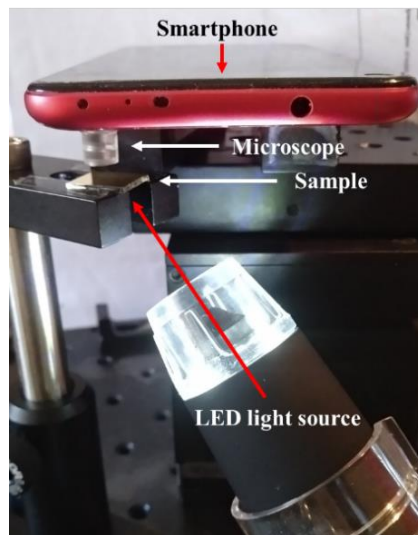


Figure 3-11 The simple darkfield setup for smartphone microscope testing.

The smartphone always uses the 2X optical magnification during all the tests while the three microscopes use their maximum optical magnification respectively. A control group using the professional microscope with the 10X eyepieces and 50X objective is also conducted. Their pixel resolutions are defined by micrometers per pixel and magnifications are calculated according to the control group and displayed in Table 3-1. The #1, #2, and #3 microscopes have a magnification of about 60X, 15X and 55X, respectively, and a pixel resolution of about 0.636 $\mu\text{m}/\text{px}$, 2.565 $\mu\text{m}/\text{px}$, and 0.700 $\mu\text{m}/\text{px}$, respectively. Figure 3-12 shows the images that are taken by the smartphone with #1 microscope, #3 microscope, and the professional microscope. The first row in Figure 3-12 (a) and (b) contains nanohole arrays with 2 μm periodicity and different diameters. Figure 3-12 (c) shows that the nanohole array with 150 nm diameter and 2 μm periodicity can be distinguished easily due to the large numerical aperture of the 50X objective and the high pixel resolution, 77 nm/px, of the professional microscope with a large magnification of 500X. However, Figure 3-12 (a) and (b) show that the #1 and #3 microscopes can't distinguish the nanohole array with the same periodicity due to a small magnification. These results show that even the most expensive one among the three with the largest magnification of 60X among the three cannot have enough resolution to distinguish the nanoholes with the 2 μm periodicity.

Table 3-1 Smartphone microscopes compared with the professional microscope.

Microscope	Magnification (whole system)	Pixel Resolution	Magnification (microscope)
#1 	Smartphone 2X Microscope max	0.636 $\mu\text{m}/\text{px}$	60X
#2 	Smartphone 2X Microscope max	2.565 $\mu\text{m}/\text{px}$	15X
#3 	Smartphone 2X Microscope max	0.700 $\mu\text{m}/\text{px}$	55X
	Smartphone 2X Eyepieces 10X Objective 50X	77 nm/px	500X

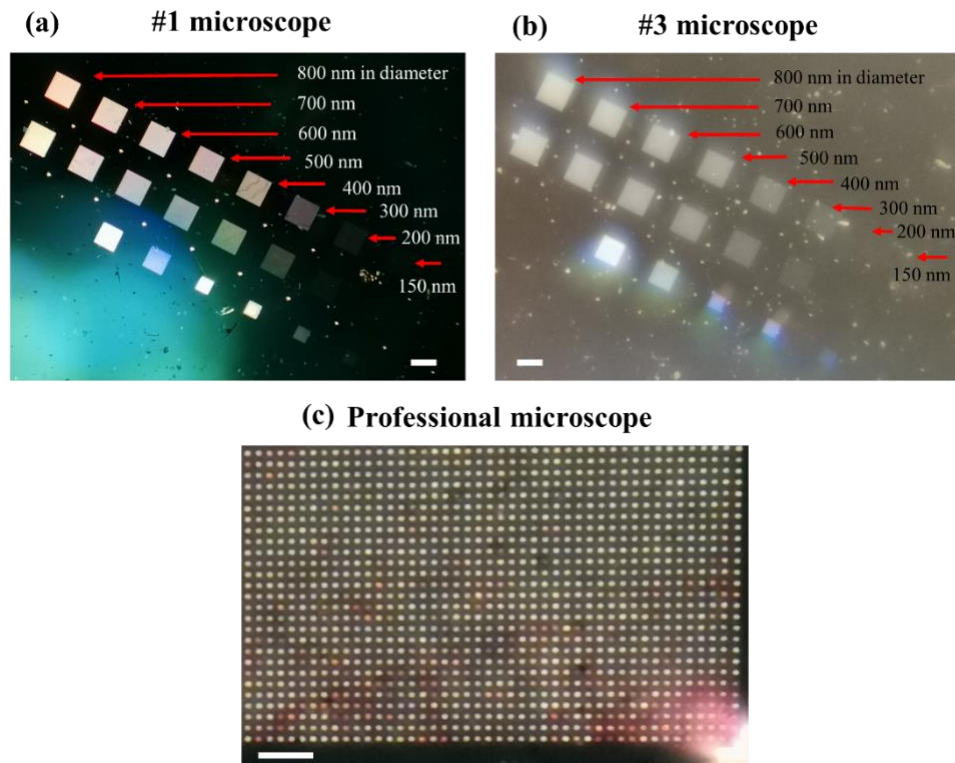


Figure 3-12 Images taken by the smartphone camera with different microscopes, (a) #1 microscope, (b) #3 microscope, and (c) professional microscope. The scale bars are 100 μm in (a) and (b), and 10 μm in (c).

In Figure 3-12 (c), a 2 μm length under 500X magnification can include about 26 pixels and one nanohole spot can include about 10 pixels in diameter. To have enough pixels for

one nanohole spot and the space between two nanoholes, it is conservatively estimated that at least a magnification of 200X is necessary for a smartphone, let alone the numerical aperture. Thus, an inexpensive learner's microscope purchased from Amazon costing about \$70 is tested, which has two types of eyepieces, 10X and 25X, and three types of objectives, 4X, 10X, and 40X. This microscope can achieve enough magnification but the volume of the device will increase. Firstly, the practical performance of the inexpensive microscope, such as the pixel resolution, field of view, and practical magnification, is investigated by using a ruler with 100 μm markers. Different combinations of the eyepieces and objectives are tested and the results are summarized in Table 3-2. Considering the field of view and practical magnification, the combination of 10X eyepiece and 40X objective is the best choice. The 40X objective can provide the highest optical resolution due to the largest numerical aperture among the three objectives under the same magnification. While the 10X eyepiece has a larger field of view than the 25X eyepiece. And they together provide about 363X magnification. Then, the inexpensive microscope is adapted to a home-made darkfield setup, shown in Figure 3-13. The exciting light is incident from the backside of the sample at a large angle. A filter can be put in front of the exciting light. The sample holder is replaced by a glass holder with a 3D translation stage. The eyepiece is also coupled with a smartphone holder. Next, this setup is used to test the performance of the inexpensive microscope configuration by taking pictures of the nanohole array sample with 150 nm diameter and 2 μm periodicity. The darkfield images taken by the smartphone with the professional microscope and the inexpensive microscope are compared and shown in

Figure 3-14 (a) and (b), respectively. It can be seen that the image quality of the inexpensive microscope at the center area is approaching that of the professional microscope. The inexpensive microscope can have enough magnification and optical resolution to distinguish the nanoholes. However, due to the lower quality lenses in the objective, the aberration is pronounced at the edge of the image taken by the inexpensive microscope. And the contrast of Figure 3-14 (b) between the background and the nanoscale structure is slightly inferior compared with that of Figure 3-14 (a). To sum up, the practical performance of the inexpensive microscope is acceptable to a certain degree for analyzing the nanohole array samples.

Table 3-2 Practical performance of the inexpensive microscope with different combinations of eyepieces and objectives.

Smartphone magnification	Eyepieces	Objective	Preset microscope magnification	Pixel resolution (um/px)	Field of view (um)	Practical microscope magnification
2X	10X	4X	40X	1.056	4000	36.5X
		10X	100X	0.406	1600	94.8X
		40X	400X	0.106	400	363X
	25X	4X	100X	0.407	950	94.7X
		10X	250X	0.165	360	234X
		40X	1000X	0.059	124	653X

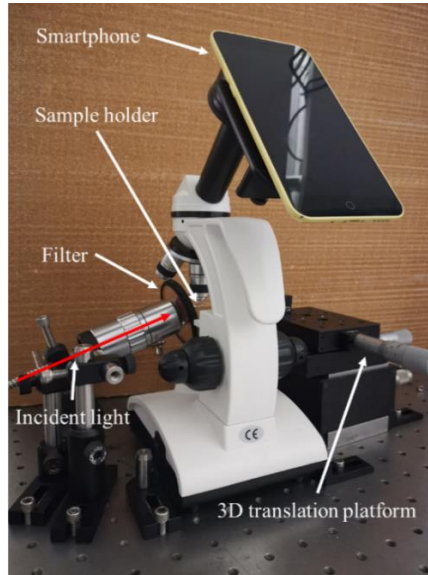
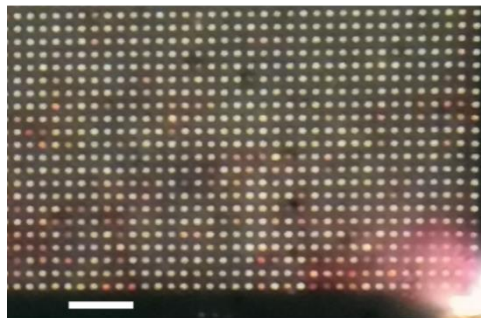


Figure 3-13 The home-made darkfield setup by using an inexpensive learner's microscope bundled with a smartphone holder. The eyepiece and the objective are 10X and 40X respectively.

(a) Professional microscope



(b) Inexpensive microscope

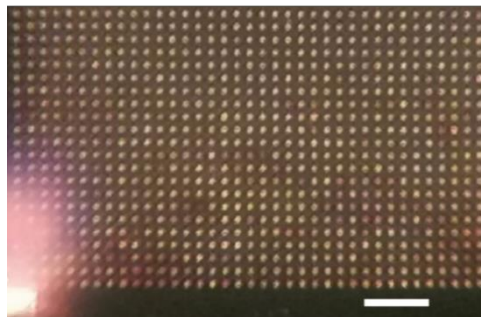


Figure 3-14 Darkfield images of the nanohole array captured by smartphone with (a) professional and (b) inexpensive microscope. The nanohole array has 150 nm diameter and 2 μm period. The scale bars are both 10 μm .

3.2.7 Filter test with inexpensive microscope darkfield setup

The RGB filters are also used to investigate the performance of the monochromatic light in the inexpensive microscope darkfield setup. The darkfield images with white light, blue light, green light, and red light are captured by the smartphone and shown in Figure 3-15. The image with the white light shows a nanohole array of uniform intensity, as well as the image with the green light. And the image with red light is slightly inferior compared with them. Unfortunately, the image with blue light has a very low definition and is extremely dim. Although we don't know how this happens in details, it should have some relation to the Bayer filter included in the CMOS of the smartphone camera, shown in Figure 3-16. The color filter array covers the pixel array of the CMOS. Each pixel sensor can only receive one of the RGB lights and record its intensity. That's why the sensor can recognize the color of the object. The RGB filters are arranged alternatively. Since the human eyes are most sensitive to green light, the Bayer filter array contains 50% green filters, 25% blue filters and 25% red filters. Thus, when using monochromatic light, the pixel resolution has been reduced because fewer pixel sensors can receive light. However, the pixel sensors with green filters endure less influence since they occupy half of the sensor array. This is why the green light has the best performance when using monochromatic light as the exciting light.

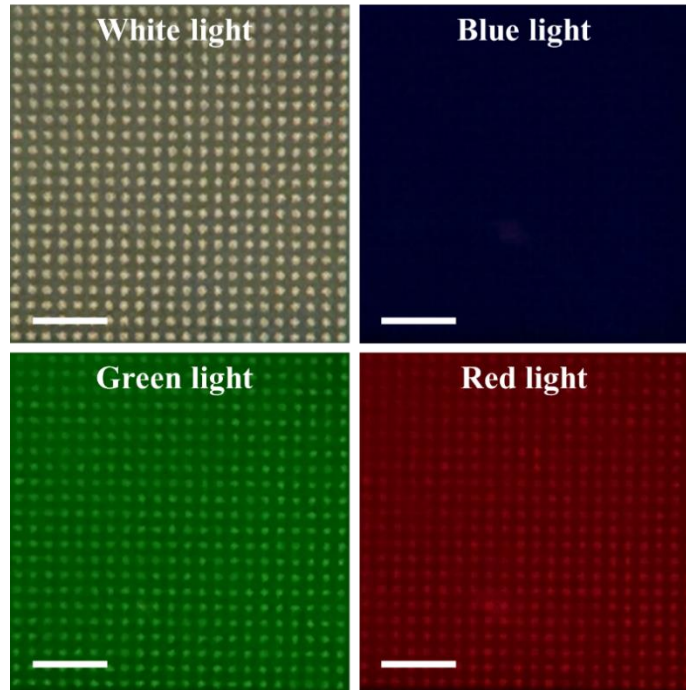


Figure 3-15 Darkfield images of the empty nanohole array, taken by a smartphone with RGB filters. The nanohole array has 150 nm diameter and 2 μm period. The scale bars are all 10 μm .

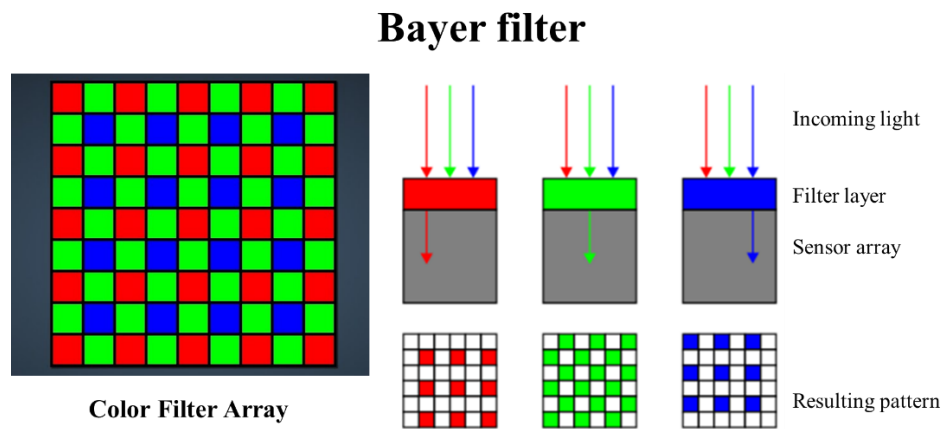


Figure 3-16 The Bayer filter in the CMOS of the smartphone camera.

As we know from the previous study, the red light cannot distinguish the blocked and unblocked nanoholes. And we also lose the choice of the blue light due to its awful performance in our setup. Thus, the green light is tested for the blocked nanohole array

sample and compared with the white light when as the exciting light. The darkfield images of the blocked nanohole array sample at the same area are captured by the smartphone with white light and green light, shown in Figure 3-17. The blocked and unblocked nanoholes cannot be distinguished well by eyes in the image with white light since the incident angle of the exciting light cannot perfectly match the numerical aperture of the cheap objective in the home-made inexpensive darkfield setup. However, the image with green light shows a better consequence. The blocked nanoholes can be distinguished from the unblocked ones since they have an obvious reduction of light intensity. Another thing to note is that the nonuniformity of the empty nanoholes is more enhanced when using monochromatic light. Thus, to fabricate more uniform nanohole arrays is very important to improve the imaging results.

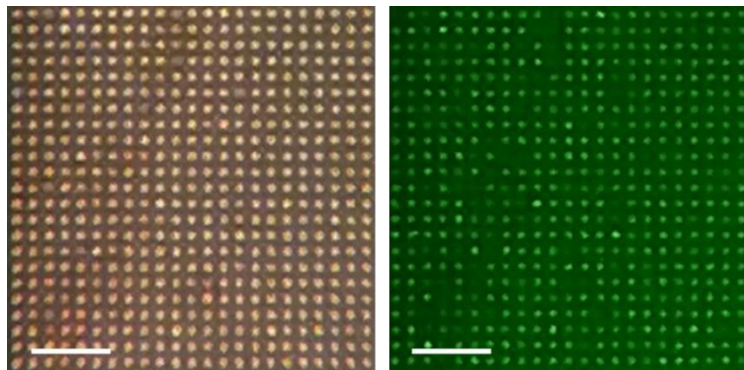


Figure 3-17 Darkfield images of the blocked nanohole array at the same area, taken by a smartphone. The nanohole array has 150 nm diameter and 2 μm period. The scale bars are both 10 μm .

3.2.8 Optimized field of view and designed structure of the device

By optimizing all the conditions that we can control, such as the monochromatic light source, the magnification of the eyepiece and objective, the field of view, and so on, a

nanohole array as large as 80×80 can be explicitly imaged by the inexpensive darkfield microscope setup coupled with a smartphone, which is shown in Figure 3-18. The nanohole array has a configuration of the 150 nm diameter and 2 μm periodicity. Some of the nanoholes that are blocked by the nanospheres have a lower intensity than those that are not blocked. This means that 6400 individual nanoholes can be detected at the same time within one image. If the quality of the cheap eyepiece and objective can be improved, a larger area of no aberration can be achieved, which means that more nanoholes, maybe more than 10000 nanoholes, can be detected at the same time. For the 10X eyepiece and 40X objective we have chosen, the field of view is about 400 μm in diameter. If there is no aberration, theoretically about 30000 nanoholes can be detected at the same time within one image for a nanohole array of the 150 nm diameter and 2 μm periodicity.

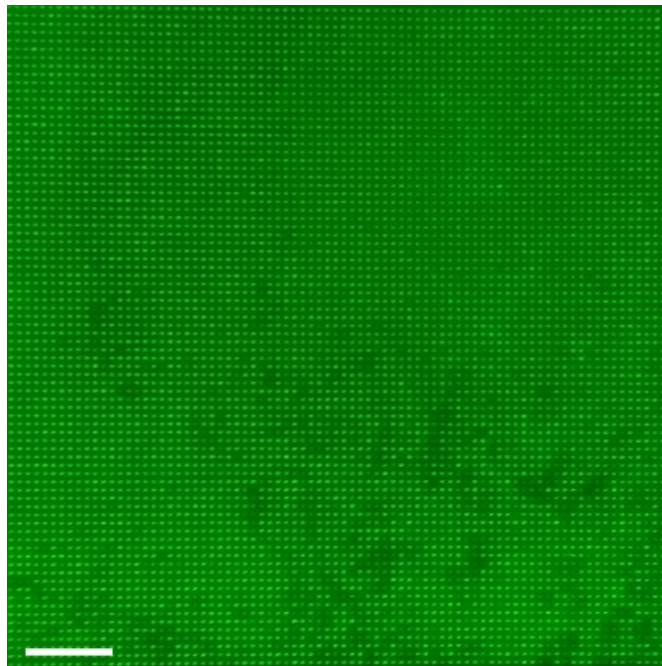


Figure 3-18 The optimized field of view of the monochromatic darkfield image taken by the inexpensive microscope coupled with the smartphone, which shows a 80×80 blocked nanohole array. The scale bar is 20 μm .

To achieve the 400X magnification with a 10X eyepiece and 40X objective, there has to be a distance of about 15 cm between the eyepiece and the objective. According to the microscopic theory, the magnification of the objective is related to the ratio between the distance of the eyepiece and the objective and the focal length of the objective in a finite conjugate microscope system. Thus, a portable device with a 400X magnification has to contain this distance between the eyepiece and the objective. Figure 3-19 shows a schematic of the designed structure of the possible portable device considering the conditions discussed above. A reflection mirror between the eyepiece and the objective is used to shrink the volume of the device. The sample can be fixed on the glass holder by the finger structures. And the exciting light is incident from the backside of the sample to achieve a darkfield effect. The device is also coupled with the smartphone. The user can easily take pictures of the nanohole array samples with their smartphone by this device anywhere outside the laboratory.

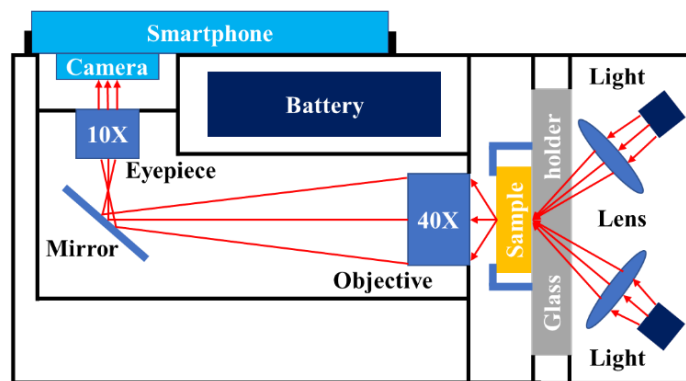


Figure 3-19 The designed structure of the device for point-of-care diagnostic.

3.3 Conclusions

The darkfield images of the empty nanohole array samples indicate a high uniformity and high quality of the nanohole array on gold thin film, which again confirms the success of the previous work in chapter 2. The individual nanohole can be recognized explicitly and easily by the darkfield images. The background of the darkfield images with the perfect configuration is completely dark, and the nanoholes are very bright and clear. The nanohole blocked by a single silica-shelled gold nanosphere shows some interesting phenomena, which can be utilized for blocked nanohole recognition. For the blocked nanoholes, there can be an obvious reduction of the blue and green light but an enhancement of the red light. Since not all the blocked nanoholes have this response and the sizes and positions of the nanospheres vary from one another, this phenomenon should be dependent on the sizes and positions of the silica-shelled gold nanospheres. However, this is hard to be further confirmed by the experiments due to the lack of nanospheres with different sizes as well as the effective control of the nanosphere position inside the nanohole. Thus, the simulation will be conducted to verify the inference. On the other hand, the darkfield images of good quality have been obtained by an inexpensive microscope coupled with the smartphone. It demonstrates the possibility to manufacture a portable and inexpensive device with good imaging quality for POC diagnostics.

Chapter 4 Simulations

4.1 Introduction

Within several decades of history, there are many kinds of approaches developed to model the electromagnetic engineering systems. During the 1960s, the increasing availability of programmable electronic digital computers permitted many frequency-domain approaches to rise markedly. Researchers were able to take advantage of the capabilities afforded by powerful new high-level programming languages and computational speeds that were orders of magnitude faster than possible with the old mechanical calculators before the 1960s. However, these frequency-domain techniques have difficulties and trade-offs. While significant progress has been made in solving the ultra-large systems of equations generated by frequency-domain integral equations, the capabilities of even the latest such technologies are exhausted by many volumetrically complex structures of engineering interest. Further, the very difficult incorporation of material and device nonlinearities into frequency-domain solutions of Maxwell's equations poses a significant problem as engineers seek to design active electromagnetic/electronic and electromagnetic/quantum-optical systems such as high-speed digital circuits, microwave and millimeter-wave amplifiers, and lasers.^[78]

During the 1970s and 1980s, many researchers realized the limitations of frequency-domain integral equation solutions of Maxwell's equations. This led to early explorations of a novel alternative approach: direct time-domain solutions of Maxwell's differential

(curl) equations on spatial grids or lattice. The finite-difference time-domain (FDTD) method introduced by Yee^[79] in 1966, was the first technique in this class and has remained the subject of continuous development.

There are seven primary reasons for the expansion of interest in FDTD and related computational solution approaches for Maxwell's equations:

1. FDTD doesn't use linear algebra. Being a fully direct and explicit computation, it avoids the difficulties with linear algebra that limit the size of a frequency-domain integral equation and finite-element electromagnetics models to generally fewer than 10^6 field unknowns. FDTD models with as many as 10^9 field unknowns have been run. There is no intrinsic upper bound to this number.
2. FDTD is accurate and robust. The sources of error in FDTD calculations are well understood and can be bounded to permit accurate models for a very large variety of electromagnetic wave interaction problems.
3. FDTD treats impulsive behavior naturally. Being a time-domain technique, FDTD directly calculates the impulse response of an electromagnetic system. Therefore, a single FDTD simulation can provide either ultrawideband temporal waveforms or the sinusoidal steady-state response at any frequency in the excitation spectrum.
4. FDTD treats nonlinear behavior naturally. Being a time-domain technique, FDTD directly calculates the nonlinear response of an electromagnetic system.
5. FDTD is a systematic approach. With FDTD, specifying a new structure to be modeled is reduced to a problem of mesh generation rather than the potentially complex

reformulation of an integral equation. For example, FDTD requires no calculation of structure-dependent Green's functions.

6. Computer memory capacities are increasing rapidly. Although this trend positively influences all numerical techniques, it is of particular advantage to FDTD methods that are founded on discretizing space over a volume and that inherently require a large random access memory.
7. Computer visualization capabilities are increasing rapidly. Although this trend positively influences all numerical techniques, it is of particular advantage to FDTD methods that generate time-marched arrays of field quantities suitable for use in color videos to illustrate field dynamics.

An indication of the expanding level of interest in FDTD Maxwell's equations solvers is the hundreds of papers currently published in this area worldwide each year, as opposed to fewer than ten as 1985 and before that year.^[80] This expansion continues as engineers and scientists in nontraditional electromagnetics related areas such as digital systems and integrated optics become aware of the power of such direct solution techniques for Maxwell's equations.

The Finite-Difference Time-Domain method (FDTD) is today's one of the most popular techniques for the solution of electromagnetic problems. It has been successfully applied to an extremely wide variety of problems, such as scattering from metal objects and dielectrics, antennas, microstrip circuits, and electromagnetic absorption in the human body exposed to radiation. The main reason for the success of the FDTD method resides

in the fact that the method itself is extremely simple, even for programming a three-dimensional code.

4.1.1 FDTD Theory

The theory of the FDTD method is simply based on the time-dependent Maxwell's equations in the differential form. To solve an electromagnetic problem, the idea is to simply discretize, Maxwell's equations with central difference approximations both in time and space. The originality of the idea of Yee resides in the allocation in space of the electric and magnetic field components, and the marching in time for the evolution of the procedure.

To better understand how FDTD works, we can start from the three dimensional Maxwell's equations in differential form and suggest that there is no charge and current. The time-dependent Maxwell's equations are given by:

Gauss' law for the electric field:

$$\nabla \cdot \vec{D}(t) = 0, \quad (4 - 1)$$

Gauss' law for the magnetic field:

$$\nabla \cdot \vec{B}(t) = 0, \quad (4 - 2)$$

Faraday's law:

$$\nabla \times \vec{E}(t) = -\frac{\partial \vec{B}(t)}{\partial t}, \quad (4 - 3)$$

and **Ampere's law:**

$$\nabla \times \vec{H}(t) = \frac{\partial \vec{D}(t)}{\partial t}. \quad (4 - 4)$$

Considering the linear, isotropic, and nondispersive materials, which means no field-dependent, direction-dependent, and frequency-dependent electric and magnetic properties, we can have:

$$\vec{D} = \epsilon \vec{E} = \epsilon_0 \epsilon_r \vec{E} \quad (4 - 5)$$

and

$$\vec{B} = \mu \vec{H} = \mu_0 \mu_r \vec{H}. \quad (4 - 6)$$

For Equation 4-1 through 4-6, the following symbols and units are defined:

\vec{E} : Electric field [V/m],

\vec{D} : Electric displacement field or electric flux density [C/m²],

\vec{H} : Magnetic field [A/m],

\vec{B} : Magnetic flux density [T or Wb/m² or kg/(A×s²)],

ϵ : Electrical permittivity [F/m],

ϵ_r : Relative permittivity [dimensionless scalar],

ϵ_0 : Free-space permittivity [8.854×10⁻¹² F/m],

μ : Magnetic permeability [H/m or N/A²],

μ_r : Relative permeability [dimensionless scalar],

μ_0 : Free-space permeability [4π×10⁻⁷ H/m].

Then, we substitute Equations 4-5 and 4-6 into 4-3 and 4-4, respectively. This yields Maxwell's curl equations in linear, isotropic, and nondispersive materials:

$$\nabla \times \vec{E}(t) = -\mu \frac{\partial \vec{H}(t)}{\partial t} \quad (4 - 7)$$

and

$$\nabla \times \vec{H}(t) = \varepsilon \frac{\partial \vec{E}(t)}{\partial t}. \quad (4-8)$$

First, we deal with the time derivative parts of the above equations. For the stable finite-difference equations, each term in a finite-difference equation must exist at the same point in time and space. Thus, we can rewrite the time derivatives in the above equations by:

$$\nabla \times \vec{E}(t) = -\mu \frac{\vec{H}(t + \Delta t/2) - \vec{H}(t - \Delta t/2)}{\Delta t} \quad (4-9)$$

and

$$\nabla \times \vec{H}(t + \Delta t/2) = \varepsilon \frac{\vec{E}(t + \Delta t) - \vec{E}(t)}{\Delta t}. \quad (4-10)$$

Here, we stagger \vec{E} and \vec{H} in time so that \vec{E} exists at integer time steps ($t, t + \Delta t, t + 2\Delta t, \dots$) and \vec{H} exists at half time steps ($t - \Delta t/2, t + \Delta t/2, t + 3\Delta t/2, \dots$). Reordering Equations 4-9 and 4-10, we can obtain the following equations, called “update equations”:

$$\vec{H}(t + \Delta t/2) = \vec{H}(t - \Delta t/2) - \frac{\Delta t}{\mu} (\nabla \times \vec{E}(t)) \quad (4-9a)$$

and

$$\vec{E}(t + \Delta t) = \vec{E}(t) + \frac{\Delta t}{\varepsilon} (\nabla \times \vec{H}(t + \Delta t/2)). \quad (4-10a)$$

With the “update equations”, if we know the initial electric field and magnetic field, we can update $\vec{H}(t + \Delta t/2)$ from $\vec{E}(t)$ and then update $\vec{E}(t + \Delta t)$ from $\vec{H}(t + \Delta t/2)$. Thus, this can form a loop to update the future value of the electromagnetic field from the previous value of the electromagnetic field at each point in time and space.

We now expand the vector components of the curl operations of Equations 4-7 and 4-8 in Cartesian coordinates. This yields the following six-coupled scalar equations:

$$\frac{\partial H_x(t)}{\partial t} = \frac{1}{\mu} \left(\frac{\partial E_y(t)}{\partial z} - \frac{\partial E_z(t)}{\partial y} \right), \quad (4-11)$$

$$\frac{\partial H_y(t)}{\partial t} = \frac{1}{\mu} \left(\frac{\partial E_z(t)}{\partial x} - \frac{\partial E_x(t)}{\partial z} \right), \quad (4-12)$$

$$\frac{\partial H_z(t)}{\partial t} = \frac{1}{\mu} \left(\frac{\partial E_x(t)}{\partial y} - \frac{\partial E_y(t)}{\partial x} \right), \quad (4-13)$$

$$\frac{\partial E_x(t)}{\partial t} = \frac{1}{\varepsilon} \left(\frac{\partial H_z(t)}{\partial y} - \frac{\partial H_y(t)}{\partial z} \right), \quad (4-14)$$

$$\frac{\partial E_y(t)}{\partial t} = \frac{1}{\varepsilon} \left(\frac{\partial E_x(t)}{\partial z} - \frac{\partial E_z(t)}{\partial x} \right), \quad (4-15)$$

and

$$\frac{\partial E_z(t)}{\partial t} = \frac{1}{\varepsilon} \left(\frac{\partial E_y(t)}{\partial x} - \frac{\partial E_x(t)}{\partial y} \right). \quad (4-16)$$

The six-coupled partial differential equations from Equations 4-11 to 4-16 form the basis of the FDTD numerical algorithm for electromagnetic wave interactions with general three-dimensional objects. Previously, we have used centered finite-difference expressions for the time derivatives. Here, we use the same method for the space derivatives in the above six equations. Thus, we can rewrite the space derivatives on the right side of the equations from Equation 4-11 to 4-16. Combining Equations 4-9 and 4-10, we can achieve a finite-difference numerical approximation of the Maxwell's curl equations on both sides of the above equations from Equations 4-11 to 4-16. As we know that each space component is a function of x, y, z, t , we can introduce a simplified notation:

$$F(i\Delta x, j\Delta y, k\Delta z, t) = F^{i,j,k}|_t. \quad (4-17)$$

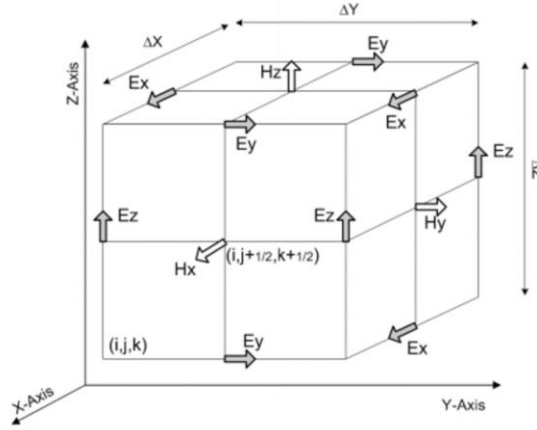


Figure 4-1 Positions of the electric and magnetic field vector components in a cubic unit cell of the space lattice. The E-components are at the middle of the edges and the H-components are at the center of the faces.

And the grid points for the E-field and the H-field are chosen as shown in Figure 4-1.

We begin by considering Equation 4-11 as an example. Referring to Figure 4-1 and applying the above notation, a typical substitution of central differences for the time and space derivatives in Equation 4-11 at $H_x(i, j+1/2, k+1/2, t)$ yields the following expression:

$$\frac{H_x^{i,j+\frac{1}{2},k+\frac{1}{2}} \Big|_{t+\frac{\Delta t}{2}} - H_x^{i,j+\frac{1}{2},k+\frac{1}{2}} \Big|_{t-\frac{\Delta t}{2}}}{\Delta t} = \frac{1}{\mu} \left(\frac{E_y^{i,j+\frac{1}{2},k+1} \Big|_t - E_y^{i,j+\frac{1}{2},k} \Big|_t}{\Delta z} - \frac{E_z^{i,j+1,k+\frac{1}{2}} \Big|_t - E_z^{i,j,k+\frac{1}{2}} \Big|_t}{\Delta y} \right). \quad (4-18)$$

Reordering above equation can yield the following explicit time-stepping relation for H_x :

$$H_x^{i,j+\frac{1}{2},k+\frac{1}{2}} \Big|_{t+\frac{\Delta t}{2}} = H_x^{i,j+\frac{1}{2},k+\frac{1}{2}} \Big|_{t-\frac{\Delta t}{2}} + \frac{\Delta t}{\mu} \left(\frac{E_y^{i,j+\frac{1}{2},k+1} \Big|_t - E_y^{i,j+\frac{1}{2},k} \Big|_t}{\Delta z} - \frac{E_z^{i,j+1,k+\frac{1}{2}} \Big|_t - E_z^{i,j,k+\frac{1}{2}} \Big|_t}{\Delta y} \right). \quad (4-19)$$

Similarly, we can derive finite-difference expressions for the H_y , H_z , E_x , E_y , E_z field components in equations from Equation 4-12 to 4-16. They are as following:

$$\begin{aligned} H_y^{i-\frac{1}{2}j+1,k+\frac{1}{2}} \Big|_{t+\frac{\Delta t}{2}} &= H_y^{i-\frac{1}{2}j+1,k+\frac{1}{2}} \Big|_{t-\frac{\Delta t}{2}} + \\ \frac{\Delta t}{\mu} &\left(\frac{E_z^{ij+1,k+\frac{1}{2}} \Big|_t - E_z^{i-1,j+1,k+\frac{1}{2}} \Big|_t}{\Delta x} - \frac{E_x^{i-\frac{1}{2}j+1,k+1} \Big|_t - E_x^{i-\frac{1}{2}j+1,k} \Big|_t}{\Delta z} \right), \end{aligned} \quad (4-20)$$

$$\begin{aligned} H_z^{i-\frac{1}{2}j+\frac{1}{2},k+1} \Big|_{t+\frac{\Delta t}{2}} &= H_z^{i-\frac{1}{2}j+\frac{1}{2},k+1} \Big|_{t-\frac{\Delta t}{2}} + \\ \frac{\Delta t}{\mu} &\left(\frac{E_x^{i-\frac{1}{2}j,k+1} \Big|_t - E_x^{i-\frac{1}{2}j+1,k+1} \Big|_t}{\Delta y} - \frac{E_y^{ij+\frac{1}{2},k+1} \Big|_t - E_y^{i-1,j+\frac{1}{2},k+1} \Big|_t}{\Delta x} \right), \end{aligned} \quad (4-21)$$

$$\begin{aligned} E_x^{i-\frac{1}{2}j+1,k+1} \Big|_{t+\Delta t} &= E_x^{i-\frac{1}{2}j+1,k+1} \Big|_t \\ + \frac{\Delta t}{\varepsilon} &\left(\frac{H_z^{i-\frac{1}{2}j+\frac{1}{2},k+1} \Big|_{t+\frac{\Delta t}{2}} - H_z^{i-\frac{1}{2}j+\frac{3}{2},k+1} \Big|_{t+\frac{\Delta t}{2}}}{\Delta y} - \frac{H_y^{i-\frac{1}{2}j+1,k+\frac{3}{2}} \Big|_{t+\frac{\Delta t}{2}} - H_y^{i-\frac{1}{2}j+1,k+\frac{1}{2}} \Big|_{t+\frac{\Delta t}{2}}}{\Delta z} \right), \end{aligned} \quad (4-22)$$

$$\begin{aligned} E_y^{ij+\frac{1}{2},k+1} \Big|_{t+\Delta t} &= E_y^{ij+\frac{1}{2},k+1} \Big|_t \\ + \frac{\Delta t}{\varepsilon} &\left(\frac{H_x^{ij+\frac{1}{2},k+\frac{3}{2}} \Big|_{t+\frac{\Delta t}{2}} - H_x^{ij+\frac{1}{2},k+\frac{1}{2}} \Big|_{t+\frac{\Delta t}{2}}}{\Delta z} - \frac{H_z^{i+\frac{1}{2}j+\frac{1}{2},k+1} \Big|_{t+\frac{\Delta t}{2}} - H_z^{i-\frac{1}{2}j+\frac{1}{2},k+1} \Big|_{t+\frac{\Delta t}{2}}}{\Delta x} \right), \end{aligned} \quad (4-23)$$

and

$$\begin{aligned}
& E_z^{i,j+1,k+\frac{1}{2}} \Big|_{t+\Delta t} = E_z^{i,j+1,k+\frac{1}{2}} \Big|_t \\
& + \frac{\Delta t}{\epsilon} \left(\frac{H_y^{i+\frac{1}{2},j+1,k+\frac{1}{2}} \Big|_{t+\frac{\Delta t}{2}} - H_y^{i-\frac{1}{2},j+1,k+\frac{1}{2}} \Big|_{t+\frac{\Delta t}{2}}}{\Delta x} - \frac{H_x^{i,j+\frac{3}{2},k+\frac{1}{2}} \Big|_{t+\frac{\Delta t}{2}} - H_x^{i,j+\frac{1}{2},k+\frac{1}{2}} \Big|_{t+\frac{\Delta t}{2}}}{\Delta y} \right). \quad (4-24)
\end{aligned}$$

The equations from Equation 4-19 to 4-24 are the systems of finite-difference expressions of Maxwell's curl equations in three dimensions for linear, isotropic, and nondispersive materials without current. The new value of an electromagnetic field vector component at any space lattice point depends only on its previous value, and the previous values of the components of the other field vector at adjacent points. Thus, at any given time step, the computation of a field vector can proceed either one point at a time or several points at a time if several parallel processors are employed concurrently. This indicates the core ideas of how the finite-difference time-domain method works for solving problems of the electromagnetic system.

4.1.2 The condition of the numerical stability

Within the computation, the error always exists because of the finite-difference approximation. The time step and space steps need to satisfy a certain relation, otherwise the computation will be unstable as the time is proceeding. The instability is shown as follows: with the increase of the number of steps, the value of the computational field will increase infinitely. This increase is not caused by the accumulation of errors, but by the

destruction of the propagation relationship of electromagnetic waves. Taflove's group^[81] indicated in 1975 that the Δt is chosen to satisfy the Equation 4-25 to ensure the stability of the systems of the above six finite-difference equations, and that the corresponding stability criterion proposed by Yee in 1966 is incorrect.

$$v_{max}\Delta t \leq \left(\frac{1}{(\Delta x)^2} + \frac{1}{(\Delta y)^2} + \frac{1}{(\Delta z)^2} \right)^{-1/2}, \quad (4 - 25)$$

where v_{max} is the maximum wave phase velocity expected within the model.

4.1.3 Numerical dispersion

In FDTD grids, the digital wave modes will change. This change is caused by the computational grid itself, not by physical factors, so it must be considered. In other words, in FDTD grids, the phase velocity of the electromagnetic wave is related to frequency and varies with wavelength, propagation direction, and variable discretization. This numerical dispersion caused by nonphysical factors will lead to pulse waveform distortion, artificial anisotropy, and false refraction. The general form of the numerical dispersion relation for the full vector-field Yee algorithm in three dimensions is:

$$\left[\frac{1}{c\Delta t} \sin\left(\frac{\omega\Delta t}{2}\right) \right]^2 = \left[\frac{1}{\Delta x} \sin\left(\frac{k_x\Delta x}{2}\right) \right]^2 + \left[\frac{1}{\Delta y} \sin\left(\frac{k_y\Delta y}{2}\right) \right]^2 + \left[\frac{1}{\Delta z} \sin\left(\frac{k_z\Delta z}{2}\right) \right]^2. \quad (4 - 26)$$

In contrast to Equation 4-26, the analytical dispersion relation for a physical plane wave propagating in three dimensions in a homogeneous lossless medium is simply:

$$\left(\frac{\omega}{c}\right)^2 = (k_x)^2 + (k_y)^2 + (k_z)^2. \quad (4 - 27)$$

Equations 4-26 and 4-27 seem to have little resemblance at first glance, while it can be easily demonstrated that they are identical when Δt , Δx , Δy , and Δz are approaching zero. That is, the numerical dispersion is caused by the substitution of approximate difference for continuous differentiation, and theoretically can be reduced to any degree, as long as the time step and the space step are fine enough.

4.1.4 Summary

In this work, we have used the finite-difference time-domain method to simulate the dark-field imaging of the blocked and unblocked nanoholes in the gold film on the glass substrate. The Lumerical's FDTD solutions software is used to perform the simulation tasks on the computer. To better understand how the nanosphere inside the nanohole interacts with the incident light, different sizes of the nanospheres and different positions of the nanosphere inside the nanohole are applied to the simulation structures. Three single wavelengths, 488 nm, 550 nm, 641 nm, are used for the plane wave light source, respectively corresponding to the blue, green, and red channels in the image analysis field.

4.2 Results and Discussion

4.2.1 Simulation configuration

Figure 4-2 shows the side view and top view of the simulated structure. The simulated structure contains two nanoholes, of which the diameter is 150 nm and the distance is 2 μm . One of the nanoholes is empty and the other one is blocked by a silica-shelled gold

nanosphere, of which the silica shell thickness is 20 nm and the gold core diameter is 70 nm, initially. From the top view, the nanosphere is located at the center of the nanohole. The single wavelength plane wave light source is incident at an angle of 54° from the glass side. Two polarizations of the incident light are chosen as shown in Figure 4-3. The P polarization indicates that the vibration direction of the electric field is in the XZ plane, while the S polarization indicates that the vibration direction of the electric field is in the YZ plane. The surface monitor is located 100 nm above the surface of the gold film. The simulated area of the XY plane is $4 \mu\text{m} \times 2 \mu\text{m}$. The minimum mesh size is set to 2.5 nm since there is a 5 nm Cr layer in the simulated structure. The perfect matched layer is used for the boundary conditions, which can absorb incident light with minimal reflections.

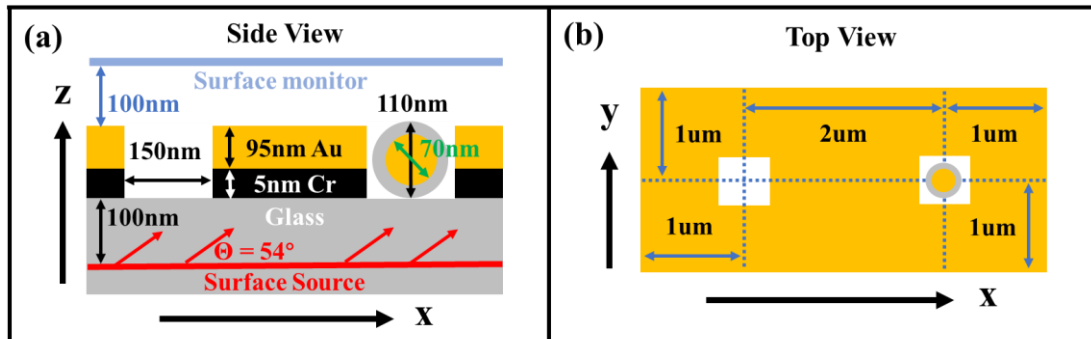


Figure 4-2 The simulation configuration of the nanoholes structure. (a) Side view of the simulated area and (b) top view of the simulated area.

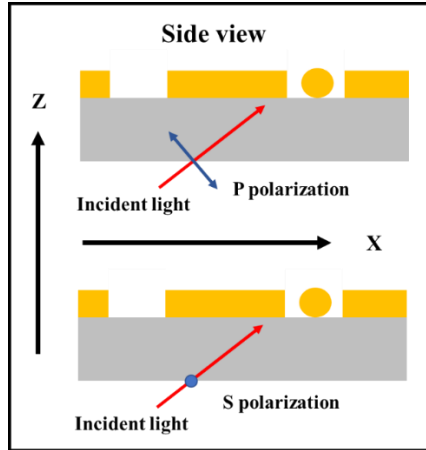


Figure 4-3 Polarizations of the incident light. Red arrows are propagating direction of the incident light. Blue arrows are polarization of the electric field. P polarization is in XZ plane and S polarization is in YZ plane.

As the simulation results only contain the data of the near field, an analysis script is used to post-process simulation monitor data such that it can be compared to experimental images obtained from a microscope with a given numerical aperture. To do this, near field monitor data is decomposed into a series of plane waves, which propagate at different angles. Any plane waves with angles outside of the NA are then discarded. Finally, the remaining light is re-focused onto an image plane. The script does this calculation and produces an image of the final result. This script does not include a magnification factor for the lens system, while it does include a defocus setting which allows us to consider the imaged light at a specified distance from the focal plane. Figure 4-4 shows the schematic of the simplified imaging system, which is achieved by the analysis script described above. A lens system takes light from the specimen and focuses it onto an image plane. At some point in the system, an aperture limits the angles of light that can travel through the lens system to create the final image.

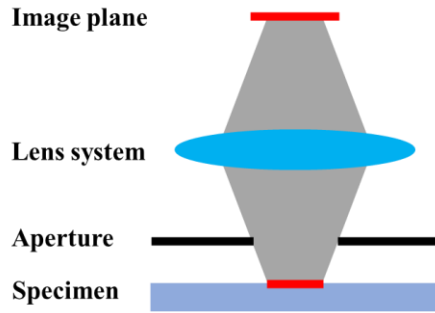


Figure 4-4 The schematic of a simplified imaging system.

4.2.2 Different sizes of the nanosphere

Since the diameters of nanospheres are always within a range, different sizes of the nanospheres are applied to the simulation. The silica-shelled gold nanospheres we have used in the experiment have a silica shell of 20 nm thickness and a gold core of 70 nm diameter. In the simulation, we keep the thickness of the silica shell unchanged and change the diameter of the gold core from 0 to 100 nm with the 10 nm increment. We use a specific notation for each case, such as 70+40 for a nanosphere with a gold core of 70 nm diameter and a silica shell of a total of 40 nm thickness. The sum of core+shell shows the total diameter of the nanosphere used.

Figure 4-5 shows the near field intensity distributions of the structure, shown in Figure 4-3, which is excited by the 488 nm, 550 nm, and 641 nm light with P and S polarizations respectively. The silica-shelled nanosphere, with a 70 nm core diameter and a 20 nm thick shell, is at the center of the right side nanohole. The results indicate that whatever the polarization of the exciting light is, the green light has a larger reduction than the blue light for the blocked nanohole, while the red light has an obvious enhancement for the blocked

nanohole. The intensity distribution of the S polarization for each light is more smooth than that of the P polarization in the area between the nanoholes.

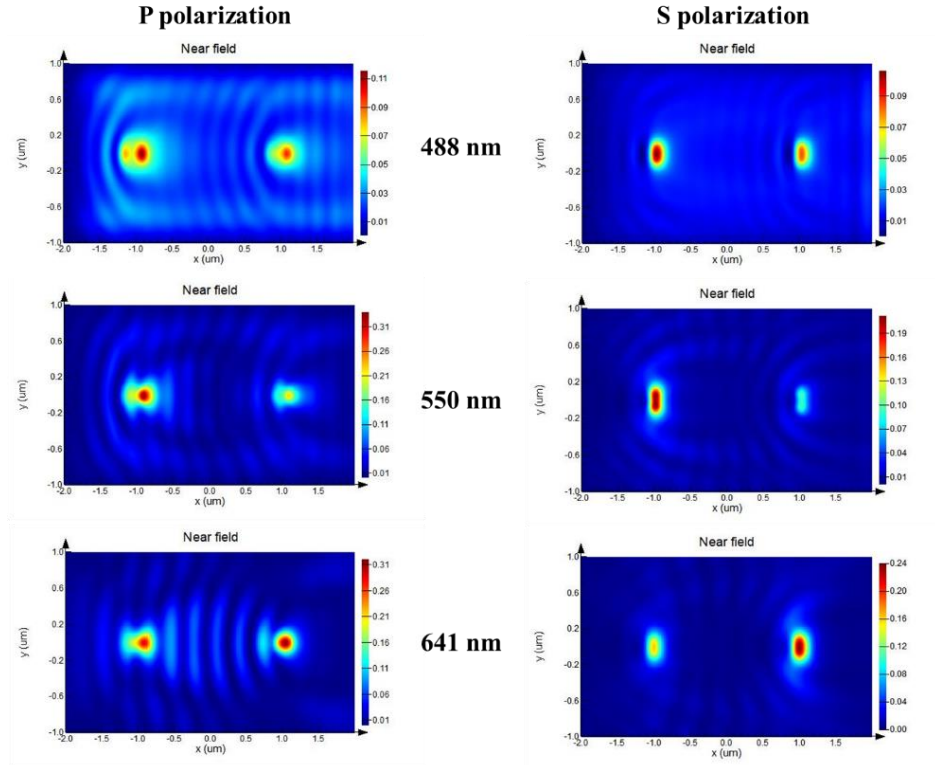


Figure 4-5 Near field intensity distributions of 488, 550, and 641 nm exciting light with P and S polarization. The right nanohole is blocked by a silica-shelled gold nanosphere with 70 nm core diameter and 20 nm thick shell.

To study the size dependence of the intensity change for the blocked nanohole, different sizes of the nanosphere at the same position have been applied to the simulation. The microscopic imaging with $NA = 1$ of the far field is also derived from the data of the near field. And the intensity ratios between the blocked and unblocked nanoholes of both the near and far field are calculated and summarized. Figure 4-6 shows the results of the 488 nm exciting light with P and S polarizations respectively. The near field data and the far field data have almost the same trend for both polarizations. The ratios have nearly no

change at the small core diameter range but decrease quickly when the core diameter is larger than 60 nm. Figure 4-7 shows the results of the 550 nm exciting light with P and S polarizations respectively. They have a similar trend with the results of the 488 nm exciting light. However, the ratios of the green light decrease much faster than those of the blue light when the core diameter is larger than 50 nm. Figure 4-8 shows the results of the 641 nm exciting light with P and S polarizations respectively. These results of 641 nm are very different from those of 488 nm and 550 nm. The ratios of the red light can be dramatically larger than 1 for both polarizations of the far field in the core diameter range from 50 to 80 nm, which means an obvious enhancement of red light in the microscopic imaging. Theoretically, the near field data should contain the nonradiative component that is coupled near the surface of the gold thin film, and the radiative component that results in the far field data. For the P polarization of the red light shown in Figure 4-8 (a), the far field ratios are larger when the core diameter is smaller than 90 nm, which means that the near field data of the blocked nanohole has a higher ratio of the radiative component than those of the unblocked nanohole. While for the S polarization of the red light shown in Figure 4-8 (b), the radiative and nonradiative components have the same ratio in the near field data of both the blocked and unblocked nanoholes. However, the maximum ratios for the P and S polarizations are almost the same when the core diameter is 70 nm, which indicates that both polarizations have the same contribution to the enhancement of the red light in the microscopic imaging of the far field.

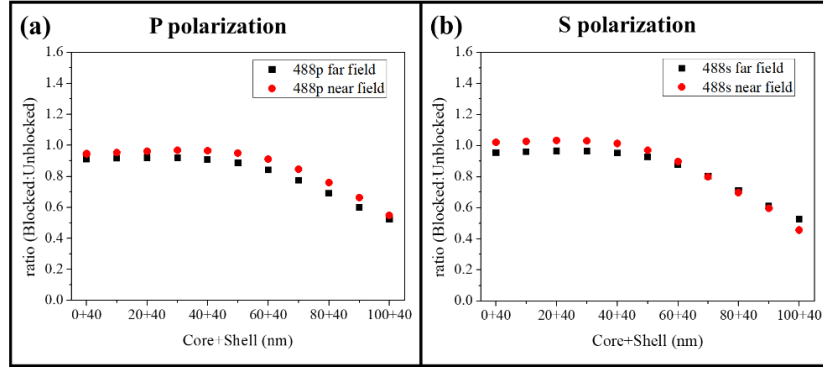


Figure 4-6 Intensity ratios between the blocked and unblocked nanoholes at 488 nm wavelength of (a) P and (b) S polarizations for near field (red dots) and far field (black squares). The nanosphere is at the center of the nanohole.

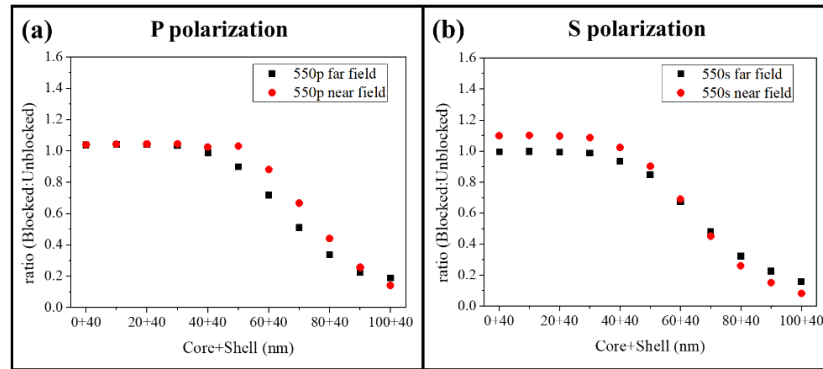


Figure 4-7 Intensity ratios between the blocked and unblocked nanoholes at 550 nm wavelength of (a) P and (b) S polarizations for near field (red dots) and far field (black squares). The nanosphere is at the center of the nanohole.

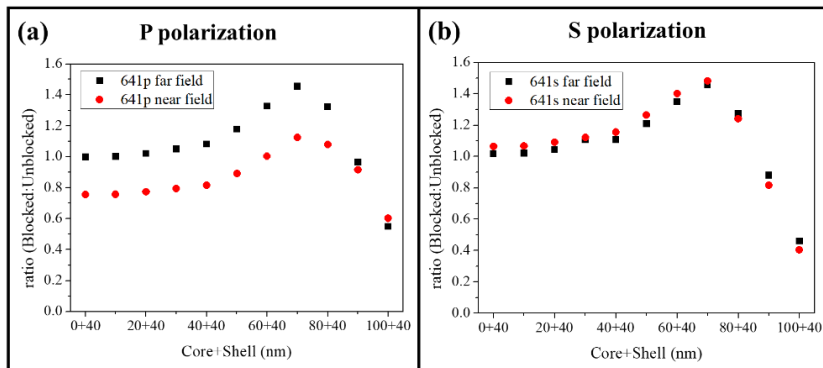


Figure 4-8 Intensity ratios between the blocked and unblocked nanoholes at 641 nm wavelength of (a) P and (b) S polarizations for near field (red dots) and far field (black squares). The nanosphere is at the center of the nanohole.

4.2.3 Different positions of the nanosphere

To investigate the position dependence of the intensity change for the blocked nanohole, two different positions of the nanosphere inside the nanohole have been applied to the simulation. The microscopic imaging with $NA = 1$ of the far field is also derived from the data of the near field. And the intensity ratios between the blocked and unblocked nanoholes of both the near and far field are calculated and summarized. The first position of the nanosphere inside the nanohole is at the edge, shown in Figure 4-9. This position change results in a larger distance between the nanohole edge and the nanosphere in the X direction. The trend of the ratio change for the 488 nm exciting light is similar to the previous structure for both the polarizations and for both the near and far field, which is shown in Figure 4-10. This position change has nearly no influence on the blue light. For the results of the green light shown in Figure 4-11, there is almost no change for the S polarization. But the ratios begin to decrease at a smaller core diameter for the P polarization since the space between the nanohole edge and the nanosphere in the X direction is larger. Also, this position change has nearly no influence on the S polarization of the red light but some influence on the P polarization, shown in Figure 4-12. The maximum intensity ratio of the far field for P polarization has a dramatic reduction but still a little larger than 1 and moves to the 60 nm core diameter. And the maximum intensity ratio of the near field for P polarization has a small reduction as well but finally smaller than 1.

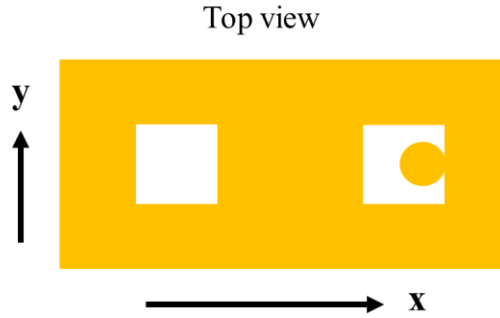


Figure 4-9 Top view of the simulated structure with a nanosphere at the edge of the nanohole.

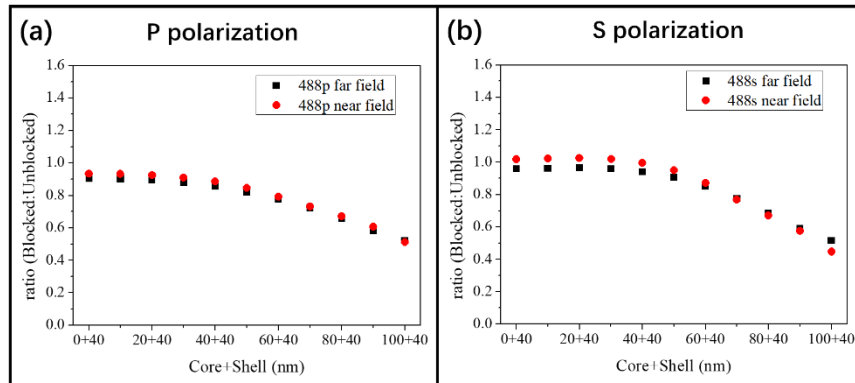


Figure 4-10 Intensity ratios between the blocked and unblocked nanoholes at 488 nm wavelength of (a) P and (b) S polarizations for near field (red dots) and far field (black squares). The nanosphere is at the edge of the nanohole.

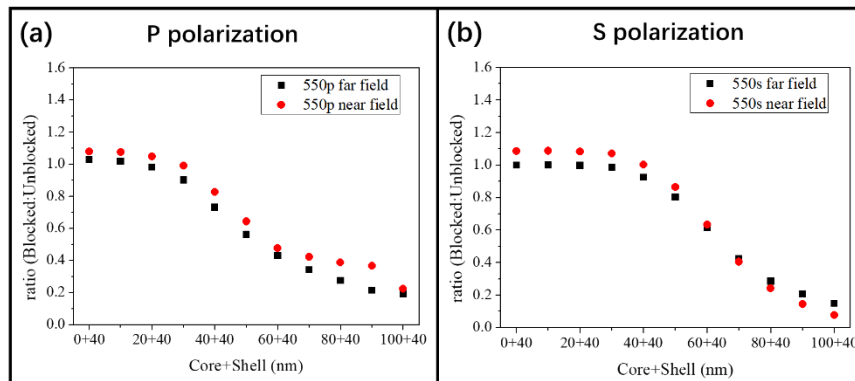


Figure 4-11 Intensity ratios between the blocked and unblocked nanoholes at 550 nm wavelength of (a) P and (b) S polarizations for near field (red dots) and far field (black squares). The nanosphere is at the edge of the nanohole.

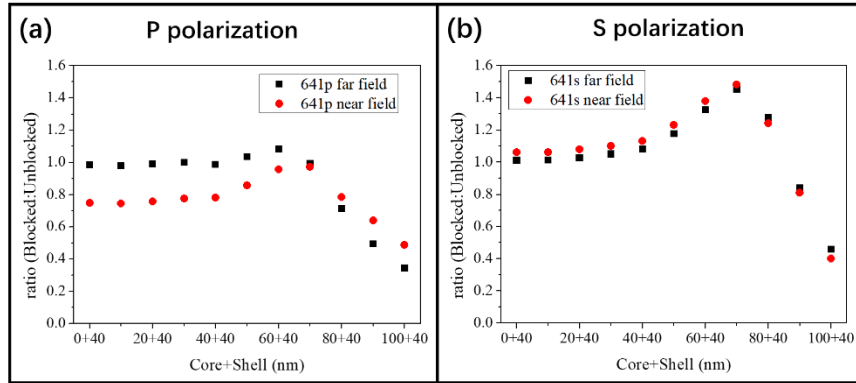


Figure 4-12 Intensity ratios between the blocked and unblocked nanoholes at 641 nm wavelength of (a) P and (b) S polarizations for near field (red dots) and far field (black squares). The nanosphere is at the edge of the nanohole.

The second position of the nanosphere inside the nanohole is at the corner, shown in Figure 4-13. This position change results in a larger distance between the nanohole edge and the nanosphere in both the X and Y direction compared with the original position. Figure 4-14 shows the results of the blue light. As with the first position, this position change has nearly no influence on the blue light because of the similar proximity change between the nanohole edge and the nanosphere in the Y direction to that of the first position in the X direction. And for the green light shown in Figure 4-15, the results for the P polarization are nearly the same as those of the first position, while the intensity ratios for the S polarization begin to decrease at a smaller core diameter because the distance between the nanohole edge and the nanosphere in the Y direction becomes larger. Figure 4-16 (a) shows that the results of the red light for P polarization is similar to those of the first position. However, the maximum intensity ratios of both the near field and far field decrease but are still larger than 1, shown in Figure 4-16 (b).

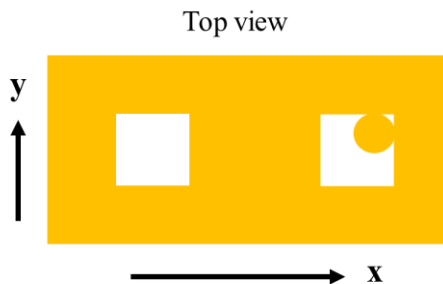


Figure 4-13 Top view of the simulated structure with a nanosphere at the corner of the nanohole.

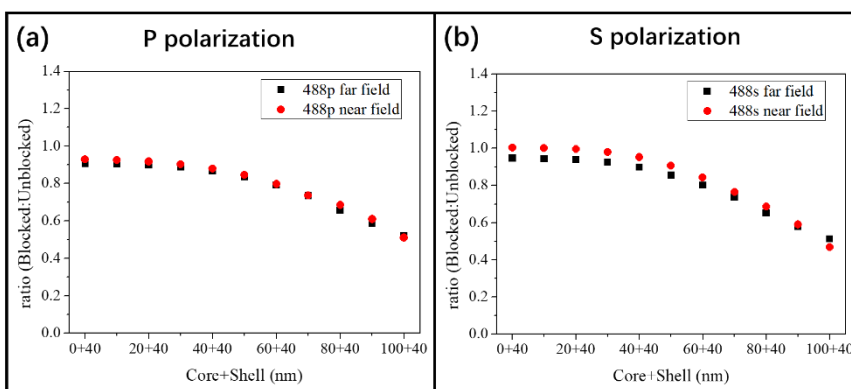


Figure 4-14 Intensity ratios between the blocked and unblocked nanoholes at 488 nm wavelength of (a) P and (b) S polarizations for near field (red dots) and far field (black squares). The nanosphere is at the corner of the nanohole.

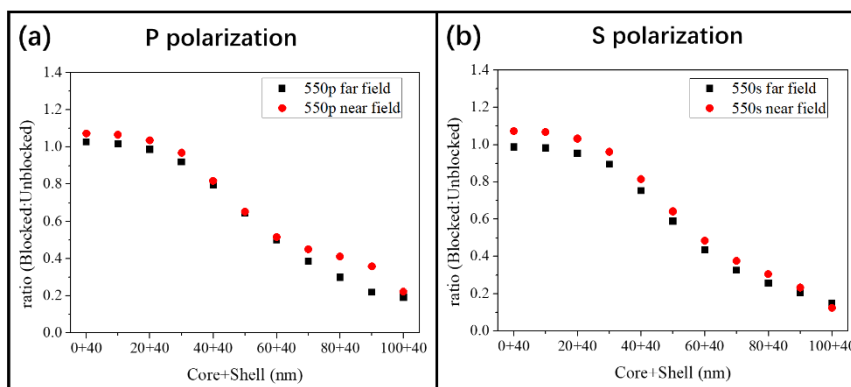


Figure 4-15 Intensity ratios between the blocked and unblocked nanoholes at 550 nm wavelength of (a) P and (b) S polarizations for near field (red dots) and far field (black squares). The nanosphere is at the corner of the nanohole.

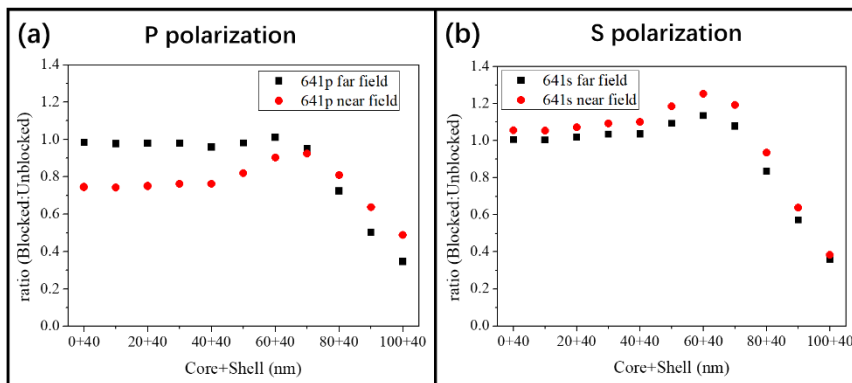


Figure 4-16 Intensity ratios between the blocked and unblocked nanoholes at 641 nm wavelength of (a) P and (b) S polarizations for near field (red dots) and far field (black squares). The nanosphere is at the corner of the nanohole.

4.2.4 Different wavelengths of the exciting light

Furthermore, different wavelengths of the exciting light are simulated to obtain the intensity ratios between the blocked and unblocked nanoholes. The silica-shelled gold nanosphere is at the center of the nanohole with a gold core of 70 nm diameter and a silica shell of 20 nm thickness. Figure 4-17 shows the far field results of the wavelength-dependent intensity ratios for the P polarization and S polarization respectively. Both curves have the same trend that they decrease first and then increase with the increase of the wavelength in the visible light region. They show a similar minimum intensity ratio between 525 and 550 nm, and both reach as high as 1.6 at 700 nm. The shapes of the curves are very similar to the shape of the spectrum shown in Figure 3-6 (c). Since the spectrum in Figure 3-6 (c) is an average spectrum of several blocked nanoholes with the nanosphere of different sizes and positions, it is reasonable that the values of the intensity ratios have some difference. While Figure 4-17 shows the results of the blocked nanohole with the

nanosphere of the specific size and position, which have a good agreement with the experimental results of the darkfield imaging.

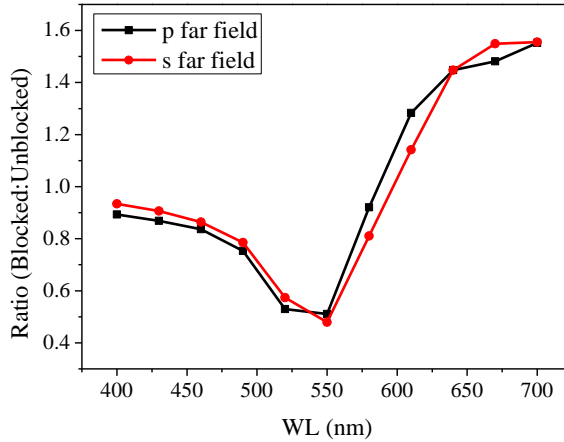


Figure 4-17 Intensity ratios between the blocked and unblocked nanoholes at different wavelengths of the exciting light with the P and S polarizations.

4.2.5 Positions of the nanosphere above the nanohole

Considering the future detection of the analyte, which will be combined with the nanosphere, the analyte may stay inside the nanohole and keep the nanosphere outside the nanohole. Thus, the situations have been also simulated when the nanosphere is above the nanohole at the center position and edge position, which are shown in Figure 4-18. The silica-shelled gold nanosphere has a 70 nm core diameter and a 20 nm shell thickness. The far field results of the P and S polarizations are obtained for the blue, green, and red light. The intensity ratios between the blocked and unblocked nanoholes are calculated and shown in Figure 4-19. It shows similar results to those when the nanosphere is inside the nanohole. As long as the nanosphere is close to the nanohole, whatever it is inside the

nanohole or above the nanohole, the blue and green light can have an obvious reduction while the red light can have a pronounced enhancement for this size. The green light still has a larger reduction than the blue light.

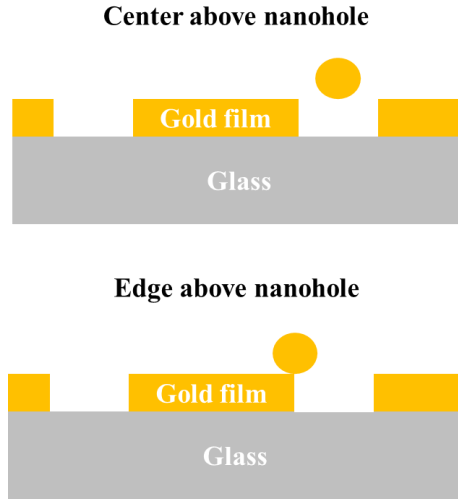


Figure 4-18 Side views of the positions when the nanosphere is above the nanohole at the center position or edge position.

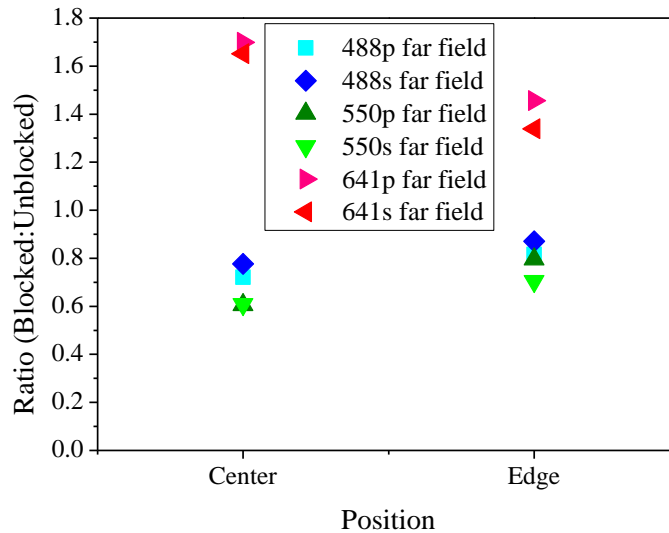


Figure 4-19 Intensity ratios between the blocked and unblocked nanoholes at 488, 550, and 641 nm wavelength of P and S polarizations. The nanosphere is above the nanohole at the center position or edge position.

4.3 Conclusions

The simulation results show that generally with the increase of the gold core diameter, the intensity of the blue light for the blocked nanohole decreases slowly, and the intensity of the green light for the blocked nanohole decreases quickly. However, the intensity of the red light for the blocked nanohole increases first and then decreases very fast with the increase of the gold core diameter. The maximum ratio of the red light between the blocked and unblocked nanoholes can be as high as 1.5, which means an obvious enhancement of the red light. The simulation results of the position changes show that the intensity of the blue light for the blocked nanohole almost hasn't been influenced, but the intensity of the green light and red light have been influenced more or less. The simulation results have a good agreement with the results of the color analysis and spectra analysis in chapter 3. They both show that the red light can have an enhancement at a certain size range and different positions, and the green light is the best choice to recognize the blocked nanoholes because it has the largest reduction of light intensity for the blocked nanoholes. They indicate the silica-shelled gold nanospheres with a gold core of 70 nm diameter and a silica shell of 20 nm thickness, which are used to block the nanoholes, have a suitable size because the blocked nanoholes can have the largest enhancement of the red light and a pronounced reduction of the green light. The simulations help us understand the phenomena in the darkfield imaging and guide us to choose the best configuration for future experiments.

Chapter 5 Smartphone Application of Nanohole Array Sensing

5.1 Introduction

In recent years, smartphone-based mobile devices have been largely developed in the area of food safety, environmental monitoring, and health care, etc. These devices can be used as on-site detection platforms to detect allergens or hormones in food^[82,83], measure the concentration of metal ions in water^[84,85], monitor vital status^[86], count the number of cells^[87], and so on. Since the smartphone is a cost-effective and powerful portable device with high-quality digital cameras, excellent computer processors, touchscreen interface, and wireless data transfer, it can be used as the microscope, instrumental interface, experimental result reader, data calculator, and analyzer.^[88,89] In the biomedical field, by substituting the expensive and complex equipment with smartphone-based devices, not only the health care cost can be dramatically reduced, but the POC testing for on-site measurement and diagnostics in remote areas and resource-limited regions can be easily achieved.^[90] Smartphone-based POC detection or testing platform allows immediate data collection, fast data analysis, and communication with remote medical centers or doctors via the wireless network. The data can be saved with time and GPS location information, which may facilitate the epidemiological studies and establishment of spatiotemporal disease prevalence maps.^[91] Due to these benefits, many types of smartphone-based POC optical devices have been developed, such as imaging^[92-96], colorimetric sensing^[97-101], fluorescence sensing^[102-104], optical spectrum sensing^[105-108], SPR sensing^[109-111], etc.

Some of these devices are served only as an image reader or a data transfer medium and need to connect with a server to analyze the data, and the others can analyze the sample images on the smartphone.

To follow the trend to replace large and expensive equipment with the portable and inexpensive device, efforts are made to apply the smartphone to the nanohole array sensing, which is promising for POC diagnostics. In the previous chapter, it is proved that the images with good quality of our nanohole array samples can be obtained by the home-made darkfield microscope setup coupled with a smartphone. To take full advantage of the powerful smartphone, a matched smartphone application is also developed with many image analysis functions, which are adjusted specifically for our situation. As we are using an android based smartphone, the smartphone application is developed by the Android Studio, a free software supported by the Google company. And the main language for coding is Java. Furthermore, the OpenCV library is also introduced into the Android Studio since it contains many useful and powerful functions for image processing. The main codes of the smartphone application used in the Android Studio are listed in the appendices.

5.2 Results and Discussion

5.2.1 Home page of the smartphone application

Figure 5-1 shows the home page of the Nanohole_Array_Sensor application. There are many buttons with different functions, several image areas to show images, and a text area to show the results of the analyzed image. The button of LOAD AN IMAGE is to load an

image to the Image1 area from the internal storage of the smartphone. The button of TAKE A PHOTO is to take a picture by the smartphone camera and load the picture to the Image1 area. The button, SAVE, is to save the text in the Results area to the internal storage of the smartphone as a file of the text form. The button, SAVE2, is to save the image in Image2 area when the Image3 area is empty, or the image in Image3 area when Image3 area is not empty, to the internal storage of the smartphone as a file of the jpg form.

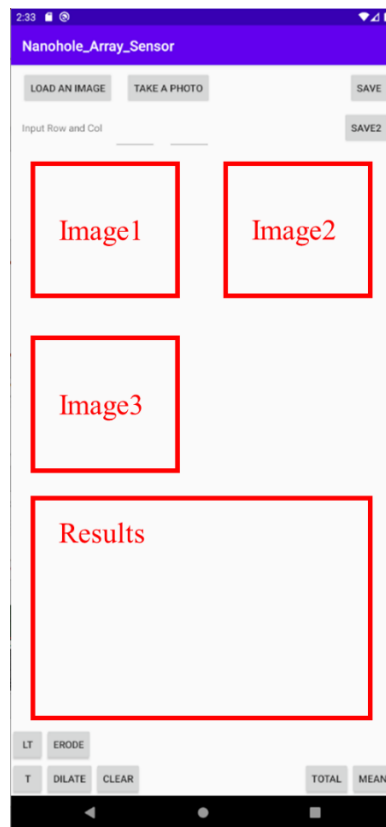


Figure 5-1 The home page of the Nanohole_Array_Sensor application.

5.2.2 Global threshold and local threshold

After loading an image to the Image1 area, which is chosen to be analyzed, there are many functional buttons at the bottom that can be used to process the image and show data

results. First of all, the threshold method is utilized to threshold the image into a binary image, which will be shown in Image2 area. The buttons, T and LT, at the bottom of the home page, provide two threshold strategies that are called the global threshold and the local threshold, respectively. These two threshold methods are both based on the Otsu threshold algorithm.^[112] The Otsu's method is a well-known method for thresholding an image. It works very well for the image with only background and foreground, which is exactly the case in our situation. The nanoholes in the image are the foreground and the space between nanoholes is the background. For this kind of image, it means the histogram of pixel intensity has a bimodal distribution and usually possesses a deep and sharp valley between the two peaks. For a given possible threshold value, the goal of Otsu's method is to calculate the within-class variance or to calculate the between-class variance in a simpler and faster way. When the within-class variance is the minimum or the between-class variance is the maximum, the given threshold value is the best choice. The equations of the within-class variance and the between-class variance are as follows:

$$\sigma_W^2 = W_b \sigma_b^2 + W_f \sigma_f^2 \quad (5 - 1)$$

and

$$\begin{aligned} \sigma_B^2 &= \sigma^2 - \sigma_W^2 \\ &= W_b (\mu_b - \mu)^2 + W_f (\mu_f - \mu)^2 \\ &= W_b W_f (\mu_b - \mu_f)^2, \end{aligned} \quad (5 - 2)$$

where $\sigma, \sigma_W, \sigma_B, \sigma_b,$ and σ_f are the total variance, within-class variance, between-class variance, the variance of the background and the variance of the foreground, respectively; W_b and W_f are the weight of the background and the weight of the foreground,

respectively; μ , μ_b and μ_f are the total mean, the mean of the background and the mean of the foreground, respectively. Since the variance is more complex to be calculated than the weight and the mean, the calculation of the between-class variance is easier than that of the within-class variance.

The threshold methods are to recognize the nanoholes in the darkfield image, locate their positions, and determine their size or area. The difference between the global threshold and local threshold is that the former processes the whole image while the latter divides the image into several small parts and processes each part individually. Figure 5-2 shows the original darkfield image of the blocked nanohole array on the top, and the images that are processed by the global threshold and local threshold on the bottom. The original darkfield image is taken by the CCD with the professional darkfield microscope. Some blocked nanoholes with very low intensity can't be recognized by the global threshold but can be recognized by the local threshold. It is obvious that the blocked nanoholes have smaller areas than the unblocked ones by the global threshold. However, this phenomenon is not pronounced by the local threshold. Usually, the local threshold method is better than the global threshold when the background is not uniform. But when the local foreground is similar to the local background, the local threshold will have a bad performance at that local area. Thus, the selection of the two threshold methods depends on the property of the analyzed image on a case-by-case basis.

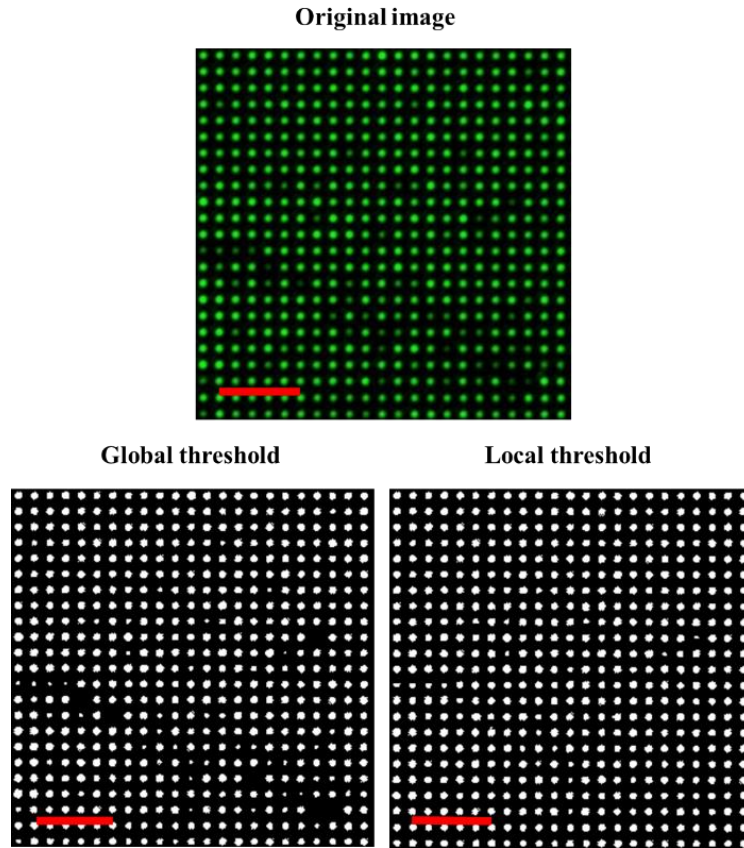


Figure 5-2 Original darkfield image processed by the global threshold and local threshold methods. The scale bars are all 10 μm .

5.2.3 Erosion and dilation operations

After the threshold of the image, sometimes there will be connected nanoholes and noisy points in the binary image due to the defects of the samples. Here, the erosion and dilation operations of the binary image are integrated into the smartphone application. Two corresponding buttons, ERODE and DILATE, are at the bottom of the home page shown in Figure 5-1. Just as their names imply, the erosion function is to decrease the area of the foreground spots in the binary image, and the dilation function is to increase the area of the foreground spots in the binary image. The middle image of Figure 5-3 shows the result of

the global threshold of the original image, which is taken by the smartphone from the eyepiece of the professional microscope with a home-made darkfield setup. The red square circles the two nanoholes which connect to each other. Then, the middle image is eroded two times and dilated once to obtain the right image. As a consequence, the connected nanoholes are successfully separated and most of the other nanoholes maintaining nearly the same size as before the operations. Figure 5-4 shows another example of how to eliminate the noisy point of the image. Similarly, the middle image is the result of the global threshold of the original image, which is taken by the smartphone from the eyepiece of the professional microscope with a home-made darkfield setup. And the red circle indicates the location of the noisy point among the nanoholes. After the middle image is eroded three times and then dilated three times, the result is shown in the right image of Figure 5-4. Finally, the noisy point is eliminated indicating by the red circle in the right image. Although most of the nanoholes maintain almost the same size as before the erosion and dilation operations, some of the extremely small nanohole spots disappear as well. In a word, the erosion operation can remove spots from small to large depending on the number of operations. When eroding the noisy points, the nanohole spots that are smaller than the noisy point will be eliminated as well. In addition, the dilation operation can increase the size of the nanohole spots after they are eroded. The combinations of the erosion and dilation operations can not only separate the connected nanoholes and remove the noisy points but also control the size of the nanohole spots, which will influence the histogram calculation in the following steps.

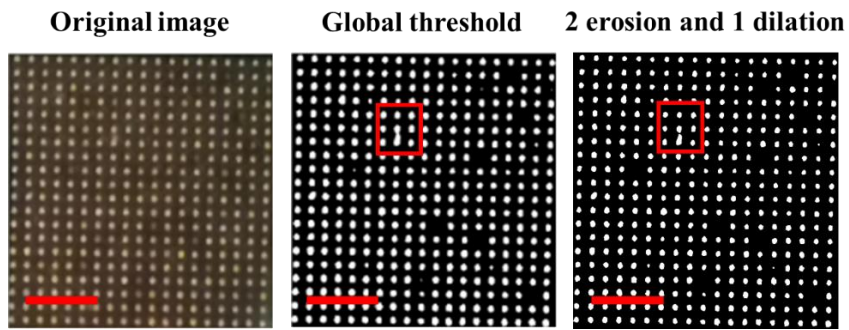


Figure 5-3 Separation of the connected nanoholes of the original darkfield image, which is processed first by the global threshold and then by the erosion and dilation operations. The scale bars are all 10 μm .

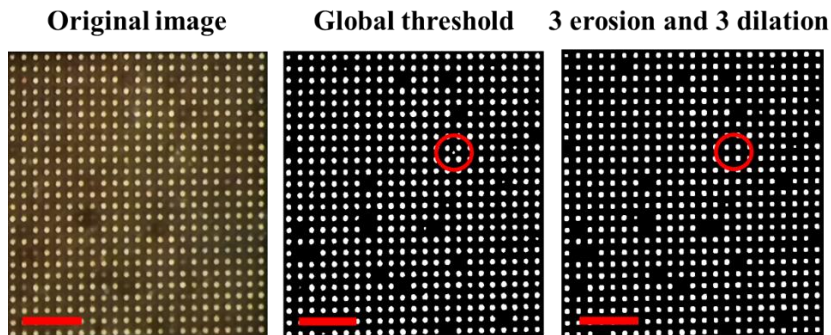


Figure 5-4 Elimination of the noisy point of the original darkfield image, which is processed first by the global threshold and then by the erosion and dilation operations. The scale bars are all 10 μm .

5.2.4 Calculation of the number of blocked nanoholes by the histogram and direct counting

The most important function of the smartphone application is to calculate the number of the blocked nanoholes in a nanohole array image. The application offers two strategies, which are using the total intensity of each nanohole and the mean intensity of each nanohole. They are corresponding to the buttons, TOTAL and MEAN, respectively. Since each nanohole spot contains many pixels, the total intensity of a nanohole means adding

all the pixel intensities included by a nanohole spot in the binary image, and the mean intensity means calculating the mean intensity of all the pixels included by a nanohole spot in the binary image. First, these two methods use the binary image obtained by the threshold methods to locate the positions and sizes of all the nanoholes in the original darkfield image. Second, they use the original darkfield image to obtain the intensity information according to the positions and sizes of all the nanoholes known in the previous step. Finally, in terms of the methods the user has chosen, the total intensity or the mean intensity of each nanohole will be calculated and displayed in the Results area on the home page shown in Figure 5-1. Besides the intensity information, three other values, the threshold value, the number of the unblocked nanoholes, and the number of the total nanoholes, will be displayed as well above the intensity information.

Figure 5-5 shows an example of the histograms of the empty nanohole arrays. Since our smartphone application hasn't included graph function yet, these histograms are drawn by the Origin software on the computer in terms of the intensity information displayed in the Results area. Figure 5-5 (a) is the white light darkfield image of the empty nanohole array, and Figure 5-5 (b) is the green light darkfield image of the empty nanohole array at the same position. Both of the images are taken by the smartphone with the home-made inexpensive darkfield microscope. Both the histograms are within a range of about 25, which indicates that the uniformity of the nanoholes is good.

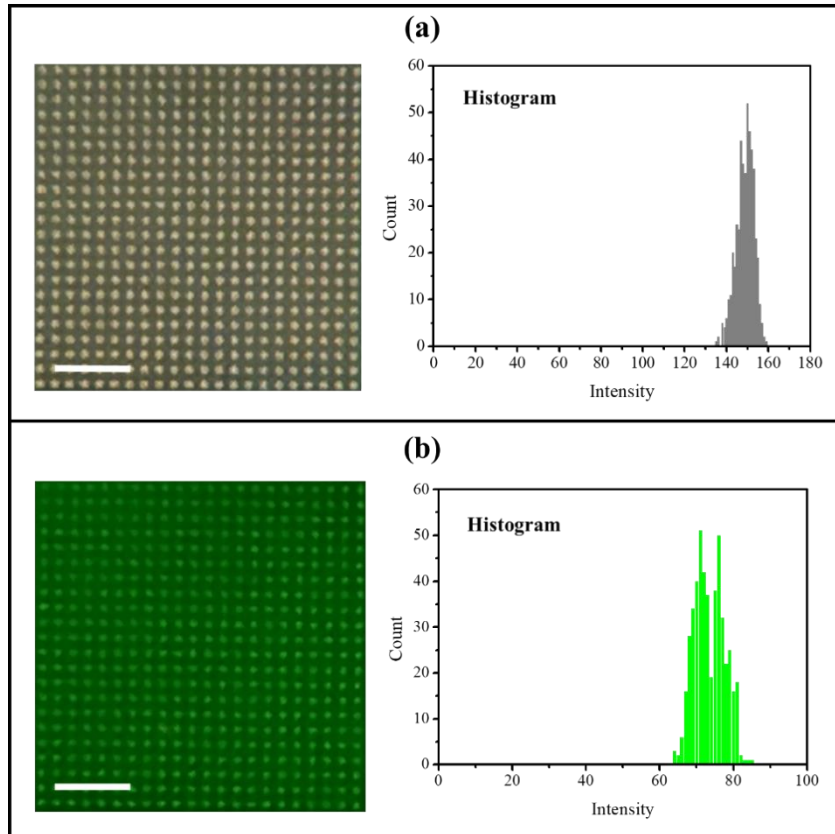


Figure 5-5 Darkfield images and histograms of empty nanohole arrays (a) without green filter and (b) with green filter. The scale bars are both 10 μm .

Figure 5-6 (a) shows an example of the blocked nanohole array analyzed by the histogram. The original darkfield image, shown in Figure 5-6 (b), is taken by the CCD with the professional darkfield microscope. It is obvious that there are nine nanoholes that are blocked by the nanosphere since they have a lower intensity than the others. The binary image, shown in Figure 5-6 (c), is obtained by the local threshold followed by the one-time erosion and one-time dilation operation. Then, the MEAN function is performed to obtain the mean intensity information of each nanohole since the nanoholes have similar sizes in the threshold image. Finally, the intensity values of all the nanoholes are collected and form

the histogram shown in Figure 5-6 (d). The red circle indicates the group of blocked nanoholes at the lower intensity region, which is separated from the large group of unblocked nanoholes at the higher intensity region. The number of the blocked nanoholes is nine shown by the histogram, which is equal to the difference between the total number (156) and the unblocked values (147), indicated by the black arrows, shown in the Results area of Figure 5-6 (a). It can be seen that the blocked and unblocked nanohole groups can be well separated in the histogram for this type of darkfield image with good quality. Thus, the consequence of the calculation is really precise.

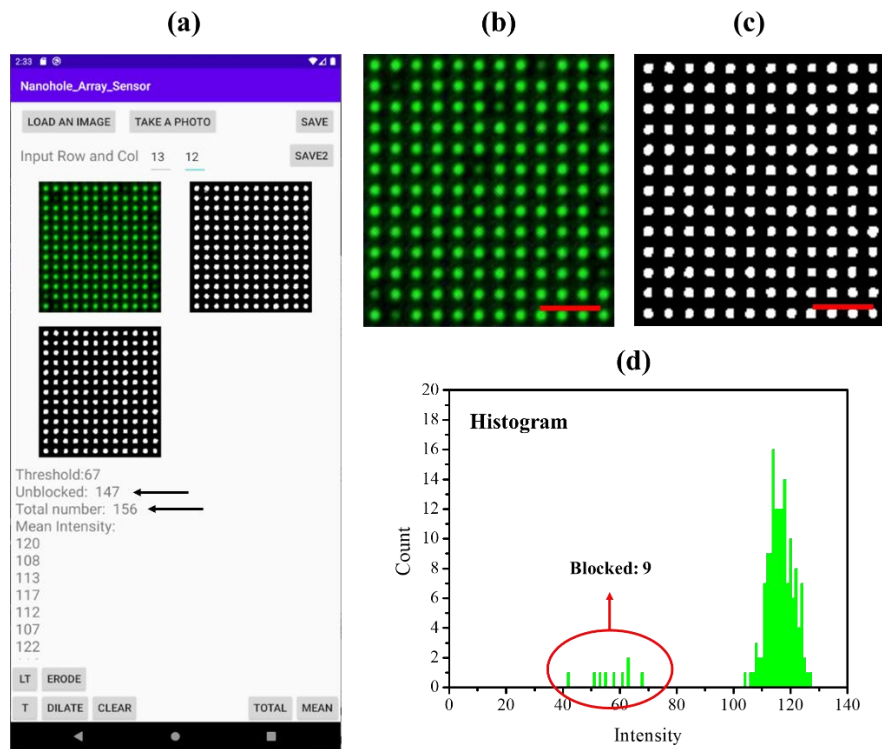


Figure 5-6 (a) Example of the darkfield image analyzed by the smartphone application, (b) the darkfield image by microscope, (c) its threshold image, and (d) intensity histogram of the nanoholes. The scale bars are both 6 μm .

Figure 5-7 (a) shows an example of the blocked nanohole array analyzed by direct counting. The original darkfield image, shown in Figure 5-7 (b), is taken by the smartphone with the home-made inexpensive darkfield microscope. The binary image, shown in Figure 5-7 (c), is obtained by the global threshold method from the original darkfield image. And the binary image, shown in Figure 5-7 (d), is obtained by one-time erosion operation from the binary image shown in Figure 5-7 (c). Then, the total number of the nanoholes that exists in Figure 5-7 (d) is calculated by performing either the MEAN function or the TOTAL function. The value of the total number is displayed in the Results area of Figure 5-7 (a), indicated by the black arrow, while the value of the unblocked is useless. Thus, it means that the number of unblocked nanoholes is 460. Since the nanohole array has 529 nanoholes in total, the number of the blocked nanoholes is 69 by subtracting 460 from 529. Figure 5-7 (e) shows the darkfield image taken by the CCD with a professional darkfield microscope. By visual inspection, the number of blocked nanoholes, which have an obvious color change, is about 69, which is equal to the number calculated above. However, comparing Figure 5-7 (d) and 4-7 (e), several blocked nanoholes are not in the same positions. This means the method still has some error in detecting the truly blocked nanoholes and some of the unblocked nanoholes with a lower intensity than others have been regarded as the blocked nanoholes. Thus, to improve the performance of the smartphone application, efforts are still needed to improve the uniformity of the nanoholes, the quality of the imaging, and the strategy for analyzing the image.

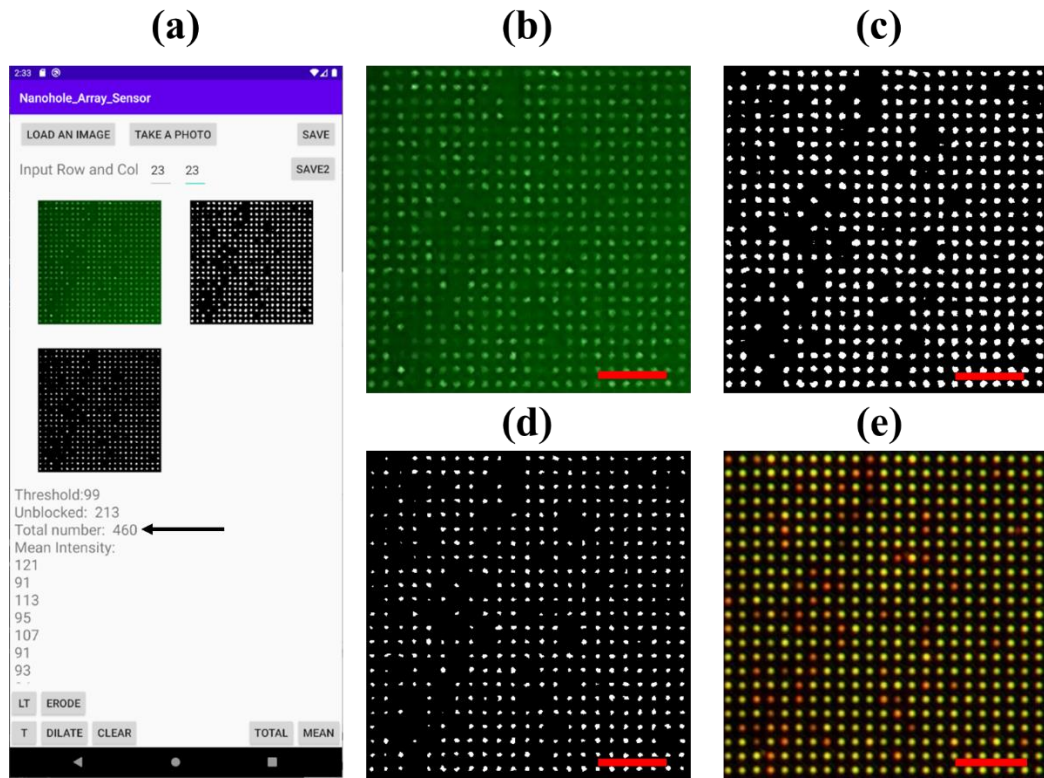


Figure 5-7 (a) Example of the darkfield image analyzed by the smartphone application, (b) the darkfield image by smartphone, (c) and (d) threshold images, and (e) the darkfield image by CCD. The scale bars are all 10 μm .

5.3 Conclusions

In this chapter, the beta version of the smartphone application, called Nanohole_Array_Sensor, which is developed for detecting the blocked nanoholes in the nanohole array samples, is introduced. The main functions of the smartphone application include two threshold methods based on Otsu's method, erosion and dilation operations of the binary image, and two methods for the intensity analysis of the nanoholes. The combinations of these functions can perform the analysis of the sample images. According to the different features of the images, choosing a suitable strategy to analyze the image

can achieve good results. Several images have been processed by the smartphone application to test these functions. In some cases, the number of blocked nanoholes is calculated precisely while in other cases there are still small errors. Generally, the results show that the smartphone application works well to a certain degree, but there is still a lot to be improved. As the experiment progresses and the requirements increase, more desired functions can be added to the smartphone application in the future.

Chapter 6 Conclusions and Perspectives

In a word, we have successfully demonstrated that the individual silica-shelled gold nanoparticles of about 110 nm size can be easily detected and analyzed with the help of the gold nanohole arrays by using a home-made darkfield imaging system coupled with a smartphone. This offers the feasibility to achieve single virus detection by the inexpensive and portable device for the future POC diagnostics, which will much benefit the healthcare in remote areas and resource-limited regions.

First of all, the fabrication methods of the nanohole arrays are introduced in chapter 2. Two techniques, e-beam lithography and nanoimprint lithography, are studied to manufacture uniform and high-quality nanohole arrays for small scale and large scale production, respectively. Various factors that will affect the performance of the samples have been investigated. The desired configuration of the nanohole arrays including the nanohole diameter and array period can be well controlled by choosing proper processing parameters. As the results, the square-lattice nanohole arrays of 150 nm diameter, 2 μm period, and 100 nm thickness have been fabricated. Both techniques can work well and produce good samples except that for the thermoplastic nanoimprint lithography there is a little distortion of the nanohole shape due to the mismatch of the thermal expansions of the Si mold and glass substrate. To solve this problem thoroughly, either the UV nanoimprint lithography or the glass mold can be used in future work.

In chapter 3, the darkfield imaging system has been utilized to acquire images of the nanohole array samples that have been blocked by the silica-shelled gold nanosphere. The individual nanoholes can be recognized readily by eyes from the darkfield images. The spectra of the individual blocked and unblocked nanoholes have also been measured by the spectrometer. The color analysis of the darkfield images and the spectra analysis of the visible light range show a pronounced reduction of light intensity in the blue and green regions but an unusual enhancement in the red region. These interesting phenomena have been confirmed as well by using the monochromatic exciting light. Additionally, a home-made inexpensive darkfield microscope imaging system coupled with a smartphone has been established, which is a prototype of the portable and inexpensive device enabling the possibility for future POC diagnostics of the individual nanometer-sized viruses. An area as large as 80×80 nanohole arrays can be clearly detected so far. The configuration and the volume of this sensing system need to be optimized in future work.

Furthermore, the simulations have been conducted to provide more information about the intensity reduction and enhancement of the transmission spectra at different wavelength regions in chapter 4. The size of the silica-shelled gold nanospheres and the position of the nanosphere inside the nanohole have been changed to obtain the trends of the size-dependent and position-dependent light intensity change. The results show that the size variation has a much larger influence than the position variation. The blue and green light intensity decrease with the increase of the nanosphere size monotonically. While the enhancement of the red light intensity can reach the maximum when the gold core size is

about 70 nm, which is just the size we have used. This implies that the combination of the nanohole size and nanosphere size induces an SPR enhancement of the red light. On the other hand, the simulated spectra of the intensity ratios between the blocked and unblocked nanoholes at different wavelengths agree well with the experimental results in the previous part. The green light between the 520 nm and 550 nm can have the maximum reduction, about 50%, of the transmitted light intensity.

Finally, we have developed a smartphone application to analyze the images obtained by the home-made inexpensive darkfield microscope imaging system. It provides two methods to threshold the darkfield images into binary images and two strategies to calculate the number of blocked nanoholes. As so far, it can work well for most of the darkfield images we obtained by choosing the proper options. In future work, more experimental samples combined with the biomedical experiments need to be tested by this home-made imaging and analysis system. At that time, the system can be further adjusted and optimized to achieve the final goal for portable, reliable, fast, and inexpensive POC diagnostics.

References

- [1] Ebbesen, T. W., Lezec, H. J., Ghaemi, H., Thio, T. & Wolff, P. A. Extraordinary optical transmission through sub-wavelength hole arrays. *Nature* **391**, 667-669 (1998).
- [2] Bethe, H. A. Theory of Diffraction by Small Holes. *Physical Review* **66**, 163-182 (1944).
- [3] Prasad, A., Choi, J., Jia, Z., Park, S. & Gartia, M. R. Nanohole array plasmonic biosensors: Emerging point-of-care applications. *Biosens Bioelectron* **130**, 185-203 (2019).
- [4] Degiron, A., Lezec, H. J., Yamamoto, N. & Ebbesen, T. W. Optical transmission properties of a single subwavelength aperture in a real metal. *Optics Communications* **239**, 61-66 (2004).
- [5] Prikulis, J., Hanarp, P., Olofsson, L., Sutherland, D. & Käll, M. Optical Spectroscopy of Nanometric Holes in Thin Gold Films. *Nano Letters* **4**, 1003-1007 (2004).
- [6] Park, T. H., Mirin, N., Lassiter, J. B., Nehl, C. L., Halas, N. J. & Nordlander, P. Optical properties of a nanosized hole in a thin metallic film. *ACS Nano* **2**, 25-32 (2008).

- [7] Gao, H., Henzie, J. & Odom, T. W. Direct evidence for surface plasmon-mediated enhanced light transmission through metallic nanohole arrays. *Nano Lett* **6**, 2104-2108 (2006).
- [8] Jahr, N., Anwar, M., Stranik, O., Hädrich, N., Vogler, N., Csaki, A., Popp, J. & Fritzsche, W. Spectroscopy on Single Metallic Nanoparticles Using Subwavelength Apertures. *The Journal of Physical Chemistry C* **117**, 7751-7756 (2013).
- [9] Lumdee, C. & Kik, P. G. Omnidirectional excitation of sidewall gap-plasmons in a hybrid gold-nanoparticle/aluminum-nanopore structure. *APL Photonics* **1**, 031301 (2016).
- [10] Seiler, S. T., Rich, I. S. & Lindquist, N. C. Direct spectral imaging of plasmonic nanohole arrays for real-time sensing. *Nanotechnology* **27**, 184001 (2016).
- [11] Cheng, F., Gao, J., Luk, T. S. & Yang, X. Structural color printing based on plasmonic metasurfaces of perfect light absorption. *Sci Rep* **5**, 11045 (2015).
- [12] Baca, A. J., Truong, T. T., Cambrea, L. R., Montgomery, J. M., Gray, S. K., Abdula, D., Banks, T. R., Yao, J., Nuzzo, R. G. & Rogers, J. A. Molded plasmonic crystals for detecting and spatially imaging surface bound species by surface-enhanced Raman scattering. *Applied Physics Letters* **94**, 243109 (2009).
- [13] Yanik, A. A., Cetin, A. E., Huang, M., Artar, A., Mousavi, S. H., Khanikaev, A., Connor, J. H., Shvets, G. & Altug, H. Seeing protein monolayers with naked eye through plasmonic Fano resonances. *Proc Natl Acad Sci U S A* **108**, 11784-11789 (2011).

- [14] Lee, S. Y., Kim, S. H., Jang, S. G., Heo, C. J., Shim, J. W. & Yang, S. M. High-fidelity optofluidic on-chip sensors using well-defined gold nanowell crystals. *Anal Chem* **83**, 9174-9180 (2011).
- [15] Gartia, M. R., Hsiao, A., Pokhriyal, A., Seo, S., Kulsharova, G., Cunningham, B. T., Bond, T. C. & Liu, G. L. Colorimetric Plasmon Resonance Imaging Using Nano Lycurgus Cup Arrays. *Advanced Optical Materials* **1**, 68-76 (2013).
- [16] Stewart, M. E., Mack, N. H., Malyarchuk, V., Soares, J. A., Lee, T. W., Gray, S. K., Nuzzo, R. G. & Rogers, J. A. Quantitative multispectral biosensing and 1D imaging using quasi-3D plasmonic crystals. *Proc Natl Acad Sci U S A* **103**, 17143-17148 (2006).
- [17] Ohno, T., Wadell, C., Inagaki, S., Shi, J., Nakamura, Y., Matsushita, S. & Sannomiya, T. Hole-size tuning and sensing performance of hexagonal plasmonic nanohole arrays. *Optical Materials Express* **6**, 1594 (2016).
- [18] Chen, Z., Li, P., Zhang, S., Chen, Y., Liu, P. & Duan, H. Enhanced extraordinary optical transmission and refractive-index sensing sensitivity in tapered plasmonic nanohole arrays. *Nanotechnology* **30**, 335201 (2019).
- [19] Najiminaini, M., Vasefi, F., Kaminska, B. & Carson, J. J. Optical resonance transmission properties of nano-hole arrays in a gold film: effect of adhesion layer. *Opt Express* **19**, 26186-26197 (2011).
- [20] Inoue, D., Miura, A., Nomura, T., Fujikawa, H., Sato, K., Ikeda, N., Tsuya, D., Sugimoto, Y. & Koide, Y. Polarization independent visible color filter comprising

- an aluminum film with surface-plasmon enhanced transmission through a subwavelength array of holes. *Applied Physics Letters* **98**, 093113 (2011).
- [21] Ghaemi, H. F., Thio, T., Grupp, D. E., Ebbesen, T. W. & Lezec, H. J. Surface plasmons enhance optical transmission through subwavelength holes. *Physical Review B* **58**, 6779-6782 (1998).
- [22] Genet, C. & Ebbesen, T. W. Light in tiny holes. *Nature* **445**, 39-46 (2007).
- [23] Najiminaini, M., Vasefi, F., Kaminska, B. & Carson, J. J. Nanohole-array-based device for 2D snapshot multispectral imaging. *Sci Rep* **3**, 2589 (2013).
- [24] Zhao, Y., Mukherjee, K., Benkstein, K. D., Sun, L., Steffens, K. L., Montgomery, C. B., Guo, S., Semancik, S. & Zaghoul, M. E. Miniaturized nanohole array based plasmonic sensor for the detection of acetone and ethanol with insights into the kinetics of adsorptive plasmonic sensing. *Nanoscale* **11**, 11922-11932 (2019).
- [25] Nakamoto, K., Kurita, R. & Niwa, O. Electrochemical surface plasmon resonance measurement based on gold nanohole array fabricated by nanoimprinting technique. *Analytical chemistry* **84**, 3187-3191 (2012).
- [26] Vala, M., Ertsgaard, C. T., Wittenberg, N. J. & Oh, S.-H. Plasmonic Sensing on Symmetric Nanohole Arrays Supporting High-Q Hybrid Modes and Reflection Geometry. *ACS sensors* **4**, 3265-3274 (2019).
- [27] Sharpe, J. C., Mitchell, J. S., Lin, L., Sedoglavich, N. & Blaikie, R. J. Gold nanohole array substrates as immunobiosensors. *Anal Chem* **80**, 2244-2249 (2008).

- [28] Sannomiya, T., Scholder, O., Jefimovs, K., Hafner, C. & Dahlin, A. B. Investigation of plasmon resonances in metal films with nanohole arrays for biosensing applications. *Small* **7**, 1653-1663 (2011).
- [29] Im, H., Shao, H., Park, Y. I., Peterson, V. M., Castro, C. M., Weissleder, R. & Lee, H. Label-free detection and molecular profiling of exosomes with a nanoplasmonic sensor. *Nat Biotechnol* **32**, 490-495 (2014).
- [30] Valsecchi, C., Gomez Armas, L. E. & Weber de Menezes, J. Large Area Nanohole Arrays for Sensing Fabricated by Interference Lithography. *Sensors (Basel)* **19** (2019).
- [31] Chang, T. Y., Huang, M., Yanik, A. A., Tsai, H. Y., Shi, P., Aksu, S., Yanik, M. F. & Altug, H. Large-scale plasmonic microarrays for label-free high-throughput screening. *Lab Chip* **11**, 3596-3602 (2011).
- [32] Monteiro, J. P., de Oliveira, J. H., Radovanovic, E., Brolo, A. G. & Girotto, E. M. Microfluidic Plasmonic Biosensor for Breast Cancer Antigen Detection. *Plasmonics* **11**, 45-51 (2015).
- [33] Soler, M., Belushkin, A., Cavallini, A., Kebbi-Beghdadi, C., Greub, G. & Altug, H. Multiplexed nanoplasmonic biosensor for one-step simultaneous detection of *Chlamydia trachomatis* and *Neisseria gonorrhoeae* in urine. *Biosens Bioelectron* **94**, 560-567 (2017).
- [34] Sinton, D., Gordon, R. & Brolo, A. G. Nanohole arrays in metal films as optofluidic elements: progress and potential. *Microfluidics and Nanofluidics* **4**, 107-116 (2007).

- [35] Li, X., Soler, M., Ozdemir, C. I., Belushkin, A., Yesilkoy, F. & Altug, H. Plasmonic nanohole array biosensor for label-free and real-time analysis of live cell secretion. *Lab Chip* **17**, 2208-2217 (2017).
- [36] Cetin, A. E., Etezadi, D., Galarreta, B. C., Busson, M. P., Eksioglu, Y. & Altug, H. Plasmonic Nanohole Arrays on a Robust Hybrid Substrate for Highly Sensitive Label-Free Biosensing. *ACS Photonics* **2**, 1167-1174 (2015).
- [37] Cetin, A. E., Coskun, A. F., Galarreta, B. C., Huang, M., Herman, D., Ozcan, A. & Altug, H. Handheld high-throughput plasmonic biosensor using computational on-chip imaging. *Light: Science & Applications* **3**, e122-e122 (2014).
- [38] Lesuffleur, A., Im, H., Lindquist, N. C., Lim, K. S. & Oh, S.-H. Laser-illuminated nanohole arrays for multiplex plasmonic microarray sensing. *Optics express* **16**, 219-224 (2008).
- [39] Escobedo, C., Vincent, S., Choudhury, A. I. K., Campbell, J., Brolo, A. G., Sinton, D. & Gordon, R. Integrated nanohole array surface plasmon resonance sensing device using a dual-wavelength source. *Journal of Micromechanics and Microengineering* **21**, 115001 (2011).
- [40] Yang, J. C., Ji, J., Hogle, J. M. & Larson, D. N. Multiplexed plasmonic sensing based on small-dimension nanohole arrays and intensity interrogation. *Biosens Bioelectron* **24**, 2334-2338 (2009).

- [41] Im, H., Lesuffleur, A., Lindquist, N. C. & Oh, S. H. Plasmonic nanoholes in a multichannel microarray format for parallel kinetic assays and differential sensing. *Anal Chem* **81**, 2854-2859 (2009).
- [42] Ji, J., O'Connell, J. G., Carter, D. J. & Larson, D. N. High-throughput nanohole array based system to monitor multiple binding events in real time. *Analytical chemistry* **80**, 2491-2498 (2008).
- [43] Lindquist, N. C., Lesuffleur, A., Im, H. & Oh, S. H. Sub-micron resolution surface plasmon resonance imaging enabled by nanohole arrays with surrounding Bragg mirrors for enhanced sensitivity and isolation. *Lab Chip* **9**, 382-387 (2009).
- [44] Tetz, K. A., Pang, L. & Fainman, Y. High-resolution surface plasmon resonance sensor based on linewidth-optimized nanohole array transmittance. *Opt Lett* **31**, 1528-1530 (2006).
- [45] Lesuffleur, A., Im, H., Lindquist, N. C. & Oh, S.-H. Periodic nanohole arrays with shape-enhanced plasmon resonance as real-time biosensors. *Applied Physics Letters* **90**, 243110 (2007).
- [46] Hwang, G. M., Pang, L., Mullen, E. H. & Fainman, Y. Plasmonic Sensing of Biological Analytes Through Nanoholes. *IEEE Sensors Journal* **8**, 2074-2079 (2008).
- [47] Lee, S. H., Lindquist, N. C., Wittenberg, N. J., Jordan, L. R. & Oh, S. H. Real-time full-spectral imaging and affinity measurements from 50 microfluidic channels using nanohole surface plasmon resonance. *Lab Chip* **12**, 3882-3890 (2012).

- [48] Belushkin, A., Yesilkoy, F. & Altug, H. Nanoparticle-enhanced plasmonic biosensor for digital biomarker detection in a microarray. *ACS nano* **12**, 4453-4461 (2018).
- [49] Belushkin, A., Yesilkoy, F., González-López, J. J., Ruiz-Rodríguez, J. C., Ferrer, R., Fàbrega, A. & Altug, H. Rapid and digital detection of inflammatory biomarkers enabled by a novel portable nanoplasmonic imager. *Small* **16**, 1906108 (2020).
- [50] Nakamoto, K., Kurita, R., Niwa, O., Fujii, T. & Nishida, M. Development of a mass-producible on-chip plasmonic nanohole array biosensor. *Nanoscale* **3**, 5067-5075 (2011).
- [51] Yanik, A. A., Huang, M., Kamohara, O., Artar, A., Geisbert, T. W., Connor, J. H. & Altug, H. An optofluidic nanoplasmonic biosensor for direct detection of live viruses from biological media. *Nano Lett* **10**, 4962-4969 (2010).
- [52] Im, H., Wittenberg, N. J., Lesuffleur, A., Lindquist, N. C. & Oh, S. H. Membrane protein biosensing with plasmonic nanopore arrays and pore-spanning lipid membranes. *Chem Sci* **1**, 688-696 (2010).
- [53] Gomez-Cruz, J., Nair, S., Manjarrez-Hernandez, A., Gavilanes-Parra, S., Ascanio, G. & Escobedo, C. Cost-effective flow-through nanohole array-based biosensing platform for the label-free detection of uropathogenic *E. coli* in real time. *Biosens Bioelectron* **106**, 105-110 (2018).

- [54] Brolo, A. G., Gordon, R., Leathem, B. & Kavanagh, K. L. Surface plasmon sensor based on the enhanced light transmission through arrays of nanoholes in gold films. *Langmuir* **20**, 4813-4815 (2004).
- [55] Fu, Y., Ngoi, B. K. A., Zhou, W. E. I. & Loh, T. F. Direct Formation of Nanopore Array Via Focused Ion Beam Fine Milling and Surface Coating Techniques. *International Journal of Nanoscience* **05**, 529-534 (2011).
- [56] Yang, J. C., Ji, J., Hogle, J. M. & Larson, D. N. Metallic nanohole arrays on fluoropolymer substrates as small label-free real-time bioprobes. *Nano Lett* **8**, 2718-2724 (2008).
- [57] Eftekhari, F., Escobedo, C., Ferreira, J., Duan, X., Girotto, E. M., Brolo, A. G., Gordon, R. & Sinton, D. Nanoholes as nanochannels: flow-through plasmonic sensing. *Anal Chem* **81**, 4308-4311 (2009).
- [58] De Leebeeck, A., Kumar, L. K., de Lange, V., Sinton, D., Gordon, R. & Brolo, A. G. On-chip surface-based detection with nanohole arrays. *Anal Chem* **79**, 4094-4100 (2007).
- [59] Blanchard-Dionne, A., Guyot, L., Patskovsky, S., Gordon, R. & Meunier, M. Intensity based surface plasmon resonance sensor using a nanohole rectangular array. *Optics express* **19**, 15041-15046 (2011).
- [60] Yanik, A. A., Huang, M., Artar, A., Chang, T.-Y. & Altug, H. Integrated nanoplasmonic-nanofluidic biosensors with targeted delivery of analytes. *Applied Physics Letters* **96**, 021101 (2010).

- [61] Lee, K. L., Wu, S. H. & Wei, P. K. Intensity sensitivity of gold nanostructures and its application for high-throughput biosensing. *Opt Express* **17**, 23104-23113 (2009).
- [62] Sandison, M. E. & Cooper, J. M. Nanofabrication of electrode arrays by electron-beam and nanoimprint lithographies. *Lab Chip* **6**, 1020-1025 (2006).
- [63] Nakamoto, K., Kurita, R. & Niwa, O. Electrochemical surface plasmon resonance measurement based on gold nanohole array fabricated by nanoimprinting technique. *Anal Chem* **84**, 3187-3191 (2012).
- [64] Malyarchuk, V., Hua, F., Mack, N., Velasquez, V., White, J., Nuzzo, R. & Rogers, J. High performance plasmonic crystal sensor formed by soft nanoimprint lithography. *Opt Express* **13**, 5669-5675 (2005).
- [65] Guo, L. J. Nanoimprint Lithography: Methods and Material Requirements. *Advanced Materials* **19**, 495-513 (2007).
- [66] Murray-Methot, M. P., Menegazzo, N. & Masson, J. F. Analytical and physical optimization of nanohole-array sensors prepared by modified nanosphere lithography. *Analyst* **133**, 1714-1721 (2008).
- [67] Park, H. K., Moon, J. H., Yoon, S. & Rag Do, Y. Fabrication of Micro-Patterned 2D Nanorod and Nanohole Arrays by a Combination of Photolithography and Nanosphere Lithography. *Journal of The Electrochemical Society* **158**, J143 (2011).
- [68] Masson, J. F., Murray-Methot, M. P. & Live, L. S. Nanohole arrays in chemical analysis: manufacturing methods and applications. *Analyst* **135**, 1483-1489 (2010).

- [69] Ai, B., Yu, Y., Mohwald, H., Zhang, G. & Yang, B. Plasmonic films based on colloidal lithography. *Adv Colloid Interface Sci* **206**, 5-16 (2014).
- [70] Larson, S., Carlson, D., Ai, B. & Zhao, Y. The extraordinary optical transmission and sensing properties of Ag/Ti composite nanohole arrays. *Physical Chemistry Chemical Physics* **21**, 3771-3780 (2019).
- [71] Santos, E. B., Valsecchi, C., Gonçalves, J. L., Ávila, L. F. & Menezes, J. W. Coupling Single-Drop Microextraction with SERS: A Demonstration Using p-MBA on Gold Nanohole Array Substrate. *Sensors* **19**, 4394 (2019).
- [72] Armas, L. E. G., Menezes, J. W., Huila, M. G., Araki, K. & Toma, H. E. Gold Nanohole Arrays Fabricated by Interference Lithography Technique as SERS Probes for Chemical Species Such As Rhodamine 6G and 4,4'-Bipyridine. *Plasmonics* **12**, 1015-1020 (2016).
- [73] Weber de Menezes, J., Thesing, A., Valsecchi, C., Armas, L. E. & Brolo, A. G. Improving the performance of gold nanohole array biosensors by controlling the optical collimation conditions. *Appl Opt* **54**, 6502-6507 (2015).
- [74] Menezes, J. W., Ferreira, J., Santos, M. J. L., Cescato, L. & Brolo, A. G. Large-Area Fabrication of Periodic Arrays of Nanoholes in Metal Films and Their Application in Biosensing and Plasmonic-Enhanced Photovoltaics. *Advanced Functional Materials* **20**, 3918-3924 (2010).

- [75] Du, K., Wathuthanthri, I., Mao, W., Xu, W. & Choi, C. H. Large-area pattern transfer of metallic nanostructures on glass substrates via interference lithography. *Nanotechnology* **22**, 285306 (2011).
- [76] Henzie, J., Lee, M. H. & Odom, T. W. Multiscale patterning of plasmonic metamaterials. *Nat Nanotechnol* **2**, 549-554 (2007).
- [77] Wang, Y., Kar, A., Paterson, A., Kourentzi, K., Le, H., Ruchhoeft, P., Willson, R. & Bao, J. Transmissive Nanohole Arrays for Massively-Parallel Optical Biosensing. *ACS Photonics* **1**, 241-245 (2014).
- [78] Taflove, A. & Hagness, S. C. Computational electromagnetics: the finite-difference time-domain method. *Artech House, Boston*, 149-161 (1995).
- [79] Yee, K. Numerical solution of initial boundary value problems involving Maxwell's equations in isotropic media. *IEEE Transactions on antennas and propagation* **14**, 302-307 (1966).
- [80] Shlager, K. L. A survey of the finite-difference time-domain literature. *Advance in computational Electrodynamics: The Finite-Difference Time-Domain Method* (1998).
- [81] Taflove, A. & Brodwin, M. E. Numerical solution of steady-state electromagnetic scattering problems using the time-dependent Maxwell's equations. *IEEE transactions on microwave theory and techniques* **23**, 623-630 (1975).

- [82] Ludwig, S. K., Tokarski, C., Lang, S. N., van Ginkel, L. A., Zhu, H., Ozcan, A. & Nielen, M. W. Calling Biomarkers in Milk Using a Protein Microarray on Your Smartphone. *PLoS One* **10**, e0134360 (2015).
- [83] Coskun, A. F., Wong, J., Khodadadi, D., Nagi, R., Tey, A. & Ozcan, A. A personalized food allergen testing platform on a cellphone. *Lab Chip* **13**, 636-640 (2013).
- [84] Song, C., Zhao, Z., Lin, Y., Zhao, Y., Liu, X. Y., Lin, C. & Wu, C. A nanoneedle-based reactional wettability variation sensor array for on-site detection of metal ions with a smartphone. *J Colloid Interface Sci* **547**, 330-338 (2019).
- [85] Wei, Q., Nagi, R., Sadeghi, K., Feng, S., Yan, E., Ki, S. J., Caire, R., Tseng, D. & Ozcan, A. Detection and spatial mapping of mercury contamination in water samples using a smart-phone. *ACS Nano* **8**, 1121-1129 (2014).
- [86] Topol, E. J. Transforming medicine via digital innovation. *Sci Transl Med* **2**, 16cm14 (2010).
- [87] Chen, H., Li, Z., Zhang, L., Sawaya, P., Shi, J. & Wang, P. Quantitation of Femtomolar-Level Protein Biomarkers Using a Simple Microbubbling Digital Assay and Bright-Field Smartphone Imaging. *Angew Chem Int Ed Engl* **58**, 13922-13928 (2019).
- [88] Ozcan, A. Mobile phones democratize and cultivate next-generation imaging, diagnostics and measurement tools. *Lab Chip* **14**, 3187-3194 (2014).

- [89] Ong, D. S. Y. & Poljak, M. Smartphones as mobile microbiological laboratories. *Clin Microbiol Infect* **26**, 421-424 (2020).
- [90] Huang, X., Xu, D., Chen, J., Liu, J., Li, Y., Song, J., Ma, X. & Guo, J. Smartphone-based analytical biosensors. *Analyst* **143**, 5339-5351 (2018).
- [91] Coskun, A. F. & Ozcan, A. Computational imaging, sensing and diagnostics for global health applications. *Curr Opin Biotechnol* **25**, 8-16 (2014).
- [92] Li, F., Zheng, Y., Wu, J., Zhao, L., Shui, L., Pu, Q. & Liu, S. Smartphone assisted immunodetection of HIV p24 antigen using reusable, centrifugal microchannel array chip. *Talanta* **203**, 83-89 (2019).
- [93] Prasad, A., Hasan, S. M. A., Grouchy, S. & Gartia, M. R. DNA microarray analysis using a smartphone to detect the BRCA-1 gene. *Analyst* **144**, 197-205 (2018).
- [94] Wang, L. J., Sun, R., Vasile, T., Chang, Y. C. & Li, L. High-Throughput Optical Sensing Immunoassays on Smartphone. *Anal Chem* **88**, 8302-8308 (2016).
- [95] Lee, S. A. & Yang, C. A smartphone-based chip-scale microscope using ambient illumination. *Lab Chip* **14**, 3056-3063 (2014).
- [96] Berg, B., Cortazar, B., Tseng, D., Ozkan, H., Feng, S., Wei, Q., Chan, R. Y., Burbano, J., Farooqui, Q., Lewinski, M., Di Carlo, D., Garner, O. B. & Ozcan, A. Cellphone-Based Hand-Held Microplate Reader for Point-of-Care Testing of Enzyme-Linked Immunosorbent Assays. *ACS Nano* **9**, 7857-7866 (2015).

- [97] Dutta, S., Saikia, G. P., Sarma, D. J., Gupta, K., Das, P. & Nath, P. Protein, enzyme and carbohydrate quantification using smartphone through colorimetric digitization technique. *J Biophotonics* **10**, 623-633 (2017).
- [98] Ra, M., Muhammad, M. S., Lim, C., Han, S., Jung, C. & Kim, W. Y. Smartphone-Based Point-of-Care Urinalysis Under Variable Illumination. *IEEE J Transl Eng Health Med* **6**, 2800111 (2018).
- [99] He, X., Pei, Q., Xu, T. & Zhang, X. Smartphone-based tape sensors for multiplexed rapid urinalysis. *Sensors and Actuators B: Chemical* **304**, 127415 (2020).
- [100] Gahlaut, S. K., Kalyani, N., Sharan, C., Mishra, P. & Singh, J. P. Smartphone based dual mode in situ detection of viability of bacteria using Ag nanorods array. *Biosens Bioelectron* **126**, 478-484 (2019).
- [101] Wang, F., Lu, Y., Yang, J., Chen, Y., Jing, W., He, L. & Liu, Y. A smartphone readable colorimetric sensing platform for rapid multiple protein detection. *Analyst* **142**, 3177-3182 (2017).
- [102] Wei, Q., Qi, H., Luo, W., Tseng, D., Ki, S. J., Wan, Z., Gorocs, Z., Bentolila, L. A., Wu, T. T., Sun, R. & Ozcan, A. Fluorescent imaging of single nanoparticles and viruses on a smart phone. *ACS Nano* **7**, 9147-9155 (2013).
- [103] Lu, M. Y., Kao, W. C., Belkin, S. & Cheng, J. Y. A Smartphone-Based Whole-Cell Array Sensor for Detection of Antibiotics in Milk. *Sensors (Basel)* **19** (2019).

- [104] Hu, X., Shi, J., Shi, Y., Zou, X., Arslan, M., Zhang, W., Huang, X., Li, Z. & Xu, Y. Use of a smartphone for visual detection of melamine in milk based on Au@Carbon quantum dots nanocomposites. *Food Chem* **272**, 58-65 (2019).
- [105] Arafat Hossain, M., Canning, J., Ast, S., Cook, K., Rutledge, P. J. & Jamalipour, A. Combined "dual" absorption and fluorescence smartphone spectrometers. *Opt Lett* **40**, 1737-1740 (2015).
- [106] Wang, L. J., Chang, Y. C., Sun, R. & Li, L. A multichannel smartphone optical biosensor for high-throughput point-of-care diagnostics. *Biosens Bioelectron* **87**, 686-692 (2017).
- [107] Long, K. D., Woodburn, E. V., Le, H. M., Shah, U. K., Lumetta, S. S. & Cunningham, B. T. Multimode smartphone biosensing: the transmission, reflection, and intensity spectral (TRI)-analyzer. *Lab Chip* **17**, 3246-3257 (2017).
- [108] Yu, H., Tan, Y. & Cunningham, B. T. Smartphone fluorescence spectroscopy. *Anal Chem* **86**, 8805-8813 (2014).
- [109] Pan, M. Y., Lee, K. L., Lo, S. C. & Wei, P. K. Resonant position tracking method for smartphone-based surface plasmon sensor. *Anal Chim Acta* **1032**, 99-106 (2018).
- [110] Fan, Z., Geng, Z., Fang, W., Lv, X., Su, Y., Wang, S. & Chen, H. Smartphone Biosensor System with Multi-Testing Unit Based on Localized Surface Plasmon Resonance Integrated with Microfluidics Chip. *Sensors (Basel)* **20** (2020).
- [111] Lertvachirapaiboon, C., Baba, A., Shinbo, K. & Kato, K. A smartphone-based surface plasmon resonance platform. *Analytical Methods* **10**, 4732-4740 (2018).

- [112] Otsu, N. A threshold selection method from gray-level histograms. *IEEE transactions on systems, man, and cybernetics* **9**, 62-66 (1979).

Appendices

A. The analysis script of the simulation

The script used to derive the far field data from the near field data is shown below.

```
# User Settings

NA = 1;      # choose NA of imaging optics

mname = "T";    # monitor recording the data

res = 401;     # res controls the number of plane waves, used for decomposition, which is (res x res)

z0 = 0e-6;     # defocus

# get simulation frequency

f = getdata(mname,"f");    # frequency of monitor

x = getdata(mname,"x");

y = getdata(mname,"y");

lambda = c/f;      # wavelength

k = 2*pi/lambda;   # k

# decompose nearfield into plane waves using farfield projection

E = farfieldvector3d(mname,1,res,res);

Ex = pinch(E,3,1);

Ey = pinch(E,3,2);

Ez = pinch(E,3,3);

ux = farfieldux(mname,1,res,res);
```

```

uy = farfielduy(mname,l,res,res);

Ux = meshgridx(ux,uy);

Uy = meshgridy(ux,uy);

Uz = real(sqrt(1-(Ux^2+Uy^2))) + 1e-5;

# filter for propagating waves through aperture

filter = real(sqrt(Ux^2 + Uy^2)) < NA;

Ex = filter*Ex;

Ey = filter*Ey;

Ez = filter*Ez;

# define image plane

x_image = linspace(min(x),max(x),res);

y_image = linspace(min(y),max(y),res);

# calculate the image, using chirped z-transform

kx = ux*k;

ky = uy*k;

dkx = kx(2)-kx(1);

dky = ky(2)-ky(1);

Kz = Uz*k;

Ex_image = czt(Ex*exp(1i*Kz*z0)*sqrt(1/Uz/k^2), kx, ky, x_image, y_image)*dkx*dky/(2*pi);

Ey_image = czt(Ey*exp(1i*Kz*z0)*sqrt(1/Uz/k^2), kx, ky, x_image, y_image)*dkx*dky/(2*pi);

Ez_image = czt(Ez*exp(1i*Kz*z0)*sqrt(1/Uz/k^2), kx, ky, x_image, y_image)*dkx*dky/(2*pi);

```

```

# calculate |E|^2 at the image plane

E2_image = abs(Ex_image)^2 + abs(Ey_image)^2 + abs(Ez_image)^2;

# plot fields at image plane

image(x_image*1e6, y_image*1e6, E2_image, "x (um)", "y (um)", "Microscopy imaging");

# plot fields in near field

image(x*1e6, y*1e6, getelectric(mname), "x (um)", "y (um)", "Near field");

# show ratio of near field and imaging

E2 = getelectric("T");

a = amax(pinch(E2),2);

max1 = max(a(50:200,1));

max2 = max(a(250:400,1));

?r_NF = max2/max1;

b = amax(E2_image,2);

max11 = max(b(50:150,1));

max22 = max(b(250:350,1));

?r_imaging = max22/max11;

```

B. The smartphone application codes

The main java and xml files of the smartphone application are shown below.

i. MainActivity.java

```
package com.sunshine.nanohole_array_sensor;
```

```
import android.Manifest;

import android.content.Intent;

import android.content.pm.PackageManager;

import android.graphics.Bitmap;

import android.graphics.drawable.BitmapDrawable;

import android.net.Uri;

import android.os.Bundle;

import android.os.Environment;

import android.provider.MediaStore;

import android.util.Log;

import android.view.View;

import android.widget.Button;

import android.widget.EditText;

import android.widget.ImageView;

import android.widget.TextView;

import android.widget.Toast;

import androidx.appcompat.app.AppCompatActivity;

import androidx.core.app.ActivityCompat;

import androidx.core.content.ContextCompat;

import org.opencv.android.OpenCVLoader;

import java.io.File;
```

```
import java.io.FileOutputStream;

import java.io.IOException;

import java.util.Arrays;

public class MainActivity extends AppCompatActivity {

    private static String Tag = "MainActivity";

    static {

        if (OpenCVLoader.initDebug()){

            Log.d(Tag, "Good");

        }else{

            Log.d(Tag, "bad");}}

    private Button Load_an_image;

    private Button Take_a_photo;

    private Button Save;

    private Button Save2;

    private ImageView image;

    private ImageView image2;

    private ImageView image3;

    private EditText row;

    private EditText col;

    private TextView result;

    private Button total;
```

```

private Button mean;

private Button t;

private Button lt;

private Button erode;

private Button dilate;

private Button clear;

private final int LOAD_AN_IMAGE = 1;

private final int TAKE_A_PHOTO = 11;

private int saveCode = 0;

@Override

protected void onCreate(Bundle savedInstanceState) {

    super.onCreate(savedInstanceState);

    setContentView(R.layout.activity_main);

    findViewById();

    setOnClickListener();}

private void findViewById(){

    Load_an_image = findViewById(R.id.Load_an_image);

    Take_a_photo = findViewById(R.id.Take_a_photo);

    image = findViewById(R.id.image);

    image2 = findViewById(R.id.image2);

    result = findViewById(R.id.result);

```

```

row = findViewById(R.id.row);

col = findViewById(R.id.col);

Save = findViewById(R.id.Save);

total = findViewById(R.id.total);

mean = findViewById(R.id.mean);

t = findViewById(R.id.t);

It = findViewById(R.id.It);

Save2 = findViewById(R.id.Save2);

erode = findViewById(R.id.erode);

dilate = findViewById(R.id.dilate);

clear = findViewById(R.id.clear);

image3 = findViewById(R.id.image3);}

private void setOnClickListener(){

    Load_an_image.setOnClickListener(new View.OnClickListener() {

        @Override

        public void onClick(View v) {

            Intent intent = new Intent(Intent.ACTION_PICK,

MediaStore.Images.Media.EXTERNAL_CONTENT_URI);

            startActivityForResult(intent, LOAD_AN_IMAGE);});

    Take_a_photo.setOnClickListener(new View.OnClickListener() {

        @Override

```

```

public void onClick(View view) {

    Intent intent = new Intent(MediaStore.ACTION_IMAGE_CAPTURE);

    startActivityForResult(intent, TAKE_A_PHOTO)}});

Save.setOnClickListener(new View.OnClickListener() {

    @Override

    public void onClick(View view) {

        if (row.getText() != null && col.getText() != null && image.getDrawable() != null) {

            if (checkStoragePermission()) {

                saveCode = 1;

                save();}};

            } else {

                Toast.makeText(getApplicationContext(), "Please enter Row or Col! or Load a
image!", Toast.LENGTH_LONG).show();}}});

total.setOnClickListener(new View.OnClickListener() {

    @Override

    public void onClick(View v) {

        total_intensity();}});

mean.setOnClickListener(new View.OnClickListener() {

    @Override

    public void onClick(View v) {

        mean_intensity();}});

```

```

t.setOnClickListener(new View.OnClickListener() {

    @Override

    public void onClick(View v) {

        if (image.getDrawable() != null) {

            Bitmap bm = ((BitmapDrawable) image.getDrawable()).getBitmap();

            image2.setImageBitmap(Threshold.globalThreshold(bm));

            int threshold = Threshold.getT(bm);

            String text = "Threshold:  " + threshold;

            result.setText(text);

        } else {

            Toast.makeText(getApplicationContext(), "Please Load a image!",

Toast.LENGTH_LONG).show();}}});

It.setOnClickListener(new View.OnClickListener() {

    @Override

    public void onClick(View v) {

        if (image.getDrawable() != null) {

            int rowSize = Integer.parseInt(row.getText().toString());

            int colSize = Integer.parseInt(col.getText().toString());

            Bitmap bm = ((BitmapDrawable) image.getDrawable()).getBitmap();

            image2.setImageBitmap(Threshold.localThreshold(bm, rowSize, colSize));

        } else {

```

```

        Toast.makeText(getApplicationContext(), "Please Load a image!",
Toast.LENGTH_LONG).show();}}});

        Save2.setOnClickListener(new View.OnClickListener() {

            @Override

            public void onClick(View v) {

                if (checkStoragePermission()) {

                    saveCode = 2;

                    save2();}}});

        erode.setOnClickListener(new View.OnClickListener() {

            @Override

            public void onClick(View v) {

                if (image2.getDrawable() != null && image3.getDrawable() == null) {

                    Bitmap bm = ((BitmapDrawable) image2.getDrawable()).getBitmap();

                    image3.setImageBitmap(Morphology.erode(bm));

                } else if (image3.getDrawable() != null) {

                    Bitmap bm = ((BitmapDrawable) image3.getDrawable()).getBitmap();

                    image3.setImageBitmap(Morphology.erode(bm));

                } else {

                    Toast.makeText(getApplicationContext(), "Please threshold a image!",

Toast.LENGTH_LONG).show();}}});

        dilate.setOnClickListener(new View.OnClickListener() {

```

```

@Override

public void onClick(View v) {

    if (image2.getDrawable() != null && image3.getDrawable() == null) {

        Bitmap bm = ((BitmapDrawable) image2.getDrawable()).getBitmap();

        image3.setImageBitmap(Morphology.dilate(bm));

    } else if (image3.getDrawable() != null) {

        Bitmap bm = ((BitmapDrawable) image3.getDrawable()).getBitmap();

        image3.setImageBitmap(Morphology.dilate(bm));

    } else {

        Toast.makeText(getApplicationContext(), "Please threshold a image!",
Toast.LENGTH_LONG).show();});});

clear.setOnClickListener(new View.OnClickListener() {

@Override

public void onClick(View v) {

    image3.setImageDrawable(null);});});

protected void onActivityResult(int requestCode, int resultCode, Intent data){

super.onActivityResult(requestCode, resultCode, data);

if (requestCode == LOAD_AN_IMAGE && resultCode == RESULT_OK){

    Uri uri = data.getData();

    image.setImageURI(uri); }

if (requestCode == TAKE_A_PHOTO && resultCode == RESULT_OK) {

```

```

        Bundle bundle = data.getExtras();

        Bitmap bitmap = (Bitmap) bundle.get("data");

        image.setImageBitmap(bitmap);}}

private final int WRITE_EXTERNAL_STORAGE_REQUEST_CODE = 2;

private boolean checkStoragePermission() {

    if (ContextCompat.checkSelfPermission(this,

Manifest.permission.WRITE_EXTERNAL_STORAGE)

        != PackageManager.PERMISSION_GRANTED) {

        ActivityCompat.requestPermissions(this, new

String[]{Manifest.permission.WRITE_EXTERNAL_STORAGE},

            WRITE_EXTERNAL_STORAGE_REQUEST_CODE);

        return false;

    } else {

        return true;}}

@Override

public void onRequestPermissionsResult(int requestCode, String[] permissions, int[] grantResults) {

    super.onRequestPermissionsResult(requestCode, permissions, grantResults);

    if (requestCode == WRITE_EXTERNAL_STORAGE_REQUEST_CODE) {

        if (grantResults[0] == PackageManager.PERMISSION_GRANTED) {

            // Permission Granted

            if (saveCode == 1) {

```

```

        save();}

        if (saveCode == 2) {

            save2();}

        } else {

            // Permission Denied

            Toast.makeText(this, "Permission Denied", Toast.LENGTH_SHORT).show();}}

private void save() {

    String text = result.getText().toString();

    Log.i("MainActivity", Environment.getExternalStorageState());

    if(!Environment.getExternalStorageState().equals(Environment.MEDIA_MOUNTED)){

        Toast.makeText(MainActivity.this, "SDcard not found! Data save failed!",

Toast.LENGTH_SHORT).show();

        return;}

    File file = Environment.getExternalStorageDirectory();

    File myFile = new File(file, "myData.txt");

    FileOutputStream fos = null;

    try {

        fos = new FileOutputStream(myFile);

        Log.i("MainActivity", "----->");

        fos.write(text.getBytes());

        Toast.makeText(MainActivity.this, "Data saved successfully",

```

```

Toast.LENGTH_SHORT).show();

    } catch (Exception e) {

        e.printStackTrace();

        Toast.makeText(this, "Data save failed", Toast.LENGTH_SHORT).show();

    } finally{

        if(fos!=null){

            try {

                fos.close();

            } catch (IOException e) {

                e.printStackTrace();}}}}

private void total_intensity() {

    Bitmap bm;

    if (image3.getDrawable() != null) {

        bm = ((BitmapDrawable) image3.getDrawable()).getBitmap();

    } else {

        bm = ((BitmapDrawable) image2.getDrawable()).getBitmap();

    }

    Bitmap bm2 = ((BitmapDrawable) image.getDrawable()).getBitmap();

    int[] labels = Label.cc_labels(bm);

    int num = Label.cc_num(bm);

    int[] gray = Label.cc_gray(bm2);

    int[] intensity = new int[num];

```

```

for(int i = 0; i < labels.length; i++){

    intensity[labels[i]] += gray[i];}

int[] intensity1 = new int[num-1]; //remove background

int[] intensity2 = new int[num-1]; //remove background

for (int i = 0; i < num-1; i++){

    intensity1[i] = intensity[i+1]; //remove background}

Arrays.sort(intensity1); //from min to max

for (int i = 0; i < num-1; i++) {

    intensity2[i] = intensity1[num-2-i];} //from max to min

int[] t = FindTforAnyRange.OtsuThreshold(intensity2);

int unblocked = 0;

for (int i = 0; i < num-1; i++) {

    if (intensity2[i] > t[0]) {

        unblocked += 1;}}

String threshold = "Threshold:" + t[0];

String text = threshold + "\nUnblocked:  " + unblocked + "\nTotal number:  " + (num-1) +

"\nTotal Intensity:\n";

for (int i = 0; i < num-1; i++){

    text += intensity2[i] + "\n";}

result.setText(text);}

private void mean_intensity() {

```

```

Bitmap bm;

if (image3.getDrawable() != null) {

    bm = ((BitmapDrawable) image3.getDrawable()).getBitmap();

} else {

    bm = ((BitmapDrawable) image2.getDrawable()).getBitmap();

Bitmap bm2 = ((BitmapDrawable) image.getDrawable()).getBitmap();

int[] labels = Label.cc_labels(bm);

int num = Label.cc_num(bm);

int[] gray = Label.cc_gray(bm2);

int[] pixelnum = new int[num];

int[] intensity = new int[num];

for(int i = 0; i < labels.length; i++){

    intensity[labels[i]] += gray[i];

    pixelnum[labels[i]] += 1;}

int[] meanIntensity = new int[num - 1]; //remove background

for (int i = 0; i < num-1; i++){

    meanIntensity[i] = intensity[i+1]/pixelnum[i+1];} //remove background

int[] t = FindThreshold.OtsuThreshold(meanIntensity);

int unblocked = 0;

for (int i = 0; i < num-1; i++) {

    if (meanIntensity[i] > t[0]) {

```

```

        unblocked += 1;}}

String threshold = "Threshold:" + t[0];

String text = threshold + "\nUnblocked:  " + unblocked + "\nTotal number:  " + (num-1) +

"\nMean Intensity:\n";

for (int i = 0; i < num-1; i++){

    text += meanIntensity[i] + "\n";}

result.setText(text);}

private void save2() {

    Log.i("MainActivity",Environment.getExternalStorageState());

    if(!Environment.getExternalStorageState().equals(Environment.MEDIA_MOUNTED)){

        Toast.makeText(MainActivity.this, "SDcard not found! Data save failed!",

Toast.LENGTH_SHORT).show();

        return;}

    Bitmap bm;

    if (image3.getDrawable() != null) {

        bm = ((BitmapDrawable) image3.getDrawable()).getBitmap();

    } else {

        bm = ((BitmapDrawable) image2.getDrawable()).getBitmap();}

    SaveImage.saveImageToGallery(MainActivity.this, bm);} }

```

ii. Label.java

```
package com.sunshine.nanohole_array_sensor;

import android.graphics.Bitmap;

import org.opencv.android.Utils;

import org.opencv.core.CvType;

import org.opencv.core.Mat;

import org.opencv.imgproc.Imgproc;

import static org.opencv.imgproc.Imgproc.COLOR_BGRA2GRAY;

import static org.opencv.imgproc.Imgproc.cvtColor;

public class Label {

    static int[] cc_gray(Bitmap bm){

        Mat mat = new Mat();

        Mat mat2 = new Mat();

        Mat mat3 = new Mat();

        Utils.bitmapToMat(bm,mat);

        cvtColor(mat, mat2, COLOR_BGRA2GRAY);

        int width = mat2.cols();

        int height = mat2.rows();

        int[] gray = new int[width * height];

        mat2.convertTo(mat3, CvType.CV_32S);
```

```

mat3.get(0, 0, gray);

return gray;}

static int cc_num(Bitmap bm){

    Mat mat = new Mat();

    Mat mat2 = new Mat();

    Utils.bitmapToMat(bm,mat);

    cvtColor(mat, mat2, COLOR_BGRA2GRAY);

    Mat labels = new Mat(), stats = new Mat(), centroids = new Mat();

    return Imgproc.connectedComponentsWithStats(mat2, labels, stats, centroids, 8);}

static int[] cc_labels(Bitmap bm){

    Mat mat = new Mat();

    Mat mat2 = new Mat();

    Utils.bitmapToMat(bm,mat);

    cvtColor(mat, mat2, COLOR_BGRA2GRAY);

    int width = mat2.cols();

    int height = mat2.rows();

    Mat labels = new Mat(), stats = new Mat(), centroids = new Mat();

    int num = Imgproc.connectedComponentsWithStats(mat2, labels, stats, centroids, 8);

    int[] labels1 = new int[width * height];

    labels.get(0, 0, labels1);

    return labels1;}}

```

iii. FindThreshold.java

```
package com.sunshine.nanohole_array_sensor;

public class FindThreshold {

    // Function for Otsu thresholding

    static int[] OtsuThreshold(int[] a){

        // Total number of pixels

        int total = a.length;

        // Calculate histogram

        int p = 0;

        int[] hist = new int[256];

        while (p < total) {

            int h = a[p];

            hist[h]++;

            p++;}

        int sum = 0;

        for (int t = 0 ; t < 256 ; t++){

            sum += t * hist[t];}

        int sumB = 0;

        int wB = 0;

        int wF;
```

```

float varMax = 0.0f;

int threshold = 0;

int finalSumBackground = 0;

int finalSumForeground = 0;

int weightBackground = 0;

int weightForeground = 0;

for (int t=0 ; t < 256 ; t++) {

    wB += hist[t];                // Weight Background

    if (wB == 0) continue;

    wF = total - wB;              // Weight Foreground

    if (wF == 0) break;

    sumB += (float) (t * hist[t]);

    float mB = (float) sumB / (float) wB;        // Mean Background

    float mF = (float)(sum - sumB) / (float) wF;    // Mean Foreground

    // Calculate Between Class Variance

    float varBetween = (float)wB * (float)wF * (mB - mF) * (mB - mF);

    // Check if new maximum found

    if (varBetween > varMax) {

        varMax = varBetween;

        threshold = t;

        finalSumBackground = sumB;

```

```

        finalSumForeground = sum - sumB;

        weightBackground = wB;

        weightForeground = wF;}}

int[] result = new int[5];

result[0] = threshold;

result[1] = finalSumBackground;

result[2] = finalSumForeground;

result[3] = weightBackground;

result[4] = weightForeground;

return result;}}

```

iv. Threshold.java

```

package com.sunshine.nanohole_array_sensor;

import android.graphics.Bitmap;

public class Threshold {

    static Bitmap globalThreshold(Bitmap bm){

        int width = bm.getWidth();

        int height = bm.getHeight();

        int z = width * height;

        int[] gray = new int[z];

        int[] rgb = new int[z];

```

```

bm.getPixels(rgb, 0, width, 0, 0, width, height);

for (int k = 0; k < z; k++){

    gray[k] = Math.round((float) (rgb[k] >> 16 & 0x000000FF) * 0.3f +

        (float) (rgb[k] >> 8 & 0x000000FF) * 0.59f +

        (float) (rgb[k] & 0x000000FF) * 0.11f);}

int[] t;

int[] pixels = new int[z];

t = FindThreshold.OtsuThreshold(gray);

for (int n = 0; n < z; n++) {

    if(gray[n] <= t[0]){

        pixels[n] = 0xFF000000;

    }else {

        pixels[n] = 0xFFFFFFFF;}}

Bitmap image = Bitmap.createBitmap(width, height, Bitmap.Config.ARGB_8888);

image.setPixels(pixels, 0, width, 0, 0, width, height);

return image;}

static int getT(Bitmap bm) {

    int width = bm.getWidth();

    int height = bm.getHeight();

    int z = width * height;

    int[] gray = new int[z];

```

```

int[] rgb = new int[z];

bm.getPixels(rgb, 0, width, 0, 0, width, height);

for (int k = 0; k < z; k++) {

    gray[k] = Math.round((float) (rgb[k] >> 16 & 0x000000FF) * 0.3f +

        (float) (rgb[k] >> 8 & 0x000000FF) * 0.59f +

        (float) (rgb[k] & 0x000000FF) * 0.11f);}

int[] t;

t = FindThreshold.OtsuThreshold(gray);

return t[0];}

static Bitmap localThreshold(Bitmap bm, int row1, int col1){

    int width = bm.getWidth();

    int height = bm.getHeight();

    int x = (int) ((float) width / (float) col1);

    int y = (int) ((float) height / (float) row1);

    int row = height/y;

    int col = width/x;

    int z = x * y;

    int z1 = (width - x * (col - 1)) * y;

    int z2 = x * (height - y * (row - 1));

    int z3 = (width - x * (col - 1)) * (height - y * (row - 1));

    Bitmap image = Bitmap.createBitmap(width, height, Bitmap.Config.ARGB_8888);

```

```

for (int i = 0; i < row; i++){

    for (int j = 0; j < col; j++){

        if (i != row - 1 && j == col - 1) {

            int[] rgb = new int[z1];

            bm.getPixels(rgb, 0, (width - x * (col - 1)), x * j, y * i, (width - x * (col - 1)), y);

            int[] gray = new int[z1];

            int[] pixels = new int[z1];

            for (int k = 0; k < z1; k++) {

                gray[k] = Math.round((float) (rgb[k] >> 16 & 0x000000FF) * 0.3f +

                    (float) (rgb[k] >> 8 & 0x000000FF) * 0.59f +

                    (float) (rgb[k] & 0x000000FF) * 0.11f);}

            int[] t = FindThreshold.OtsuThreshold(gray);

            for (int n = 0; n < z1; n++) {

                if (gray[n] <= t[0]) {

                    pixels[n] = 0xFF000000;

                } else {

                    pixels[n] = 0xFFFFFFFF;}}

            image.setPixels(pixels, 0, (width - x * (col - 1)), x * j, y * i, (width - x * (col - 1)),

y);

        }else if(i == row - 1 && j != col - 1){

            int[] rgb = new int[z2];

```

```

        bm.getPixels(rgb, 0, x, x * j, y * i, x, (height - y * (row - 1)));

        int[] gray = new int[z2];

        int[] pixels = new int[z2];

        for (int k = 0; k < z2; k++) {

            gray[k] = Math.round((float) (rgb[k] >> 16 & 0x000000FF) * 0.3f +

                (float) (rgb[k] >> 8 & 0x000000FF) * 0.59f +

                (float) (rgb[k] & 0x000000FF) * 0.11f);}

        int[] t = FindThreshold.OtsuThreshold(gray);

        for (int n = 0; n < z2; n++) {

            if (gray[n] <= t[0]) {

                pixels[n] = 0xFF000000;

            } else {

                pixels[n] = 0xFFFFFFFF;}}

        image.setPixels(pixels, 0, x, x * j, y * i, x, (height - y * (row - 1)));

    }else if(i == row - 1 && j == col - 1){

        int[] rgb = new int[z3];

        bm.getPixels(rgb, 0, (width - x * (col - 1)), x * j, y * i, (width - x * (col - 1)),

(height - y * (row - 1)));

        int[] gray = new int[z3];

        int[] pixels = new int[z3];

        for (int k = 0; k < z3; k++) {

```

```

        gray[k] = Math.round((float) (rgb[k] >> 16 & 0x000000FF) * 0.3f +
            (float) (rgb[k] >> 8 & 0x000000FF) * 0.59f +
            (float) (rgb[k] & 0x000000FF) * 0.11f);}

    int[] t = FindThreshold.OtsuThreshold(gray);

    for (int n = 0; n < z3; n++) {

        if (gray[n] <= t[0]) {

            pixels[n] = 0xFF000000;

        } else {

            pixels[n] = 0xFFFFFFFF;}

        image.setPixels(pixels, 0, (width - x * (col - 1)), x * j, y * i, (width - x * (col - 1)),
            (height - y * (row - 1)));

    }else{

        int[] rgb = new int[z];

        bm.getPixels(rgb, 0, x, x * j, y * i, x, y);

        int[] gray = new int[z];

        int[] pixels = new int[z];

        for (int k = 0; k < z; k++) {

            gray[k] = Math.round((float) (rgb[k] >> 16 & 0x000000FF) * 0.3f +
                (float) (rgb[k] >> 8 & 0x000000FF) * 0.59f +
                (float) (rgb[k] & 0x000000FF) * 0.11f);}

        int[] t = FindThreshold.OtsuThreshold(gray);

```

```

        for (int n = 0; n < z; n++) {

            if (gray[n] <= t[0]) {

                pixels[n] = 0xFF000000;

            } else {

                pixels[n] = 0xFFFFFFFF;}}

        image.setPixels(pixels, 0, x, x * j, y * i, x, y);}}

    return image;}}

```

v. FindTforAnyRange.java

```

package com.sunshine.nanohole_array_sensor;

public class FindTforAnyRange {

    // Function for Otsu thresholding

    static int[] OtsuThreshold(int[] a){

        // Total number of pixels

        int total = a.length;

        // Calculate histogram

        int p = 0;

        int[] hist = new int[a[0]+1];    //updated

        while (p < total) {

            int h = a[p];

            hist[h]++;

```

```

        p++;}

int sum = 0;

for (int t = 0 ; t < total ; t++){    //updated

    sum += a[t];}

int sumB = 0;

int wB = 0;

int wF;

float varMax = 0.0f;

int threshold = 0;

int finalSumBackground = 0;

int finalSumForeground = 0;

int weightBackground = 0;

int weightForeground = 0;

for (int t=0 ; t < a[0]+1 ; t++) {

    wB += hist[t];                // Weight Background

    if (wB == 0 | hist[t] == 0) continue;    //updated

    wF = total - wB;                // Weight Foreground

    if (wF == 0) break;

    sumB += (float) (t * hist[t]);

    float mB = (float) sumB / (float) wB;        // Mean Background

    float mF = (float)(sum - sumB) / (float) wF;    // Mean Foreground

```

```

// Calculate Between Class Variance

float varBetween = (float)wB * (float)wF * (mB - mF) * (mB - mF);

// Check if new maximum found

if (varBetween > varMax) {

    varMax = varBetween;

    threshold = t;

    finalSumBackground = sumB;

    finalSumForeground = sum - sumB;

    weightBackground = wB;

    weightForeground = wF;}}

int[] result = new int[5];

result[0] = threshold;

result[1] = finalSumBackground;

result[2] = finalSumForeground;

result[3] = weightBackground;

result[4] = weightForeground;

return result;}}

```

vi. Morphology.java

```

package com.sunshine.nanohole_array_sensor;

import android.graphics.Bitmap;

```

```

import org.opencv.android.Utils;

import org.opencv.core.Mat;

import org.opencv.imgproc.Imgproc;

public class Morphology {

    static Bitmap erode(Bitmap bm) {

        Bitmap bm2 = Bitmap.createBitmap(bm.getWidth(), bm.getHeight(),
Bitmap.Config.ARGB_8888);

        Mat mat = new Mat();

        Mat mat3 = new Mat();

        Utils.bitmapToMat(bm,mat);

        Imgproc.erode(mat, mat3, new Mat());

        Utils.matToBitmap(mat3, bm2);

        return bm2;}

    static Bitmap dilate(Bitmap bm) {

        Bitmap bm2 = Bitmap.createBitmap(bm.getWidth(), bm.getHeight(),
Bitmap.Config.ARGB_8888);

        Mat mat = new Mat();

        Mat mat3 = new Mat();

        Utils.bitmapToMat(bm,mat);

        Imgproc.dilate(mat, mat3, new Mat());

        Utils.matToBitmap(mat3, bm2);

```

```
return bm2;}}
```

vii. SaveImage.java

```
package com.sunshine.nanohole_array_sensor;

import android.content.Context;

import android.content.Intent;

import android.graphics.Bitmap;

import android.net.Uri;

import android.os.Environment;

import android.provider.MediaStore;

import android.widget.Toast;

import java.io.File;

import java.io.FileNotFoundException;

import java.io.FileOutputStream;

import java.io.IOException;

public class SaveImage {

    public static void saveImageToGallery(Context context, Bitmap bmp) {

        File appDir = new File(Environment.getExternalStorageDirectory(),

            "image");

        if (!appDir.exists()) {

            appDir.mkdir();}
```

```

String fileName = System.currentTimeMillis() + ".jpg";

File file = new File(appDir, fileName);

try {

    FileOutputStream fos = new FileOutputStream(file);

    bmp.compress(Bitmap.CompressFormat.JPEG, 100, fos);

    fos.flush();

    fos.close();

} catch (FileNotFoundException e) {

    Toast.makeText(context, "Image save failed!", Toast.LENGTH_SHORT).show();

    e.printStackTrace();

} catch (IOException e) {

    Toast.makeText(context, "Image save failed!", Toast.LENGTH_SHORT).show();

    e.printStackTrace();}

try {

    MediaStore.Images.Media.insertImage(context.getContentResolver(),

        file.getAbsolutePath(), fileName, null);

    Toast.makeText(context, "Image save successfully!", Toast.LENGTH_SHORT).show();

} catch (FileNotFoundException e) {

    Toast.makeText(context, "Image save failed!", Toast.LENGTH_SHORT).show();

    e.printStackTrace();}

context.sendBroadcast(new Intent(Intent.ACTION_MEDIA_SCANNER_SCAN_FILE,

```

```
Uri.fromFile(new File(file.getPath())));}}
```

viii. activity_main.xml

```
<?xml version="1.0" encoding="utf-8"?>  
  
<androidx.constraintlayout.widget.ConstraintLayout  
  
xmlns:android="http://schemas.android.com/apk/res/android"  
  
xmlns:app="http://schemas.android.com/apk/res-auto"  
  
xmlns:tools="http://schemas.android.com/tools"  
  
android:layout_width="match_parent"  
  
android:layout_height="match_parent"  
  
tools:context=".MainActivity">  
  
<Button  
  
android:id="@+id/Load_an_image"  
  
android:layout_width="wrap_content"  
  
android:layout_height="wrap_content"  
  
android:layout_marginStart="16dp"  
  
android:layout_marginTop="8dp"  
  
android:layout_marginEnd="16dp"  
  
android:text="@string/Load_an_image"  
  
android:textSize="18sp"  
  
app:layout_constraintEnd_toStartOf="@+id/Take_a_photo"
```

```
app:layout_constraintStart_toStartOf="parent"  
app:layout_constraintTop_toTopOf="parent" />
```

```
<ImageView
```

```
    android:id="@+id/image"  
    android:layout_width="200dp"  
    android:layout_height="220dp"  
    android:contentDescription="@string/image"  
    app:layout_constraintBottom_toTopOf="@+id/guideline2"  
    app:layout_constraintEnd_toStartOf="@+id/image2"  
    app:layout_constraintStart_toStartOf="parent"  
    app:layout_constraintTop_toTopOf="@+id/guideline"  
    app:srcCompat="@null" />
```

```
<androidx.constraintlayout.widget.Guideline
```

```
    android:id="@+id/guideline"  
    android:layout_width="wrap_content"  
    android:layout_height="wrap_content"  
    android:orientation="horizontal"  
    app:layout_constraintGuide_begin="120dp" />
```

```
<EditText
```

```
    android:id="@+id/row"  
    android:layout_width="40dp"
```

```
android:layout_height="60dp"

android:layout_marginStart="16dp"

android:ems="10"

android:inputType="textPersonName"

android:textSize="20sp"

app:layout_constraintBottom_toTopOf="@+id/guideline"

app:layout_constraintStart_toEndOf="@+id/textView"

tools:text="row" />
```

```
<EditText
```

```
android:id="@+id/col"

android:layout_width="40dp"

android:layout_height="60dp"

android:layout_marginStart="16dp"

android:ems="10"

android:inputType="textPersonName"

android:textSize="20sp"

app:layout_constraintBottom_toTopOf="@+id/guideline"

app:layout_constraintStart_toEndOf="@+id/row"

tools:text="col" />
```

```
<androidx.constraintlayout.widget.Guideline
```

```
android:id="@+id/guideline2"
```

```
android:layout_width="wrap_content"

android:layout_height="wrap_content"

android:orientation="horizontal"

app:layout_constraintGuide_begin="360dp" />
```

```
<TextView
```

```
    android:id="@+id/textView"

    android:layout_width="wrap_content"

    android:layout_height="wrap_content"

    android:layout_marginStart="16dp"

    android:text="@string/textView"

    android:textSize="24sp"

    app:layout_constraintBottom_toTopOf="@+id/guideline"

    app:layout_constraintStart_toStartOf="parent"

    app:layout_constraintTop_toBottomOf="@+id/Load_an_image" />
```

```
<ScrollView
```

```
    android:id="@+id/scrollView"

    android:layout_width="0dp"

    android:layout_height="0dp"

    android:layout_marginStart="8dp"

    android:layout_marginEnd="8dp"

    android:layout_marginBottom="8dp"
```

```

app:layout_constraintBottom_toTopOf="@+id/lt"

app:layout_constraintEnd_toEndOf="parent"

app:layout_constraintStart_toStartOf="parent"

app:layout_constraintTop_toTopOf="@+id/guideline3">

<LinearLayout

    android:id="@+id/LL"

    android:layout_width="match_parent"

    android:layout_height="wrap_content"

    android:orientation="vertical">

    <TextView

        android:id="@+id/result"

        android:layout_width="match_parent"

        android:layout_height="match_parent"

        android:textSize="24sp"

        tools:text="@string/result" />

    </LinearLayout>

</ScrollView>

<Button

    android:id="@+id/Save"

    style="@style/Widget.AppCompat.Button.Small"

    android:layout_width="wrap_content"

```

```
android:layout_height="wrap_content"

android:layout_marginTop="8dp"

android:layout_marginEnd="8dp"

android:text="@string/Save"

android:textSize="18sp"

app:layout_constraintEnd_toEndOf="parent"

app:layout_constraintTop_toTopOf="parent" />
```

<Button

```
android:id="@+id/Take_a_photo"

android:layout_width="wrap_content"

android:layout_height="wrap_content"

android:layout_marginStart="16dp"

android:layout_marginTop="8dp"

android:text="@string/Take_a_photo"

android:textSize="18sp"

app:layout_constraintStart_toEndOf="@+id/Load_an_image"

app:layout_constraintTop_toTopOf="parent" />
```

<androidx.constraintlayout.widget.Guideline

```
android:id="@+id/guideline3"

android:layout_width="wrap_content"

android:layout_height="wrap_content"
```

```
android:orientation="horizontal"

app:layout_constraintGuide_begin="600dp" />
```

```
<ImageView
```

```
    android:id="@+id/image2"

    android:layout_width="200dp"

    android:layout_height="220dp"

    app:layout_constraintBottom_toTopOf="@+id/guideline2"

    app:layout_constraintEnd_toEndOf="parent"

    app:layout_constraintStart_toEndOf="@+id/image"

    app:layout_constraintTop_toTopOf="@+id/guideline"

    app:srcCompat="@null" />
```

```
<Button
```

```
    android:id="@+id/t"

    style="@style/Widget.AppCompat.Button.Small"

    android:layout_width="wrap_content"

    android:layout_height="wrap_content"

    android:text="@string/t"

    android:textSize="18sp"

    app:layout_constraintBottom_toBottomOf="parent"

    app:layout_constraintStart_toStartOf="parent" />
```

```
<Button
```

```
android:id="@+id/total"

style="@style/Widget.AppCompat.Button.Small"

android:layout_width="wrap_content"

android:layout_height="wrap_content"

android:text="@string/total"

android:textSize="18sp"

app:layout_constraintBottom_toBottomOf="parent"

app:layout_constraintEnd_toStartOf="@+id/mean" />
```

<Button

```
android:id="@+id/mean"

style="@style/Widget.AppCompat.Button.Small"

android:layout_width="wrap_content"

android:layout_height="wrap_content"

android:text="@string/mean"

android:textSize="18sp"

app:layout_constraintBottom_toBottomOf="parent"

app:layout_constraintEnd_toEndOf="parent" />
```

<Button

```
android:id="@+id/Save2"

style="@style/Widget.AppCompat.Button.Small"

android:layout_width="wrap_content"
```

```
android:layout_height="wrap_content"

android:layout_marginTop="8dp"

android:layout_marginEnd="8dp"

android:text="@string/Save2"

android:textSize="18sp"

app:layout_constraintEnd_toEndOf="parent"

app:layout_constraintTop_toBottomOf="@+id/Save" />
```

<Button

```
android:id="@+id/lt"

style="@style/Widget.AppCompat.Button.Small"

android:layout_width="wrap_content"

android:layout_height="wrap_content"

android:text="@string/lt"

android:textSize="18sp"

app:layout_constraintBottom_toTopOf="@+id/t"

app:layout_constraintStart_toStartOf="parent" />
```

<Button

```
android:id="@+id/erode"

style="@style/Widget.AppCompat.Button.Small"

android:layout_width="wrap_content"

android:layout_height="wrap_content"
```

```
android:text="@string/erode"

android:textSize="18sp"

app:layout_constraintBottom_toTopOf="@+id/t"

app:layout_constraintStart_toEndOf="@+id/t" />
```

<Button

```
android:id="@+id/dilate"

style="@style/Widget.AppCompat.Button.Small"

android:layout_width="wrap_content"

android:layout_height="wrap_content"

android:text="@string/dilate"

android:textSize="18sp"

app:layout_constraintBottom_toBottomOf="parent"

app:layout_constraintStart_toEndOf="@+id/t" />
```

<ImageView

```
android:id="@+id/image3"

android:layout_width="200dp"

android:layout_height="220dp"

app:layout_constraintBottom_toTopOf="@+id/guideline3"

app:layout_constraintEnd_toStartOf="@+id/image4"

app:layout_constraintStart_toStartOf="parent"

app:layout_constraintTop_toTopOf="@+id/guideline2"
```

```
app:srcCompat="@null" />
```

```
<ImageView
```

```
android:id="@+id/image4"
```

```
android:layout_width="200dp"
```

```
android:layout_height="220dp"
```

```
app:layout_constraintBottom_toTopOf="@+id/guideline3"
```

```
app:layout_constraintEnd_toEndOf="parent"
```

```
app:layout_constraintStart_toEndOf="@+id/image3"
```

```
app:layout_constraintTop_toTopOf="@+id/guideline2"
```

```
app:srcCompat="@null" />
```

```
<Button
```

```
android:id="@+id/clear"
```

```
style="@style/Widget.AppCompat.Button.Small"
```

```
android:layout_width="wrap_content"
```

```
android:layout_height="wrap_content"
```

```
android:text="@string/clear"
```

```
android:textSize="18sp"
```

```
app:layout_constraintBottom_toBottomOf="parent"
```

```
app:layout_constraintStart_toEndOf="@+id/dilate" />
```

```
</androidx.constraintlayout.widget.ConstraintLayout>
```

ix. AndroidManifest.xml

```
<?xml version="1.0" encoding="utf-8"?>

<manifest xmlns:android="http://schemas.android.com/apk/res/android"

    package="com.sunshine.nanohole_array_sensor">

    <uses-permission android:name="android.permission.WRITE_EXTERNAL_STORAGE"/>

    <uses-permission android:name="android.permission.CAMERA"/>

    <application

        android:allowBackup="true"

        android:icon="@mipmap/ic_launcher"

        android:label="@string/app_name"

        android:roundIcon="@mipmap/ic_launcher_round"

        android:supportsRtl="true"

        android:theme="@style/AppTheme">

        <activity android:name=".MainActivity">

            <intent-filter>

                <action android:name="android.intent.action.MAIN" />

                <category android:name="android.intent.category.LAUNCHER" />

            </intent-filter>

        </activity>

    </application>
```

```
</manifest>
```

x. strings.xml

```
<resources>
```

```
<string name="app_name">Nanohole_Array_Sensor</string>
```

```
<string name="Load_an_image">Load an image</string>
```

```
<string name="Calculate">Calculate</string>
```

```
<string name="image">image</string>
```

```
<string name="textView">Input Row and Col</string>
```

```
<string name="result">result</string>
```

```
<string name="Save">Save</string>
```

```
<string name="Take_a_photo">Take a photo</string>
```

```
<string name="t">t</string>
```

```
<string name="total">total</string>
```

```
<string name="mean">mean</string>
```

```
<string name="Save2">Save2</string>
```

```
<string name="lt">lt</string>
```

```
<string name="erode">erode</string>
```

```
<string name="dilate">dilate</string>
```

```
<string name="clear">clear</string>
```

```
</resources>
```